

Readiness of the ATLAS Liquid Argon Calorimeter for LHC Collisions

G. Aad⁸³, B. Abbott¹¹⁰, J. Abdallah¹¹, A.A. Abdelalim⁴⁹, A. Abdesselam¹¹⁷, O. Abdinov¹⁰, B. Abi¹¹¹, M. Abolins⁸⁸, H. Abramowicz¹⁵¹, H. Abreu¹¹⁴, B.S. Acharya^{162a,162b}, D.L. Adams²⁴, T.N. Addy⁵⁶, J. Adelman¹⁷³, C. Adorisio^{36a,36b}, P. Adragna⁷⁵, T. Adye¹²⁸, S. Aefsky²², J.A. Aguilar-Saavedra^{123a}, M. Aharrouche⁸¹, S.P. Ahlen²¹, F. Ahles⁴⁸, A. Ahmad¹⁴⁶, H. Ahmed², M. Ahsan⁴⁰, G. Aielli^{132a,132b}, T. Akdogan¹⁸, T.P.A. Åkesson⁷⁹, G. Akimoto¹⁵³, A.V. Akimov⁹⁴, A. Aktas⁴⁸, M.S. Alam¹, M.A. Alam⁷⁶, J. Albert¹⁶⁷, S. Albrand⁵⁵, M. Aleksa²⁹, I.N. Aleksandrov⁶⁵, F. Alessandria^{89a,89b}, C. Alexa^{25a}, G. Alexander¹⁵¹, G. Alexandre⁴⁹, T. Alexopoulos⁹, M. Alhroob²⁰, M. Aliev¹⁵, G. Alimonti^{89a}, J. Alison¹¹⁹, M. Aliyev¹⁰, P.P. Allport⁷³, S.E. Allwood-Spiers⁵³, J. Almond⁸², A. Aloisio^{102a,102b}, R. Alon¹⁶⁹, A. Alonso⁷⁹, M.G. Alvigi^{102a,102b}, K. Amako⁶⁶, C. Amelung²², V.V. Ammosov¹²⁷, A. Amorim^{123b}, G. Amorós¹⁶⁵, N. Amram¹⁵¹, C. Anastopoulos¹³⁸, T. Andeen²⁹, C.F. Anders⁴⁸, K.J. Anderson³⁰, A. Andreazza^{89a,89b}, V. Andrei^{58a}, X.S. Anduaga⁷⁰, A. Angerami³⁴, F. Anghinolfi²⁹, N. Anjos^{123b}, A. Antonaki⁸, M. Antonelli⁴⁷, S. Antonelli^{19a,19b}, B. Antunovic⁴¹, F. Anulli^{131a}, S. Aoun⁸³, G. Arabidze⁸, I. Aracena¹⁴², Y. Arai⁶⁶, A.T.H. Arce¹⁴, J.P. Archambault²⁸, S. Arfaoui^{29,a}, J-F. Arguin¹⁴, T. Argyropoulos⁹, E. Arik^{18,*}, M. Arik¹⁸, A.J. Armbruster⁸⁷, O. Arnaez⁴, C. Arnault¹¹⁴, A. Artamonov⁹⁵, D. Arutinov²⁰, M. Asai¹⁴², S. Asai¹⁵³, R. Asfandiyarov¹⁷⁰, S. Ask⁸², B. Åsman¹⁴⁴, D. Asner²⁸, L. Asquith⁷⁷, K. Assamagan²⁴, A. Astbury¹⁶⁷, A. Astvatsatourov⁵², G. Atoian¹⁷³, B. Auerbach¹⁷³, E. Auge¹¹⁴, K. Augsten¹²⁶, M. Aurousseau⁴, N. Austin⁷³, G. Avolio¹⁶¹, R. Avramidou⁹, D. Axen¹⁶⁶, C. Ay⁵⁴, G. Azuelos^{93,b}, Y. Azuma¹⁵³, M.A. Baak²⁹, G. Baccaglioni^{89a,89b}, C. Bacci^{133a,133b}, A. Bach¹⁴, H. Bachacou¹³⁵, K. Bachas²⁹, M. Backes⁴⁹, E. Badescu^{25a}, P. Bagnaia^{131a,131b}, Y. Bai³², D.C. Bailey¹⁵⁶, T. Bain¹⁵⁶, J.T. Baines¹²⁸, O.K. Baker¹⁷³, M.D. Baker²⁴, F. Baltasar Dos Santos Pedrosa²⁹, E. Banas³⁸, P. Banerjee⁹³, S. Banerjee¹⁶⁷, D. Banfi^{89a,89b}, A. Bangert¹³⁶, V. Bansal¹⁶⁷, S.P. Baranov⁹⁴, S. Baranov⁶⁵, A. Barashkou⁶⁵, T. Barber²⁷, E.L. Barberio⁸⁶, D. Barberis^{50a,50b}, M. Barbero²⁰, D.Y. Bardin⁶⁵, T. Barillari⁹⁹, M. Barisonzi¹⁷², T. Barklow¹⁴², N. Barlow²⁷, B.M. Barnett¹²⁸, R.M. Barnett¹⁴, S. Baron²⁹, A. Baroncelli^{133a}, A.J. Barr¹¹⁷, F. Barreiro⁸⁰, J. Barreiro Guimarães da Costa⁵⁷, P. Barrillon¹¹⁴, N. Barros^{123b}, R. Bartoldus¹⁴², D. Bartsch²⁰, J. Bastos^{123b}, R.L. Bates⁵³, S. Bathe²⁴, L. Batkova¹⁴³, J.R. Batley²⁷, A. Battaglia¹⁶, M. Battistin²⁹, F. Bauer¹³⁵, H.S. Bawa¹⁴², M. Bazalova¹²⁴, B. Beare¹⁵⁶, T. Beau⁷⁸, P.H. Beauchemin¹¹⁷, R. Beccherle^{50a}, N. Becerici¹⁸, P. Bechtel⁴¹, G.A. Beck⁷⁵, H.P. Beck¹⁶, M. Beckingham⁴⁸, K.H. Becks¹⁷², I. Bedajane¹²⁶, A.J. Beddall^{18,c}, A. Beddall^{18,c}, P. Bednár¹⁴³, V.A. Bednyakov⁶⁵, C. Bee⁸³, M. Begel²⁴, S. Behar Harpaz¹⁵⁰, P.K. Behera⁶³, M. Beimforde⁹⁹, C. Belanger-Champagne¹⁶⁴, P.J. Bell⁸², W.H. Bell⁴⁹, G. Bella¹⁵¹, L. Bellagamba^{19a}, F. Bellina²⁹, M. Bellomo^{118a}, A. Belloni⁵⁷, K. Belotskiy⁹⁶, O. Beltramello²⁹, S. Ben Ami¹⁵⁰, O. Benary¹⁵¹, D. Bencheikroun^{134a}, M. Bendel⁸¹, B.H. Benedict¹⁶¹, N. Benekos¹⁶³, Y. Benhammou¹⁵¹, G.P. Benincasa^{123b}, D.P. Benjamin⁴⁴, M. Benoit¹¹⁴, J.R. Bensinger²², K. Benslama¹²⁹, S. Bentvelsen¹⁰⁵, M. Beretta⁴⁷, D. Berge²⁹, E. Bergeaas Kuutmann¹⁴⁴, N. Berger⁴, F. Berghaus¹⁶⁷, E. Berglund⁴⁹, J. Beringer¹⁴, K. Bernardet⁸³, P. Bernat¹¹⁴, R. Bernhard⁴⁸, C. Bernius⁷⁷, T. Berry⁷⁶, A. Bertin^{19a,19b}, N. Besson¹³⁵, S. Bethke⁹⁹, R.M. Bianchi⁴⁸, M. Bianco^{72a,72b}, O. Biebel⁹⁸, J. Biesiada¹⁴, M. Biglietti^{131a,131b}, H. Bilokon⁴⁷, M. Bindi^{19a,19b}, S. Binet¹¹⁴, A. Bingul^{18,c}, C. Bini^{131a,131b}, C. Biscarat¹⁷⁸, U. Bitenc⁴⁸, K.M. Black⁵⁷, R.E. Blair⁵, J-B Blanchard¹¹⁴, G. Blanchot²⁹, C. Blocker²², J. Blocki³⁸, A. Blondel⁴⁹, W. Blum⁸¹, U. Blumenschein⁵⁴, G.J. Bobbink¹⁰⁵, A. Bocci⁴⁴, M. Boehler⁴¹, J. Boek¹⁷², N. Boelaert⁷⁹, S. Böser⁷⁷, J.A. Bogaerts²⁹, A. Bogouch^{90,*}, C. Bohm¹⁴⁴, J. Bohm¹²⁴, V. Boisvert⁷⁶, T. Bold^{161,d}, V. Boldea^{25a}, A. Boldyrev⁹⁷, V.G. Bondarenko⁹⁶, M. Bondioli¹⁶¹, M. Boonekamp¹³⁵, J.R.A. Booth¹⁷, S. Bordini⁷⁸, C. Borer¹⁶, A. Borisov¹²⁷, G. Borissov⁷¹, I. Borjanovic^{72a}, S. Borroni^{131a,131b}, K. Bos¹⁰⁵, D. Boscherini^{19a}, M. Bosman¹¹, M. Bosteels²⁹, H. Boterenbrood¹⁰⁵, J. Bouchami⁹³, J. Boudreau¹²², E.V. Bouhova-Thacker⁷¹, C. Boulahouache¹²², C. Bourdarios¹¹⁴, J. Boyd²⁹, I.R. Boyko⁶⁵, I. Bozovic-Jelisavcic^{12b}, J. Bracinik¹⁷, A. Braem²⁹, P. Branchini^{133a}, G.W. Brandenburg⁵⁷, A. Brandt⁷, G. Brandt⁴¹, O. Brandt⁵⁴, U. Bratzler¹⁵⁴, B. Brau⁸⁴, J.E. Brau¹¹³, H.M. Braun¹⁷², B. Brelief¹⁵⁶, J. Bremer²⁹, R. Brenner¹⁶⁴, S. Bressler¹⁵⁰, D. Breton¹¹⁴, N.D. Brett¹¹⁷, D. Britton⁵³, F.M. Brochu²⁷, I. Brock²⁰, R. Brock⁸⁸, T.J. Brodbeck⁷¹, E. Brodet¹⁵¹, F. Broggi^{89a,89b}, C. Bromberg⁸⁸, G. Brooijmans³⁴, W.K. Brooks^{31b}, G. Brown⁸², E. Brubaker³⁰, P.A. Bruckman de Renstrom³⁸, D. Bruncko¹⁴³, R. Bruneliere⁴⁸, S. Brunet⁴¹, A. Bruni^{19a}, G. Bruni^{19a}, M. Bruschi^{19a}, T. Buanes¹³, F. Bucci⁴⁹, J. Buchanan¹¹⁷, P. Buchholz¹⁴⁰, A.G. Buckley^{77,e}, I.A. Budagov⁶⁵, B. Budick¹⁰⁷, V. Büscher⁸¹, L. Bugge¹¹⁶, O. Bulekov⁹⁶, M. Bunse⁴², T. Buran¹¹⁶, H. Burckhart²⁹, S. Burdin⁷³, T. Burgess¹³, S. Burke¹²⁸, E. Busato³³, P. Bussey⁵³, C.P. Buszello¹⁶⁴, F. Butin²⁹, B. Butler¹⁴², J.M. Butler²¹, C.M. Buttar⁵³, J.M. Butterworth⁷⁷, T. Byatt⁷⁷, J. Caballero²⁴, S. Cabrera Urbán¹⁶⁵, D. Caforio^{19a,19b}, O. Cakir³, P. Calafiura¹⁴, G. Calderini⁷⁸, P. Calfayan⁹⁸, R. Calkins⁵,

L.P. Caloba^{23a}, R. Caloi^{131a,131b}, D. Calvet³³, P. Camarri^{132a,132b}, M. Cambiaghi^{118a,118b}, D. Cameron¹¹⁶, F. Campabadal Segura¹⁶⁵, S. Campana²⁹, M. Campanelli⁷⁷, V. Canale^{102a,102b}, F. Canelli³⁰, A. Canepa^{157a}, J. Cantero⁸⁰, L. Capasso^{102a,102b}, M.D.M. Capeans Garrido²⁹, I. Caprini^{25a}, M. Caprini^{25a}, M. Capua^{36a,36b}, R. Caputo¹⁴⁶, D. Caracinha^{123b}, C. Caramarcu^{25a}, R. Cardarelli^{132a}, T. Carli²⁹, G. Carlino^{102a}, L. Carminati^{89a,89b}, B. Caron^{2,b}, S. Caron⁴⁸, G.D. Carrillo Montoya¹⁷⁰, S. Carron Montero¹⁵⁶, A.A. Carter⁷⁵, J.R. Carter²⁷, J. Carvalho^{123b}, D. Casadei¹⁰⁷, M.P. Casado¹¹, M. Cascella^{121a,121b}, C. Caso^{50a,50b,*}, A.M. Castaneda Hernadez¹⁷⁰, E. Castaneda-Miranda¹⁷⁰, V. Castillo Gimenez¹⁶⁵, N. Castro^{123a}, G. Cataldi^{72a}, A. Catinaccio²⁹, J.R. Catmore⁷¹, A. Cattai²⁹, G. Cattani^{132a,132b}, S. Caughron³⁴, D. Cauz^{162a,162c}, P. Cavalleri⁷⁸, D. Cavalli^{89a}, M. Cavalli-Sforza¹¹, V. Cavašinni^{121a,121b}, F. Ceradini^{133a,133b}, A.S. Cerqueira^{23a}, A. Cerri²⁹, L. Cerrito⁷⁵, F. Cerutti⁴⁷, S.A. Cetin^{18,f}, F. Cevenini^{102a,102b}, A. Chafaq^{134a}, D. Chakraborty⁵, K. Chan², J.D. Chapman²⁷, J.W. Chapman⁸⁷, E. Chareyre⁷⁸, D.G. Charlton¹⁷, V. Chavda⁸², S. Cheatham⁷¹, S. Chekanov⁵, S.V. Chekulaev^{157a}, G.A. Chelkov⁶⁵, H. Chen²⁴, S. Chen³², T. Chen³², X. Chen¹⁷⁰, S. Cheng³², A. Cheplakov⁶⁵, V.F. Chepurinov⁶⁵, R. Cherkaoui El Moursli^{134d}, V. Tcherniatine²⁴, D. Chesneau^{25a}, E. Cheu⁶, S.L. Cheung¹⁵⁶, L. Chevalier¹³⁵, F. Chevallier¹³⁵, V. Chiarella⁴⁷, G. Chiefari^{102a,102b}, L. Chikovani⁵¹, J.T. Childers^{58a}, A. Chilingarov⁷¹, G. Chiodini^{72a}, M. Chizhov⁶⁵, G. Choudalakis³⁰, S. Chouridou¹³⁶, D. Chren¹²⁶, I.A. Christidi¹⁵², A. Christov⁴⁸, D. Chromek-Burckhart²⁹, M.L. Chu¹⁴⁹, J. Chudoba¹²⁴, G. Ciapetti^{131a,131b}, A.K. Ciftci³, R. Ciftci³, D. Cinca³³, V. Cindro⁷⁴, M.D. Ciobotaru¹⁶¹, C. Ciocca^{19a,19b}, A. Ciocio¹⁴, M. Cirilli⁸⁷, M. Citterio^{89a}, A. Clark⁴⁹, W. Cleland¹²², J.C. Clemens⁸³, B. Clement⁵⁵, C. Clement¹⁴⁴, D. Clements⁵³, Y. Coadou⁸³, M. Cobal^{162a,162c}, A. Coccaro^{50a,50b}, J. Cochran⁶⁴, S. Coelli^{89a,89b}, J. Coggeshall¹⁶³, E. Cogneras¹⁶, C.D. Cojocar²⁸, J. Colas⁴, B. Cole³⁴, A.P. Colijn¹⁰⁵, C. Collard¹¹⁴, N.J. Collins¹⁷, C. Collins-Tooth⁵³, J. Collot⁵⁵, G. Colon⁸⁴, R. Coluccia^{72a,72b}, P. Conde Muiño^{123b}, E. Coniavitis¹⁶⁴, M. Consonni¹⁰⁴, S. Constantinescu^{25a}, C. Conta^{118a,118b}, F. Conventi^{102a,g}, J. Cook²⁹, M. Cooke³⁴, B.D. Cooper⁷⁵, A.M. Cooper-Sarkar¹¹⁷, N.J. Cooper-Smith⁷⁶, K. Copic³⁴, T. Cornelissen^{50a,50b}, M. Corradi^{19a}, F. Corriveau^{85,h}, A. Corso-Radu¹⁶¹, A. Cortes-Gonzalez¹⁶³, G. Cortiana⁹⁹, G. Costa^{89a}, M.J. Costa¹⁶⁵, D. Costanzo¹³⁸, T. Costin³⁰, D. Côté⁴¹, R. Coura Torres^{23a}, L. Courneyea¹⁶⁷, G. Cowan⁷⁶, C. Cowden²⁷, B.E. Cox⁸², K. Cranmer¹⁰⁷, J. Cranshaw⁵, M. Cristinziani²⁰, G. Crosetti^{36a,36b}, R. Crupi^{72a,72b}, S. Crépe-Renaudin⁵⁵, C. Cuenca Almenar¹⁷³, T. Cuhadar Donszelmann¹³⁸, M. Curatolo⁴⁷, C.J. Curtis¹⁷, P. Cwetanski⁶¹, Z. Czyzula³⁵, S. D'Auria⁵³, M. D'Onofrio¹¹, A. D'Orazio⁹⁹, P.V.M. Da Silva^{23a}, C. Da Via⁸², W. Dabrowski³⁷, T. Dai⁸⁷, C. Dallapiccola⁸⁴, S.J. Dallison^{128,*}, C.H. Daly¹³⁷, M. Dam³⁵, H.O. Danielsson²⁹, D. Dannheim⁹⁹, V. Dao⁴⁹, G. Darbo^{50a}, G.L. Darlea^{25a}, W. Davey⁸⁶, T. Davidek¹²⁵, N. Davidson⁸⁶, R. Davidson⁷¹, A.R. Davison⁷⁷, I. Dawson¹³⁸, J.W. Dawson⁵, R.K. Daya³⁹, K. De⁷, R. de Asmundis^{102a}, S. De Castro^{19a,19b}, P.E. De Castro Faria Salgado²⁴, S. De Cecco⁷⁸, J. de Graat⁹⁸, N. De Groot¹⁰⁴, P. de Jong¹⁰⁵, E. De La Cruz-Burelo⁸⁷, C. De La Taille¹¹⁴, L. De Mora⁷¹, M. De Oliveira Branco²⁹, D. De Pedis^{131a}, A. De Salvo^{131a}, U. De Sanctis^{162a,162c}, A. De Santo⁷⁶, J.B. De Vivie De Regie¹¹⁴, G. De Zorzi^{131a,131b}, S. Dean⁷⁷, H. Deberg¹⁶³, G. Dedes⁹⁹, D.V. Dedovich⁶⁵, P.O. Defay³³, J. Degenhardt¹¹⁹, M. Dehchar¹¹⁷, C. Del Papa^{162a,162c}, J. Del Peso⁸⁰, T. Del Prete^{121a,121b}, A. Dell'Acqua²⁹, L. Dell'Asta^{89a,89b}, M. Della Pietra^{102a,g}, D. della Volpe^{102a,102b}, M. Delmastro²⁹, N. Delruelle²⁹, P.A. Delsart⁵⁵, C. Deluca¹⁴⁶, S. Demers¹⁷³, M. Demichev⁶⁵, B. Demirköz²⁷, J. Deng¹⁶¹, W. Deng²⁴, S.P. Denisov¹²⁷, C. Dennis¹¹⁷, J.E. Derkaoui^{134c}, F. Derue⁷⁸, P. Dervan⁷³, K. Desch²⁰, P.O. Deviveiros¹⁵⁶, A. Dewhurst⁷¹, B. DeWilde¹⁴⁶, S. Dhaliwal¹⁵⁶, R. Dhullipudi^{24,i}, A. Di Ciaccio^{132a,132b}, L. Di Ciaccio⁴, A. Di Domenico^{131a,131b}, A. Di Girolamo²⁹, B. Di Girolamo²⁹, S. Di Luise^{133a,133b}, A. Di Mattia⁸⁸, R. Di Nardo^{132a,132b}, A. Di Simone^{132a,132b}, R. Di Sipio^{19a,19b}, M.A. Diaz^{31a}, F. Diblen¹⁸, E.B. Diehl⁸⁷, J. Dietrich⁴⁸, S. Diglio¹¹⁴, K. Dindar Yagci³⁹, D.J. Dingfelder⁴⁸, C. Dionisi^{131a,131b}, P. Dita^{25a}, S. Dita^{25a}, F. Dittus²⁹, F. Djama⁸³, R. Djilkibaev¹⁰⁷, T. Djobava⁵¹, M.A.B. do Vale^{23a}, A. Do Valle Wemans^{123b}, M. Dobbs⁸⁵, D. Dobos²⁹, E. Dobson¹¹⁷, M. Dobson¹⁶¹, J. Dodd³⁴, O.B. Dogan^{18,*}, T. Doherty⁵³, Y. Doi⁶⁶, J. Dolejsi¹²⁵, I. Dolenc⁷⁴, Z. Dolezal¹²⁵, B.A. Dolgoshein⁹⁶, T. Dohmae¹⁵³, M. Donega¹¹⁹, J. Donini⁵⁵, J. Dopke¹⁷², A. Doria^{102a}, A. Dos Anjos¹⁷⁰, A. Dotti^{121a,121b}, M.T. Dova⁷⁰, A. Doxiadis¹⁰⁵, A.T. Doyle⁵³, Z. Drasal¹²⁵, C. Driouichi³⁵, M. Dris⁹, J. Dubbert⁹⁹, E. Duchovni¹⁶⁹, G. Duckeck⁹⁸, A. Dudarev²⁹, F. Dudziak¹¹⁴, M. Dührssen⁴⁸, L. Duflot¹¹⁴, M-A. Dufour⁸⁵, M. Dunford³⁰, A. Duperrin⁸³, H. Duran Yildiz^{3,j}, A. Dushkin²², R. Duxfield¹³⁸, M. Dwuznik³⁷, M. Düren⁵², W.L. Ebenstein⁴⁴, J. Ebke⁹⁸, S. Eckert⁴⁸, S. Eckweiler⁸¹, K. Edmonds⁸¹, C.A. Edwards⁷⁶, P. Eerola^{79,k}, K. Egorov⁶¹, W. Ehrenfeld⁴¹, T. Ehrich⁹⁹, T. Eifert²⁹, G. Eigen¹³, K. Einsweiler¹⁴, E. Eisenhandler⁷⁵, T. Ekelof¹⁶⁴, M. El Kacimi⁴, M. Ellert¹⁶⁴, S. Elles⁴, F. Ellinghaus⁸¹, K. Ellis⁷⁵, N. Ellis²⁹, J. Elmsheuser⁹⁸, M. Elsing²⁹, R. Ely¹⁴, D. Emeliyanov¹²⁸, R. Engelmann¹⁴⁶, A. Engl⁹⁸, B. Epp⁶², A. Eppig⁸⁷, V.S. Epshteyn⁹⁵, A. Ereditato¹⁶, D. Eriksson¹⁴⁴, I. Ermoline⁸⁸, J. Ernst¹, M. Ernst²⁴, J. Ernwein¹³⁵, D. Errede¹⁶³, S. Errede¹⁶³, E. Ertel⁸¹, M. Escalier¹¹⁴, C. Escobar¹⁶⁵, X. Espinal Curull¹¹, B. Esposito⁴⁷, F. Etienne⁸³, A.I. Etiennevire¹³⁵, E. Etzion¹⁵¹, H. Evans⁶¹, L. Fabbri^{19a,19b}, C. Fabre²⁹, P. Faccioli^{19a,19b}, K. Facius³⁵, R.M. Fakhruudinov¹²⁷, S. Falciano^{131a}, A.C. Falou¹¹⁴, Y. Fang¹⁷⁰, M. Fanti^{89a,89b}, A. Farbin⁷, A. Farilla^{133a}, J. Farley¹⁴⁶, T. Farooque¹⁵⁶, S.M. Farrington¹¹⁷, P. Farthouat²⁹, F. Fassi¹⁶⁵, P. Fassnacht²⁹, D. Fassouliotis⁸, B. Fatholahzadeh¹⁵⁶, L. Fayard¹¹⁴, F. Fayette⁵⁴, R. Febbraro³³, P. Federic¹⁴³, O.L. Fedin¹²⁰, I. Fedorko²⁹, W. Fedorko²⁹, L. Feligioni⁸³, C.U. Felzmann⁸⁶, C. Feng³², E.J. Feng³⁰, A.B. Fenyuk¹²⁷, J. Ferencei¹⁴³, J. Ferland⁹³, B. Fernandes^{123b}, W. Fernando¹⁰⁸, S. Ferrag⁵³, J. Ferrando¹¹⁷, A. Ferrari¹⁶⁴, P. Ferrari¹⁰⁵, R. Ferrari^{118a}, A. Ferrer¹⁶⁵, M.L. Ferrer⁴⁷, D. Ferrere⁴⁹, C. Ferretti⁸⁷, M. Fiascaris¹¹⁷, F. Fiedler⁸¹, A. Filipčić⁷⁴,

A. Filippas⁹, F. Filthaut¹⁰⁴, M. Fincke-Keeler¹⁶⁷, M.C.N. Fiolhais^{123b}, L. Fiorini¹¹, A. Firan³⁹, G. Fischer⁴¹, M.J. Fisher¹⁰⁸, M. Flechl¹⁶⁴, I. Fleck¹⁴⁰, J. Fleckner⁸¹, P. Fleischmann¹⁷¹, S. Fleischmann²⁰, T. Flick¹⁷², L.R. Flores Castillo¹⁷⁰, M.J. Flowerdew⁹⁹, F. Föhlisch^{58a}, M. Fokitis⁹, T. Fonseca Martin⁷⁶, D.A. Forbush¹³⁷, A. Formica¹³⁵, A. Forti⁸², D. Fortin^{157a}, J.M. Foster⁸², D. Fournier¹¹⁴, A. Foussat²⁹, A.J. Fowler⁴⁴, K. Fowler¹³⁶, H. Fox⁷¹, P. Francavilla^{121a,121b}, S. Franchino^{118a,118b}, D. Francis²⁹, M. Franklin⁵⁷, S. Franz²⁹, M. Fraternali^{118a,118b}, S. Fratina¹¹⁹, J. Freestone⁸², S.T. French²⁷, R. Froeschl²⁹, D. Froidevaux²⁹, J.A. Frost²⁷, C. Fukunaga¹⁵⁴, E. Fullana Torregrosa⁵, J. Fuster¹⁶⁵, C. Gabaldon⁸⁰, O. Gabizon¹⁶⁹, T. Gadfort³⁴, S. Gadomski⁴⁹, G. Gagliardi^{50a,50b}, P. Gagnon⁶¹, C. Galea⁹⁸, E.J. Gallas¹¹⁷, M.V. Gallas²⁹, B.J. Gallop¹²⁸, P. Gallus¹²⁴, E. Galyaev⁴⁰, K.K. Gan¹⁰⁸, Y.S. Gao^{142,l}, A. Gaponenko¹⁴, M. Garcia-Sciveres¹⁴, C. García¹⁶⁵, J.E. García Navarro⁴⁹, R.W. Gardner³⁰, N. Garelli²⁹, H. Garitaonandia¹⁰⁵, V. Garonne²⁹, C. Gatti⁴⁷, G. Gaudio^{118a}, O. Gaumer⁴⁹, P. Gauzzi^{131a,131b}, I.L. Gavrilenko⁹⁴, C. Gay¹⁶⁶, G. Gaycken²⁰, J.-C. Gayde²⁹, E.N. Gazis⁹, P. Ge³², C.N.P. Gee¹²⁸, Ch. Geich-Gimbel²⁰, K. Gellerstedt¹⁴⁴, C. Gemme^{50a}, M.H. Genest⁹⁸, S. Gentile^{131a,131b}, F. Georgatos⁹, S. George⁷⁶, P. Gerlach¹⁷², A. Gershon¹⁵¹, C. Geweniger^{58a}, H. Ghazlane^{134d}, P. Ghez⁴, N. Ghodbane³³, B. Giacobbe^{19a}, S. Giagu^{131a,131b}, V. Giakoumopoulou⁸, V. Giangiobbe^{121a,121b}, F. Gianotti²⁹, B. Gibbard²⁴, A. Gibson¹⁵⁶, S.M. Gibson¹¹⁷, L.M. Gilbert¹¹⁷, M. Gilchriese¹⁴, V. Gilevsky⁹¹, D. Gillberg²⁸, A.R. Gillman¹²⁸, D.M. Gingrich^{2,m}, J. Ginzburg¹⁵¹, N. Giokaris⁸, M.P. Giordani^{162a,162c}, R. Giordano^{102a,102b}, P. Giovannini⁹⁹, P.F. Giraud²⁹, P. Girtler⁶², D. Giugni^{89a}, P. Giusti^{19a}, B.K. Gjølsten¹¹⁶, L.K. Gladilin⁹⁷, C. Glasman⁸⁰, A. Glazov⁴¹, K.W. Glitza¹⁷², G.L. Glonti⁶⁵, J. Godfrey¹⁴¹, J. Godlewski²⁹, M. Goebel⁴¹, T. Göpfert⁴³, C. Goeringer⁸¹, C. Gössling⁴², T. Göttfert⁹⁹, V. Goggi^{118a,118b,n}, S. Goldfarb⁸⁷, D. Goldin³⁹, T. Golling¹⁷³, N.P. Gollub²⁹, A. Gomes^{123b}, L.S. Gomez Fajardo¹⁶⁰, R. Gonçalves⁷⁶, L. Gonella²⁰, C. Gong³², S. González de la Hoz¹⁶⁵, M.L. Gonzalez Silva²⁶, S. Gonzalez-Sevilla⁴⁹, J.J. Goodson¹⁴⁶, L. Goossens²⁹, P.A. Gorbounov¹⁵⁶, H.A. Gordon²⁴, I. Gorelov¹⁰³, G. Gorfine¹⁷², B. Gorini²⁹, E. Gorini^{72a,72b}, A. Gorišek⁷⁴, E. Gornicki³⁸, S.V. Goryachev¹²⁷, V.N. Goryachev¹²⁷, B. Gosdzik⁴¹, M. Gosselink¹⁰⁵, M.I. Gostkin⁶⁵, I. Gough Eschrich¹⁶¹, M. Goughri^{134a}, D. Goujdami^{134a}, M.P. Goulette⁴⁹, A.G. Goussiou¹³⁷, C. Goy⁴, I. Grabowska-Bold^{161,d}, P. Grafström²⁹, K.-J. Grahn¹⁴⁵, L. Granado Cardoso^{123b}, F. Grancagnolo^{72a}, S. Grancagnolo¹⁵, V. Grassi^{89a}, V. Gratchev¹²⁰, N. Grau³⁴, H.M. Gray^{34,o}, J.A. Gray¹⁴⁶, E. Graziani^{133a}, B. Green⁷⁶, T. Greenshaw⁷³, Z.D. Greenwood^{24,i}, I.M. Gregor⁴¹, P. Grenier¹⁴², E. Griesmayer⁴⁶, J. Griffiths¹³⁷, N. Grigalashvili⁶⁵, A.A. Grillo¹³⁶, K. Grimm¹⁴⁶, S. Grinstein¹¹, Y.V. Grishkevich⁹⁷, L.S. Groer¹⁵⁶, J. Grognez²⁹, M. Groh⁹⁹, M. Groll⁸¹, E. Gross¹⁶⁹, J. Grosse-Knetter⁵⁴, J. Groth-Jensen⁷⁹, K. Grybel¹⁴⁰, V.J. Guarino⁵, C. Guicheney³³, A. Guida^{72a,72b}, T. Guillemin⁴, H. Guler^{85,p}, J. Gunther¹²⁴, B. Guo¹⁵⁶, A. Gupta³⁰, Y. Gusakov⁶⁵, A. Gutierrez⁹³, P. Gutierrez¹¹⁰, N. Guttman¹⁵¹, O. Gutzwiller²⁹, C. Guyot¹³⁵, C. Gwenlan¹¹⁷, C.B. Gwilliam⁷³, A. Haas¹⁴², S. Haas²⁹, C. Haber¹⁴, R. Hackenburg²⁴, H.K. Hadavand³⁹, D.R. Hadley¹⁷, P. Haefner⁹⁹, R. Härtel⁹⁹, Z. Hajduk³⁸, H. Hakobyan¹⁷⁴, J. Haller^{41,q}, K. Hamacher¹⁷², A. Hamilton⁴⁹, S. Hamilton¹⁵⁹, H. Han³², L. Han³², K. Hanagaki¹¹⁵, M. Hance¹¹⁹, C. Handel⁸¹, P. Hanke^{58a}, J.R. Hansen³⁵, J.B. Hansen³⁵, J.D. Hansen³⁵, P.H. Hansen³⁵, T. Hansl-Kozanecka¹³⁶, P. Hansson¹⁴², K. Hara¹⁵⁸, G.A. Hare¹³⁶, T. Harenberg¹⁷², R.D. Harrington²¹, O.B. Harris⁷⁷, O.M. Harris¹³⁷, K. Harrison¹⁷, J. Hartert⁴⁸, F. Hartjes¹⁰⁵, T. Haruyama⁶⁶, A. Harvey⁵⁶, S. Hasegawa¹⁰¹, Y. Hasegawa¹³⁹, K. Hashemi²², S. Hassani¹³⁵, M. Hatch²⁹, F. Haug²⁹, S. Haug¹⁶, M. Hauschild²⁹, R. Hauser⁸⁸, M. Havranek¹²⁴, C.M. Hawkes¹⁷, R.J. Hawkins²⁹, D. Hawkins¹⁶¹, T. Hayakawa⁶⁷, H.S. Hayward⁷³, S.J. Haywood¹²⁸, M. He³², S.J. Head⁸², V. Hedberg⁷⁹, L. Heelan²⁸, S. Heim⁸⁸, B. Heinemann¹⁴, S. Heisterkamp³⁵, L. Helary⁴, M. Heller¹¹⁴, S. Hellman¹⁴⁴, C. Helsens¹¹, T. Hemperek²⁰, R.C.W. Henderson⁷¹, M. Henke^{58a}, A. Henrichs⁵⁴, A.M. Henriques Correia²⁹, S. Henrot-Versille¹¹⁴, C. Hensel⁵⁴, T. Henß¹⁷², A.D. Hershenhorn¹⁵⁰, G. Hertel⁴⁸, R. Hertenberger⁹⁸, L. Hervas²⁹, N.P. Hessey¹⁰⁵, A. Hidvegi¹⁴⁴, E. Higón-Rodríguez¹⁶⁵, D. Hill^{5,*}, J.C. Hill²⁷, K.H. Hiller⁴¹, S.J. Hillier¹⁷, I. Hinchliffe¹⁴, M. Hirose¹¹⁵, F. Hirsch⁴², J. Hobbs¹⁴⁶, N. Hod¹⁵¹, M.C. Hodgkinson¹³⁸, P. Hodgson¹³⁸, A. Hoecker²⁹, M.R. Hoefkamp¹⁰³, J. Hoffman³⁹, D. Hoffmann⁸³, M. Hohlfeld⁸¹, S.O. Holmgren¹⁴⁴, T. Holy¹²⁶, J.L. Holzbauer⁸⁸, Y. Homma⁶⁷, P. Homola¹²⁶, T. Horazdovsky¹²⁶, T. Hori⁶⁷, C. Horn¹⁴², S. Horner⁴⁸, S. Horvat⁹⁹, J.-Y. Hostachy⁵⁵, S. Hou¹⁴⁹, M.A. Houlden⁷³, A. Hoummada^{134a}, T. Howe³⁹, J. Hrivnac¹¹⁴, T. Hryn'ova⁴, P.J. Hsu¹⁷³, S.-C. Hsu¹⁴, G.S. Huang¹¹⁰, Z. Hubacek¹²⁶, F. Hubaut⁸³, F. Huegging²⁰, E.W. Hughes³⁴, G. Hughes⁷¹, R.E. Hughes-Jones⁸², P. Hurst⁵⁷, M. Hurwitz³⁰, U. Husemann⁴¹, N. Huseynov¹⁰, J. Huston⁸⁸, J. Huth⁵⁷, G. Iacobucci^{102a}, G. Iakovidis⁹, I. Ibragimov¹⁴⁰, L. Iconomidou-Fayard¹¹⁴, J. Idarraga^{157b}, P. Iengo⁴, O. Igonkina¹⁰⁵, Y. Ikegami⁶⁶, M. Ikono⁶⁶, Y. Ilchenko³⁹, D. Iliadis¹⁵², Y. Ilyushenka⁶⁵, M. Imori¹⁵³, T. Ince¹⁶⁷, P. Ioannou⁸, M. Iodice^{133a}, A. Irls Quiles¹⁶⁵, A. Ishikawa⁶⁷, M. Ishino⁶⁶, R. Ishmukhametov³⁹, T. Isobe¹⁵³, V. Issakov^{173,*}, C. Issever¹¹⁷, S. Istin¹⁸, Y. Itoh¹⁰¹, A.V. Ivashin¹²⁷, W. Iwanski³⁸, H. Iwasaki⁶⁶, J.M. Izen⁴⁰, V. Izzo^{102a}, J.N. Jackson⁷³, P. Jackson¹⁴², M. Jaekel²⁹, M. Jahoda¹²⁴, V. Jain⁶¹, K. Jakobs⁴⁸, S. Jakobsen²⁹, J. Jakubek¹²⁶, D. Jana¹¹⁰, E. Jansen¹⁰⁴, A. Jantsch⁹⁹, M. Janus⁴⁸, R.C. Jared¹⁷⁰, G. Jarlskog⁷⁹, P. Jarron²⁹, L. Jeanty⁵⁷, K. Jelen³⁷, I. Jen-La Plante³⁰, P. Jenni²⁹, P. Jez³⁵, S. Jézéquel⁴, W. Ji⁷⁹, J. Jia¹⁴⁶, Y. Jiang³², M. Jimenez Belenguer²⁹, G. Jin³², S. Jin³², O. Jinnouchi¹⁵⁵, D. Joffe³⁹, M. Johansen¹⁴⁴, K.E. Johansson¹⁴⁴, P. Johansson¹³⁸, S. Johnert⁴¹, K.A. Johns⁶, K. Jon-And¹⁴⁴, G. Jones⁸², R.W.L. Jones⁷¹, T.W. Jones⁷⁷, T.J. Jones⁷³, O. Jonsson²⁹, D. Joos⁴⁸, C. Joram²⁹, P.M. Jorge^{123b}, V. Juranek¹²⁴, P. Jussel⁶², V.V. Kabachenko¹²⁷, S. Kabana¹⁶, M. Kaci¹⁶⁵, A. Kaczmarek³⁸, M. Kado¹¹⁴, H. Kagan¹⁰⁸, M. Kagan⁵⁷, S. Kaiser⁹⁹, E. Kajomovitz¹⁵⁰, L.V. Kalinovskaya⁶⁵, A. Kalinowski¹²⁹, S. Kama⁴¹, N. Kanaya¹⁵³, M. Kaneda¹⁵³, V.A. Kantserov⁹⁶, J. Kanzaki⁶⁶, B. Kaplan¹⁷³,

A. Kapliy³⁰, J. Kaplon²⁹, M. Karagounis²⁰, M. Karagoz Unel¹¹⁷, V. Kartvelishvili⁷¹, A.N. Karyukhin¹²⁷,
 L. Kashif⁵⁷, A. Kasmi³⁹, R.D. Kass¹⁰⁸, A. Kastanas¹³, M. Kastoryano¹⁷³, M. Kataoka²⁹, Y. Kataoka¹⁵³,
 E. Katsoufis⁹, J. Katzy⁴¹, V. Kaushik⁶, K. Kawagoe⁶⁷, T. Kawamoto¹⁵³, G. Kawamura⁸¹, M.S. Kayl¹⁰⁵,
 F. Kayumov⁹⁴, V.A. Kazanin¹⁰⁶, M.Y. Kazarinov⁶⁵, S.I. Kazi⁸⁶, J.R. Keates⁸², R. Keeler¹⁶⁷, P.T. Keener¹¹⁹,
 R. Kehoe³⁹, M. Keil⁴⁹, G.D. Kekelidze⁶⁵, M. Kelly⁸², J. Kennedy⁹⁸, M. Kenyon⁵³, O. Kepka¹³⁵, N. Kerschen²⁹,
 B.P. Kerševan⁷⁴, S. Kersten¹⁷², K. Kessoku¹⁵³, M. Khakzad²⁸, F. Khalil-zada¹⁰, H. Khandanyan¹⁶³, A. Khanov¹¹¹,
 D. Kharchenko⁶⁵, A. Khodinov¹⁴⁶, A.G. Kholodenko¹²⁷, A. Khomich^{58a}, G. Khorauli²⁰, N. Khovanskiy⁶⁵,
 V. Khovanskiy⁹⁵, E. Khramov⁶⁵, J. Khubua⁵¹, G. Kilvington⁷⁶, H. Kim⁷, M.S. Kim², P.C. Kim¹⁴², S.H. Kim¹⁵⁸,
 O. Kind¹⁵, P. Kind¹⁷², B.T. King⁷³, J. Kirk¹²⁸, G.P. Kirsch¹¹⁷, L.E. Kirsch²², A.E. Kiryunin⁹⁹, D. Kisielewska³⁷,
 T. Kittelmann¹²², H. Kiyamura⁶⁷, E. Kladiva¹⁴³, M. Klein⁷³, U. Klein⁷³, K. Kleinknecht⁸¹, M. Klemetti⁸⁵,
 A. Klier¹⁶⁹, A. Klimentov²⁴, R. Klingenberg⁴², E.B. Klinkby⁴⁴, T. Klioutchnikova²⁹, P.F. Klok¹⁰⁴, S. Klous¹⁰⁵,
 E.-E. Kluge^{58a}, T. Kluge⁷³, P. Kluitt¹⁰⁵, M. Klute⁵⁴, S. Kluth⁹⁹, N.S. Knecht¹⁵⁶, E. Kneringer⁶², B.R. Ko⁴⁴,
 T. Kobayashi¹⁵³, M. Kobel⁴³, B. Koblitze²⁹, M. Kocian¹⁴², A. Kocnar¹¹², P. Kodys¹²⁵, K. Köneke⁴¹, A.C. König¹⁰⁴,
 L. Köpke⁸¹, F. Koetsveld¹⁰⁴, P. Koevesarki²⁰, T. Koffas²⁹, E. Koffeman¹⁰⁵, F. Kohn⁵⁴, Z. Kohout¹²⁶, T. Kohriki⁶⁶,
 T. Kokott²⁰, H. Kolanoski¹⁵, V. Kolesnikov⁶⁵, I. Koletsou⁴, J. Koll⁸⁸, D. Kollar²⁹, S. Kolos^{161,r}, S.D. Kolya⁸²,
 A.A. Komar⁹⁴, J.R. Komaragiri¹⁴¹, T. Kondo⁶⁶, T. Kono^{41,q}, A.I. Kononov⁴⁸, R. Konoplich¹⁰⁷, S.P. Kononov⁹⁴,
 N. Konstantinidis⁷⁷, S. Koperny³⁷, K. Korcyl³⁸, K. Kordas¹⁶, V. Koreshev¹²⁷, A. Korn¹⁴, I. Korolkov¹¹,
 E.V. Korolkova¹³⁸, V.A. Korotkov¹²⁷, O. Kortner⁹⁹, P. Kostka⁴¹, V.V. Kostyukhin²⁰, M.J. Kotamäki²⁹, S. Kotov⁹⁹,
 V.M. Kotov⁶⁵, K.Y. Kotov¹⁰⁶, Z. Koupilova¹²⁵, C. Kourkouvelis⁸, A. Koutsman¹⁰⁵, R. Kowalewski¹⁶⁷,
 H. Kowalski⁴¹, T.Z. Kowalski³⁷, W. Kozanecki¹³⁵, A.S. Kozhin¹²⁷, V. Kral¹²⁶, V.A. Kramarenko⁹⁷, G. Kramberger⁷⁴,
 M.W. Krasny⁷⁸, A. Krasznahorkay¹⁰⁷, A. Kreisel¹⁵¹, F. Krejci¹²⁶, A. Krepouri¹⁵², J. Kretzschmar⁷³, P. Krieger¹⁵⁶,
 G. Krobath⁹⁸, K. Kroeninger⁵⁴, H. Kroha⁹⁹, J. Kroll¹¹⁹, J. Kroseberg²⁰, J. Krstic^{12a}, U. Kruchonak⁶⁵, H. Krüger²⁰,
 Z.V. Krumshteyn⁶⁵, T. Kubota¹⁵³, S. Kuehn⁴⁸, A. Kugel^{58c}, T. Kuhl¹⁷², D. Kuhn⁶², V. Kukhtin⁶⁵, Y. Kulchitsky⁹⁰,
 S. Kuleshov^{31b}, C. Kummer⁹⁸, M. Kuna⁸³, A. Kupco¹²⁴, H. Kurashige⁶⁷, M. Kurata¹⁵⁸, L.L. Kurchaninov^{157a},
 Y.A. Kurochkin⁹⁰, V. Kus¹²⁴, W. Kuykendall¹³⁷, E. Kuznetsova^{131a,131b}, O. Kvasnicka¹²⁴, R. Kwee¹⁵, M. La Rosa⁸⁶,
 L. La Rotonda^{36a,36b}, L. Labarga⁸⁰, J. Labbe⁴, C. Lacasta¹⁶⁵, F. Lacava^{131a,131b}, H. Lacker¹⁵, D. Lacour⁷⁸,
 V.R. Lacuesta¹⁶⁵, E. Ladygin⁶⁵, R. Lafaye⁴, B. Laforge⁷⁸, T. Lagouri⁸⁰, S. Lai⁴⁸, M. Lamanna²⁹, C.L. Lampen⁶,
 W. Lampf⁶, E. Lancon¹³⁵, U. Landgraf⁴⁸, M.P.J. Landon⁷⁵, J.L. Lane⁸², A.J. Lankford¹⁶¹, F. Lanni²⁴, K. Lantzsch²⁹,
 A. Lanza^{118a}, S. Laplace⁴, C. Lapoire⁸³, J.F. Laporte¹³⁵, T. Lari^{89a}, A.V. Larionov¹²⁷, A. Larner¹¹⁷, C. Lasseur²⁹,
 M. Lassnig²⁹, P. Laurelli⁴⁷, W. Lavrijsen¹⁴, P. Laycock⁷³, A.B. Lazarev⁶⁵, A. Lazzaro^{89a,89b}, O. Le Dortz⁷⁸,
 E. Le Guirriec⁸³, C. Le Maner¹⁵⁶, E. Le Menedeu¹³⁵, M. Le Vine²⁴, M. Leahu²⁹, A. Lebedev⁶⁴, C. Lebel⁹³,
 T. LeCompte⁵, F. Ledroit-Guillon⁵⁵, H. Lee¹⁰⁵, J.S.H. Lee¹⁴⁸, S.C. Lee¹⁴⁹, M. Lefebvre¹⁶⁷, M. Legendre¹³⁵,
 B.C. LeGeyt¹¹⁹, F. Legger⁹⁸, C. Leggett¹⁴, M. Lehmacher²⁰, G. Lehmann Miotto²⁹, X. Lei⁶, R. Leitner¹²⁵,
 D. Lelas¹⁶⁷, D. Lellouch¹⁶⁹, J. Lellouch⁷⁸, M. Leltchouk³⁴, V. Lendermann^{58a}, K.J.C. Leney⁷³, T. Lenz¹⁷²,
 G. Lenzen¹⁷², B. Lenzi¹³⁵, K. Leonhardt⁴³, C. Leroy⁹³, J.-R. Lessard¹⁶⁷, C.G. Lester²⁷, A. Leung Fook Cheong¹⁷⁰,
 J. Levêque⁸³, D. Levin⁸⁷, L.J. Levinson¹⁶⁹, M.S. Levitski¹²⁷, S. Levonian⁴¹, M. Lewandowska²¹, M. Leyton¹⁴,
 H. Li¹⁷⁰, J. Li⁷, S. Li⁴¹, X. Li⁸⁷, Z. Liang³⁹, Z. Liang^{149,s}, B. Liberti^{132a}, P. Lichard²⁹, M. Lichtnecker⁹⁸, K. Lie¹⁶³,
 W. Liebig¹⁰⁵, D. Liko²⁹, J.N. Lilley¹⁷, H. Lim⁵, A. Limosani⁸⁶, M. Limper⁶³, S.C. Lin¹⁴⁹, S.W. Lindsay⁷³,
 V. Linhart¹²⁶, J.T. Linnemann⁸⁸, A. Liolios¹⁵², E. Lipeles¹¹⁹, L. Lipinsky¹²⁴, A. Lipniacka¹³, T.M. Liss¹⁶³,
 D. Lissauer²⁴, A.M. Litke¹³⁶, C. Liu²⁸, D. Liu^{149,t}, H. Liu⁸⁷, J.B. Liu⁸⁷, M. Liu³², S. Liu², T. Liu³⁹, Y. Liu³²,
 M. Livan^{118a,118b}, A. Lleres⁵⁵, S.L. Lloyd⁷⁵, E. Lobodzinska⁴¹, P. Loch⁶, W.S. Lockman¹³⁶, S. Lockwitz¹⁷³,
 T. Loddenkoetter²⁰, F.K. Loebinger⁸², A. Loginov¹⁷³, C.W. Loh¹⁶⁶, T. Lohse¹⁵, K. Lohwasser⁴⁸, M. Lokajicek¹²⁴,
 J. Loken¹¹⁷, L. Lopes^{123b}, D. Lopez Mateos^{34,o}, M. Losada¹⁶⁰, P. Loscutoff¹⁴, M.J. Losty^{157a}, X. Lou⁴⁰, A. Lounis¹¹⁴,
 K.F. Loureiro¹⁰⁸, L. Lovas¹⁴³, J. Love²¹, P. Love⁷¹, A.J. Lowe⁶¹, F. Lu³², J. Lu², H.J. Lubatti¹³⁷, C. Luci^{131a,131b},
 A. Lucotte⁵⁵, A. Ludwig⁴³, D. Ludwig⁴¹, I. Ludwig⁴⁸, J. Ludwig⁴⁸, F. Luehring⁶¹, L. Luisa^{162a,162c}, D. Lumb⁴⁸,
 L. Luminari^{131a}, E. Lund¹¹⁶, B. Lund-Jensen¹⁴⁵, B. Lundberg⁷⁹, J. Lundberg²⁹, J. Lundquist³⁵, G. Lutz⁹⁹, D. Lynn²⁴,
 J. Lys¹⁴, E. Lytken⁷⁹, H. Ma²⁴, L.L. Ma¹⁷⁰, G. Maccarrone⁴⁷, A. Macchiolo⁹⁹, B. Maček⁷⁴, J. Machado Miguens^{123b},
 R. Mackeprang²⁹, R.J. Madaras¹⁴, W.F. Mader⁴³, R. Maenner^{58c}, T. Maeno²⁴, P. Mättig¹⁷², S. Mättig⁴¹,
 P.J. Magalhaes Martins^{123b}, E. Magradze⁵¹, C.A. Magrath¹⁰⁴, Y. Mahalalel¹⁵¹, K. Mahboubi⁴⁸, A. Mahmood¹,
 G. Mahout¹⁷, C. Maiani^{131a,131b}, C. Maidantchik^{23a}, A. Maio^{123b}, S. Majewski²⁴, Y. Makida⁶⁶, M. Makouski¹²⁷,
 N. Makovec¹¹⁴, Pa. Malecki³⁸, P. Malecki³⁸, V.P. Maleev¹²⁰, F. Malek⁵⁵, U. Mallik⁶³, D. Malon⁵, S. Maltezos⁹,
 V. Malyshev¹⁰⁶, S. Malyukov⁶⁵, M. Mambelli³⁰, R. Mameghani⁹⁸, J. Mamuzic⁴¹, A. Manabe⁶⁶, L. Mandelli^{89a},
 I. Mandić⁷⁴, R. Mandrysch¹⁵, J. Maneira^{123b}, P.S. Mangeard⁸⁸, I.D. Manjavidze⁶⁵, A. Manousakis-Katsikakis⁸,
 B. Mansoulie¹³⁵, A. Mapelli²⁹, L. Mapelli²⁹, L. March⁸⁰, J.F. Marchand⁴, F. Marchese^{132a,132b}, M. Marcisovsky¹²⁴,
 C.P. Marino⁶¹, C.N. Marques^{123b}, F. Marroquim^{23a}, R. Marshall⁸², Z. Marshall^{34,o}, F.K. Martens¹⁵⁶,
 S. Marti i Garcia¹⁶⁵, A.J. Martin⁷⁵, A.J. Martin¹⁷³, B. Martin²⁹, B. Martin⁸⁸, F.F. Martin¹¹⁹, J.P. Martin⁹³,
 T.A. Martin¹⁷, B. Martin dit Latour⁴⁹, M. Martinez¹¹, V. Martinez Outschoorn⁵⁷, A. Martini⁴⁷, V. Martynenko^{157b},
 A.C. Martyniuk⁸², T. Maruyama¹⁵⁸, F. Marzano^{131a}, A. Marzin¹³⁵, L. Masetti²⁰, T. Mashimo¹⁵³, R. Mashinistov⁹⁶,
 J. Masik⁸², A.L. Maslennikov¹⁰⁶, G. Massaro¹⁰⁵, N. Massol⁴, A. Mastroberardino^{36a,36b}, T. Masubuchi¹⁵³,

M. Mathes²⁰, P. Matricon¹¹⁴, H. Matsumoto¹⁵³, H. Matsunaga¹⁵³, T. Matsushita⁶⁷, C. Mattravers^{117,u}, S.J. Maxfield⁷³, E.N. May⁵, A. Mayne¹³⁸, R. Mazini¹⁴⁹, M. Mazur⁴⁸, M. Mazzanti^{89a,89b}, P. Mazzanti^{19a}, J. Mc Donald⁸⁵, S.P. Mc Kee⁸⁷, A. McCarn¹⁶³, R.L. McCarthy¹⁴⁶, N.A. McCubbin¹²⁸, K.W. McFarlane⁵⁶, H. McGlone⁵³, G. Mchedlidze⁵¹, R.A. McLaren²⁹, S.J. McMahon¹²⁸, T.R. McMahon⁷⁶, R.A. McPherson^{167,h}, A. Meade⁸⁴, J. Mechnich¹⁰⁵, M. Mechtel¹⁷², M. Medinnis⁴¹, R. Meera-Lebbai¹¹⁰, T.M. Meguro¹¹⁵, R. Mehdiyev⁹³, S. Mehlhase⁴¹, A. Mehta⁷³, K. Meier^{58a}, B. Meirose⁴⁸, A. Melamed-Katz¹⁶⁹, B.R. Mellado Garcia¹⁷⁰, Z. Meng^{149,t}, S. Menke⁹⁹, E. Meoni¹¹, D. Merkl⁹⁸, P. Mermod¹¹⁷, L. Merola^{102a,102b}, C. Meroni^{89a}, F.S. Merritt³⁰, A.M. Messina²⁹, I. Messmer⁴⁸, J. Metcalfe¹⁰³, A.S. Mete⁶⁴, J-P. Meyer¹³⁵, J. Meyer⁵⁴, T.C. Meyer²⁹, W.T. Meyer⁶⁴, J. Miao³², L. Micu^{25a}, R.P. Middleton¹²⁸, S. Migas⁷³, L. Mijović⁷⁴, G. Mikenberg¹⁶⁹, M. Mikuz⁷⁴, D.W. Miller¹⁴², W.J. Mills¹⁶⁶, C.M. Mills⁵⁷, A. Milov¹⁶⁹, D.A. Milstead¹⁴⁴, A.A. Minaenko¹²⁷, M. Miñano¹⁶⁵, I.A. Minashvili⁶⁵, A.I. Mincer¹⁰⁷, B. Mindur³⁷, M. Mineev⁶⁵, L.M. Mir¹¹, G. Mirabelli^{131a}, S. Misawa²⁴, S. Miscetti⁴⁷, A. Misiejuk⁷⁶, J. Mitrevski¹³⁶, V.A. Mitsou¹⁶⁵, P.S. Miyagawa⁸², J.U. Mjörnmark⁷⁹, D. Mladenov²², T. Moa¹⁴⁴, P. Mockett¹³⁷, S. Moed⁵⁷, V. Moeller²⁷, K. Mönig⁴¹, N. Möser²⁰, B. Mohn¹³, W. Mohr⁴⁸, S. Mohrdieck-Möck⁹⁹, R. Moles-Valls¹⁶⁵, J. Molina-Perez²⁹, G. Moloney⁸⁶, J. Monk⁷⁷, E. Monnier⁸³, S. Montesano^{89a,89b}, F. Monticelli⁷⁰, R.W. Moore², C. Mora Herrera⁴⁹, A. Moraes⁵³, A. Morais^{123b}, J. Morel⁴, G. Morello^{36a,36b}, D. Moreno¹⁶⁰, M. Moreno Llacer¹⁶⁵, P. Morettini^{50a}, M. Morii⁵⁷, A.K. Morley⁸⁶, G. Mornacchi²⁹, S.V. Morozov⁹⁶, J.D. Morris⁷⁵, H.G. Moser⁹⁹, M. Mosidze⁵¹, J. Moss¹⁰⁸, R. Mount¹⁴², E. Mountricha⁹, S.V. Mouraviev⁹⁴, E.J.W. Moyse⁸⁴, M. Mudrinic^{12b}, F. Mueller^{58a}, J. Mueller¹²², K. Mueller²⁰, T.A. Müller⁹⁸, D. Muenstermann⁴², A. Muir¹⁶⁶, R. Murrillo Garcia¹⁶¹, W.J. Murray¹²⁸, I. Mussche¹⁰⁵, E. Musto^{102a,102b}, A.G. Myagkov¹²⁷, M. Myska¹²⁴, J. Nadal¹¹, K. Nagai²⁴, K. Nagano⁶⁶, Y. Nagasaka⁶⁰, A.M. Nairz²⁹, K. Nakamura¹⁵³, I. Nakano¹⁰⁹, H. Nakatsuka⁶⁷, G. Nanava²⁰, A. Napier¹⁵⁹, M. Nash^{77,v}, N.R. Nation²¹, T. Nattermann²⁰, T. Naumann⁴¹, G. Navarro¹⁶⁰, S.K. Nderitu²⁰, H.A. Neal⁸⁷, E. Nebot⁸⁰, P. Nechaeva⁹⁴, A. Negri^{118a,118b}, G. Negri²⁹, A. Nelson⁶⁴, T.K. Nelson¹⁴², S. Nemecek¹²⁴, P. Nemethy¹⁰⁷, A.A. Nepomuceno^{23a}, M. Nessi²⁹, M.S. Neubauer¹⁶³, A. Neusiedl⁸¹, R.N. Neves^{123b}, P. Nevski²⁴, F.M. Newcomer¹¹⁹, C. Nicholson⁵³, R.B. Nickerson¹¹⁷, R. Nicolaidou¹³⁵, L. Nicolas¹³⁸, G. Nicoletti⁴⁷, F. Niedercorn¹¹⁴, J. Nielsen¹³⁶, A. Nikiforov¹⁵, K. Nikolaev⁶⁵, I. Nikolic-Audit⁷⁸, K. Nikolopoulos⁸, H. Nilsen⁴⁸, P. Nilsson⁷, A. Nisati^{131a}, T. Nishiyama⁶⁷, R. Nisius⁹⁹, L. Nodulman⁵, M. Nomachi¹¹⁵, I. Nomidis¹⁵², H. Nomoto¹⁵³, M. Nordberg²⁹, B. Nordkvist¹⁴⁴, D. Notz⁴¹, J. Novakova¹²⁵, M. Nozaki⁶⁶, M. Nožička⁴¹, I.M. Nugent^{157a}, A.-E. Nuncio-Quiroz²⁰, G. Nunes Hanninger²⁰, T. Nunnemann⁹⁸, E. Nurse⁷⁷, D.C. O'Neil¹⁴¹, V. O'Shea⁵³, F.G. Oakham^{28,b}, H. Oberlack⁹⁹, A. Ochi⁶⁷, S. Oda¹⁵³, S. Odaka⁶⁶, J. Odier⁸³, G.A. Odino^{50a,50b}, H. Ogren⁶¹, S.H. Oh⁴⁴, C.C. Ohm¹⁴⁴, T. Ohshima¹⁰¹, H. Ohshita¹³⁹, T. Ohsugi⁵⁹, S. Okada⁶⁷, H. Okawa¹⁵³, Y. Okumura¹⁰¹, M. Olcese^{50a}, A.G. Olchevski⁶⁵, M. Oliveira^{123b}, D. Oliveira Damazio²⁴, J. Oliver⁵⁷, E. Oliver Garcia¹⁶⁵, D. Olivito¹¹⁹, A. Olszewski³⁸, J. Olszowski³⁸, C. Omachi⁶⁷, A. Onofre^{123b}, P.U.E. Onyisi³⁰, C.J. Oram^{157a}, G. Ordóñez¹⁰⁴, M.J. Oreglia³⁰, Y. Oren¹⁵¹, D. Orestano^{133a,133b}, I. Orlov¹⁰⁶, C. Oropeza Barrera⁵³, R.S. Orr¹⁵⁶, E.O. Ortega¹²⁹, B. Osculati^{50a,50b}, C. Osuna¹¹, R. Otec¹²⁶, J.P. Ottersbach¹⁰⁵, F. Ould-Saada¹¹⁶, A. Ouraou¹³⁵, Q. Ouyang³², M. Owen⁸², S. Owen¹³⁸, V.E. Ozcan⁷⁷, K. Ozone⁶⁶, N. Ozturk⁷, A. Pacheco Pages¹¹, S. Padhi¹⁷⁰, C. Padilla Aranda¹¹, E. Paganis¹³⁸, C. Pahl⁶³, F. Paige²⁴, K. Pajchel¹¹⁶, A. Pal⁷, S. Palestini²⁹, D. Pallin³³, A. Palma^{123b}, J.D. Palmer¹⁷, Y.B. Pan¹⁷⁰, E. Panagiotopoulou⁹, B. Panes^{31a}, N. Panikashvili⁸⁷, S. Panitkin²⁴, D. Pantea^{25a}, M. Panuskova¹²⁴, V. Paolone¹²², Th.D. Papadopoulou⁹, S.J. Park⁵⁴, W. Park^{24,w}, M.A. Parker²⁷, S.I. Parker¹⁴, F. Parodi^{50a,50b}, J.A. Parsons³⁴, U. Parzefall⁴⁸, E. Pasqualucci^{131a}, G. Passardi²⁹, A. Passeri^{133a}, F. Pastore^{133a,133b}, Fr. Pastore²⁹, G. Pásztor^{49,x}, S. Patariaia⁹⁹, J.R. Pater⁸², S. Patricelli^{102a,102b}, A. Patwa²⁴, T. Pauly²⁹, L.S. Peak¹⁴⁸, M. Pecsý¹⁴³, M.I. Pedraza Morales¹⁷⁰, S.V. Peleganchuk¹⁰⁶, H. Peng¹⁷⁰, A. Penson³⁴, J. Penwell⁶¹, M. Perantoni^{23a}, K. Perez^{34,o}, E. Perez Codina¹¹, M.T. Pérez García-Estañ¹⁶⁵, V. Perez Reale³⁴, L. Perini^{89a,89b}, H. Pernegger²⁹, R. Perrino^{72a}, P. Perrodo⁴, S. Persebe³, P. Perus¹¹⁴, V.D. Peshekhonov⁶⁵, B.A. Petersen²⁹, J. Petersen²⁹, T.C. Petersen³⁵, E. Petit⁸³, C. Petridou¹⁵², E. Petrolo^{131a}, F. Petrucci^{133a,133b}, D. Petschull⁴¹, M. Petteni¹⁴¹, R. Pezoa^{31b}, B. Pfeifer⁴⁸, A. Phan⁸⁶, A.W. Phillips²⁷, G. Piacquadio⁴⁸, M. Piccinini^{19a,19b}, R. Piegai²⁶, J.E. Pilcher³⁰, A.D. Pilkington⁸², J. Pina^{123b}, M. Pinamonti^{162a,162c}, J.L. Pinfeld², J. Ping³², B. Pinto^{123b}, O. Pirotte²⁹, C. Pizio^{89a,89b}, R. Placakyte⁴¹, M. Plamondon¹⁶⁷, W.G. Plano⁸², M.-A. Pleier²⁴, A. Poblaguev¹⁷³, S. Poddar^{58a}, F. Podlyski³³, P. Poffenberger¹⁶⁷, L. Poggioli¹¹⁴, M. Pohl⁴⁹, F. Polci⁵⁵, G. Polesello^{118a}, A. Policicchio¹³⁷, A. Polini^{19a}, J. Poll⁷⁵, V. Polychronakos²⁴, D.M. Pomarede¹³⁵, D. Pomeroy²², K. Pommès²⁹, L. Pontecorvo^{131a}, B.G. Pope⁸⁸, D.S. Popovic^{12a}, A. Poppleton²⁹, J. Popule¹²⁴, X. Portell Bueso⁴⁸, R. Porter¹⁶¹, G.E. Pospelov⁹⁹, P. Pospichal²⁹, S. Pospisil¹²⁶, M. Potekhin²⁴, I.N. Potrap⁹⁹, C.J. Potter¹⁴⁷, C.T. Potter⁸⁵, K.P. Potter⁸², G. Poulard²⁹, J. Poveda¹⁷⁰, R. Prabhu²⁰, P. Pralavorio⁸³, S. Prasad⁵⁷, R. Pravahan⁷, T. Preda^{25a}, K. Pretzl¹⁶, L. Pribyl²⁹, D. Price⁶¹, L.E. Price⁵, P.M. Prichard⁷³, D. Prieur¹²², M. Primavera^{72a}, K. Prokofiev²⁹, F. Prokoshin^{31b}, S. Protopopescu²⁴, J. Proudfoot⁵, X. Prudent⁴³, H. Przysiecki⁴, S. Psoroulas²⁰, E. Ptacek¹¹³, C. Puigdemonts¹¹, J. Purdham⁸⁷, M. Purohit^{24,w}, P. Puzo¹¹⁴, Y. Pylypchenko¹¹⁶, M. Qi³², J. Qian⁸⁷, W. Qian¹²⁸, Z. Qian⁸³, Z. Qin⁴¹, D. Qing^{157a}, A. Quadt⁵⁴, D.R. Quarrie¹⁴, W.B. Quayle¹⁷⁰, F. Quinonez^{31a}, M. Raas¹⁰⁴, V. Radeka²⁴, V. Radescu^{58b}, B. Radics²⁰, T. Rador¹⁸, F. Ragusa^{89a,89b}, G. Rahal¹⁷⁸, A.M. Rahimi¹⁰⁸, D. Rahm²⁴, S. Rajagopalan²⁴, M. Rammes¹⁴⁰, P.N. Ratoff⁷¹, F. Rauscher⁹⁸, E. Rauter⁹⁹, M. Raymond²⁹, A.L. Read¹¹⁶, D.M. Rebuzzi^{118a,118b}, A. Redelbach¹⁷¹, G. Redlinger²⁴, R. Reece¹¹⁹, K. Reeves¹⁷², E. Reinherz-Aronis¹⁵¹, A. Reinsch¹¹³, I. Reisinger⁴², D. Reljic^{12a}, C. Rembser²⁹, Z.L. Ren¹⁴⁹,

P. Renkel³⁹, S. Rescia²⁴, M. Rescigno^{131a}, S. Resconi^{89a}, B. Resende¹⁰⁵, P. Reznicek¹²⁵, R. Rezvani¹⁵⁶, A. Richards⁷⁷, R.A. Richards⁸⁸, D. Richter¹⁵, R. Richter⁹⁹, E. Richter-Was^{38,y}, M. Ridel⁷⁸, S. Rieke⁸¹, M. Rijpstra¹⁰⁵, M. Rijssenbeek¹⁴⁶, A. Rimoldi^{118a,118b}, L. Rinaldi^{19a}, R.R. Rios³⁹, I. Riu¹¹, G. Rivoltella^{89a,89b}, F. Rizatdinova¹¹¹, E.R. Rizvi⁷⁵, D.A. Roa Romero¹⁶⁰, S.H. Robertson^{85,h}, A. Robichaud-Veronneau⁴⁹, D. Robinson²⁷, M. Robinson¹¹³, A. Robson⁵³, J.G. Rocha de Lima⁵, C. Roda^{121a,121b}, D. Rodriguez¹⁶⁰, Y. Rodriguez Garcia¹⁵, S. Roe²⁹, O. Röhne¹¹⁶, V. Rojo¹, S. Rolli¹⁵⁹, A. Romaniouk⁹⁶, V.M. Romanov⁶⁵, G. Romeo²⁶, D. Romero Maltrana^{31a}, L. Roos⁷⁸, E. Ros¹⁶⁵, S. Rosati^{131a,131b}, G.A. Rosenbaum¹⁵⁶, E.I. Rosenberg⁶⁴, L. Rosselet⁴⁹, L.P. Rossi^{50a}, M. Rotaru^{25a}, J. Rothberg¹³⁷, I. Rottländer²⁰, D. Rousseau¹¹⁴, C.R. Royon¹³⁵, A. Rozanov⁸³, Y. Rozen¹⁵⁰, X. Ruan³², B. Ruckert⁹⁸, N. Ruckstuhl¹⁰⁵, V.I. Rud⁹⁷, G. Rudolph⁶², F. Rühr^{58a}, F. Ruggieri^{133a}, A. Ruiz-Martinez¹⁶⁵, L. Rumyantsev⁶⁵, N.A. Rusakovich⁶⁵, J.P. Rutherford⁶, C. Ruwiedel²⁰, P. Ruzicka¹²⁴, Y.F. Ryabov¹²⁰, V. Ryadovikov¹²⁷, P. Ryan⁸⁸, G. Rybkin¹¹⁴, S. Rzaeva¹⁰, A.F. Saavedra¹⁴⁸, H.F.W. Sadrozinski¹³⁶, R. Sadykov⁶⁵, H. Sakamoto¹⁵³, G. Salamanna¹⁰⁵, A. Salamon^{132a}, M. Saleem¹¹⁰, D. Salihagic⁹⁹, A. Salnikov¹⁴², J. Salt¹⁶⁵, B.M. Salvachua Ferrando⁵, D. Salvatore^{36a,36b}, F. Salvatore¹⁴⁷, A. Salvucci⁴⁷, A. Salzburger⁴¹, D. Sampsonidis¹⁵², B.H. Samset¹¹⁶, M.A. Sanchis Lozano¹⁶⁵, H. Sandaker¹³, H.G. Sander⁸¹, M.P. Sanders⁹⁸, M. Sandhoff¹⁷², R. Sandstroem¹⁰⁵, S. Sandvoss¹⁷², D.P.C. Sankey¹²⁸, B. Sanny¹⁷², A. Sansoni⁴⁷, C. Santamarina Rios⁸⁵, L. Santi^{162a,162c}, C. Santoni³³, R. Santonico^{132a,132b}, D. Santos^{123b}, J. Santos^{123b}, J.G. Saraiva^{123b}, T. Sarangi¹⁷⁰, E. Sarkisyan-Grinbaum⁷, F. Sarri^{121a,121b}, O. Sasaki⁶⁶, T. Sasaki⁶⁶, N. Sasao⁶⁸, I. Satsounkevitch⁹⁰, G. Sauvage⁴, P. Savard^{156,b}, A.Y. Savine⁶, V. Savinov¹²², L. Sawyer^{24,i}, D.H. Saxon⁵³, L.P. Says³³, C. Sbarra^{19a,19b}, A. Sbrizzi^{19a,19b}, D.A. Scannicchio²⁹, J. Schaarschmidt⁴³, P. Schacht⁹⁹, U. Schäfer⁸¹, S. Schaezel^{158b}, A.C. Schaffer¹¹⁴, D. Schaile⁹⁸, R.D. Schamberger¹⁴⁶, A.G. Schamov¹⁰⁶, V.A. Schegelsky¹²⁰, D. Scheirich⁸⁷, M. Schernau¹⁶¹, M.I. Scherzer¹⁴, C. Schiavi^{50a,50b}, J. Schieck⁹⁹, M. Schioppa^{36a,36b}, S. Schlenker²⁹, J.L. Schlereth⁵, P. Schmid⁶², M.P. Schmidt^{173,*}, K. Schmieden²⁰, C. Schmitt⁸¹, M. Schmitz²⁰, M. Schott²⁹, D. Schouten¹⁴¹, J. Schovancova¹²⁴, M. Schram⁸⁵, A. Schreiner⁶³, C. Schroeder⁸¹, N. Schroer^{58c}, M. Schroers¹⁷², G. Schuler²⁹, J. Schultes¹⁷², H.-C. Schultz-Coulon^{58a}, J. Schumacher⁴³, M. Schumacher⁴⁸, B.A. Schumm¹³⁶, Ph. Schune¹³⁵, C. Schwanenberger⁸², A. Schwartzman¹⁴², Ph. Schwemling⁷⁸, R. Schwienhorst⁸⁸, R. Schwierz⁴³, J. Schwindling¹³⁵, W.G. Scott¹²⁸, J. Searcy¹¹³, E. Sedykh¹²⁰, E. Segura¹¹, S.C. Seidel¹⁰³, A. Seiden¹³⁶, F. Seifert⁴³, J.M. Seixas^{23a}, G. Sekhniadze^{102a}, D.M. Seliverstov¹²⁰, B. Sellden¹⁴⁴, M. Seman¹⁴³, N. Semprini-Cesari^{19a,19b}, C. Serfon⁹⁸, L. Serin¹¹⁴, R. Seuster⁹⁹, H. Severini¹¹⁰, M.E. Sevir⁸⁶, A. Sfyrta¹⁶³, M. Shamim¹¹³, L.Y. Shan³², J.T. Shank²¹, Q.T. Shao⁸⁶, M. Shapiro¹⁴, P.B. Shatalov⁹⁵, L. Shaver⁶, C. Shaw⁵³, K. Shaw¹³⁸, D. Sherman²⁹, P. Sherwood⁷⁷, A. Shibata¹⁰⁷, M. Shimojima¹⁰⁰, T. Shin⁵⁶, A. Shmeleva⁹⁴, M.J. Shochet³⁰, M.A. Shupe⁶, P. Sicho¹²⁴, A. Sidoti¹⁵, A. Siebel¹⁷², F. Siegert⁷⁷, J. Siegrist¹⁴, Dj. Sijacki^{12a}, O. Silbert¹⁶⁹, J. Silva^{123b}, Y. Silver¹⁵¹, D. Silverstein¹⁴², S.B. Silverstein¹⁴⁴, V. Simak¹²⁶, Lj. Simic^{12a}, S. Simion¹¹⁴, B. Simmons⁷⁷, M. Simonyan⁴, P. Sinervo¹⁵⁶, N.B. Sinev¹¹³, V. Sipica¹⁴⁰, G. Siragusa⁸¹, A.N. Sisakyan⁶⁵, S.Yu. Sivoklokov⁹⁷, J. Sjoelin¹⁴⁴, T.B. Sjrursen¹³, P. Skubic¹¹⁰, N. Skvorodnev²², M. Slater¹⁷, T. Slavicek¹²⁶, K. Sliwa¹⁵⁹, J. Sloper²⁹, T. Sluka¹²⁴, V. Smakhtin¹⁶⁹, S.Yu. Smirnov⁹⁶, Y. Smirnov²⁴, L.N. Smirnova⁹⁷, O. Smirnova⁷⁹, B.C. Smith⁵⁷, D. Smith¹⁴², K.M. Smith⁵³, M. Smizanska⁷¹, K. Smolek¹²⁶, A.A. Snesev⁹⁴, S.W. Snow⁸², J. Snow¹¹⁰, J. Snuverink¹⁰⁵, S. Snyder²⁴, M. Soares^{123b}, R. Sobie^{167,h}, J. Sodomka¹²⁶, A. Soffer¹⁵¹, C.A. Solans¹⁶⁵, M. Solar¹²⁶, E. Solfaroli Camillocci^{131a,131b}, A.A. Solodkov¹²⁷, O.V. Solovyanov¹²⁷, R. Soluk², J. Sondericker²⁴, V. Sopko¹²⁶, B. Sopko¹²⁶, M. Sosebee⁷, V.V. Sosnovtsev⁹⁶, L. Sospedra Suay¹⁶⁵, A. Soukharev¹⁰⁶, S. Spagnolo^{72a,72b}, F. Spanò³⁴, P. Speckmayer²⁹, E. Spencer¹³⁶, R. Spighi^{19a}, G. Spigo²⁹, F. Spila^{131a,131b}, R. Spiwoks²⁹, M. Spousta¹²⁵, T. Spreitzer¹⁴¹, B. Spurlock⁷, R.D. St. Denis⁵³, T. Stahl¹⁴⁰, R. Stamen^{58a}, S.N. Stancu¹⁶¹, E. Stanecka²⁹, R.W. Stanek⁵, C. Stancu^{133a}, S. Stapnes¹¹⁶, E.A. Starchenko¹²⁷, J. Stark⁵⁵, P. Staroba¹²⁴, P. Starovoitov⁹¹, J. Stastny¹²⁴, A. Staude⁹⁸, P. Stavina¹⁴³, G. Stavropoulos¹⁴, P. Steinbach⁴³, P. Steinberg²⁴, I. Stekl¹²⁶, B. Stelzer¹⁴¹, H.J. Stelzer⁴¹, O. Stelzer-Chilton^{157a}, H. Stenzel⁵², K. Stevenson⁷⁵, G. Stewart⁵³, M.C. Stockton¹⁷, K. Stoerig⁴⁸, G. Stoicea^{25a}, S. Stonjek⁹⁹, P. Strachota¹²⁵, A. Stradling⁷, A. Straessner⁴³, J. Strandberg⁸⁷, S. Strandberg¹⁴, A. Strandlie¹¹⁶, M. Strauss¹¹⁰, P. Strizenecek¹⁴³, R. Ströhmer⁹⁸, D.M. Strom¹¹³, J.A. Strong^{76,*}, R. Stroynowski³⁹, J. Strube¹²⁸, B. Stugu¹³, I. Stumer^{24,*}, D.A. Soh^{149,z}, D. Su¹⁴², S.I. Suchkov⁹⁶, Y. Sugaya¹¹⁵, T. Sugimoto¹⁰¹, C. Suhr⁵, M. Suk¹²⁵, V.V. Sulin⁹⁴, S. Sultansoy^{3,aa}, T. Sumida²⁹, X. Sun³², J.E. Sundermann⁴⁸, K. Suruliz^{162a,162b}, S. Sushkov¹¹, G. Susinno^{36a,36b}, M.R. Sutton¹³⁸, T. Suzuki¹⁵³, Y. Suzuki⁶⁶, Yu.M. Sviridov¹²⁷, I. Sykora¹⁴³, T. Sykora¹²⁵, T. Szymocha³⁸, J. Sánchez¹⁶⁵, D. Ta²⁰, K. Tackmann²⁹, A. Taffard¹⁶¹, R. Tafirout^{157a}, A. Taga¹¹⁶, Y. Takahashi¹⁰¹, H. Takai²⁴, R. Takashima⁶⁹, H. Takeda⁶⁷, T. Takeshita¹³⁹, M. Talby⁸³, A. Talyshv¹⁰⁶, M.C. Tamsett⁷⁶, J. Tanaka¹⁵³, R. Tanaka¹¹⁴, S. Tanaka¹³⁰, S. Tanaka⁶⁶, G.P. Tappern²⁹, S. Tapprogge⁸¹, D. Tardif¹⁵⁶, S. Tarem¹⁵⁰, F. Tarrade²⁴, G.F. Tartarelli^{89a}, P. Tas¹²⁵, M. Tasevsky¹²⁴, E. Tassi^{36a,36b}, C. Taylor⁷⁷, F.E. Taylor⁹², G.N. Taylor⁸⁶, R.P. Taylor¹⁶⁷, W. Taylor^{157b}, P. Teixeira-Dias⁷⁶, H. Ten Kate²⁹, P.K. Teng¹⁴⁹, S. Terada⁶⁶, K. Terashi¹⁵³, J. Terron⁸⁰, M. Terwort^{41,q}, M. Testa⁴⁷, R.J. Teuscher^{156,h}, C.M. Tevlin⁸², J. Thadome¹⁷², R. Thananuwig⁴⁹, M. Thioye¹⁷³, S. Thoma⁴⁸, J.P. Thomas¹⁷, T.L. Thomas¹⁰³, E.N. Thompson⁸⁴, P.D. Thompson¹⁷, P.D. Thompson¹⁵⁶, R.J. Thompson⁸², A.S. Thompson⁵³, E. Thomson¹¹⁹, R.P. Thun⁸⁷, T. Tic¹²⁴, V.O. Tikhomirov⁹⁴, Y.A. Tikhonov¹⁰⁶, C.J.W.P. Timmermans¹⁰⁴, P. Tipton¹⁷³, F.J. Tique Aires Viegas²⁹, S. Tisserant⁸³, J. Tobias⁴⁸, B. Toczek³⁷, T. Todorov⁴, S. Todorova-Nova¹⁵⁹, B. Toggerson¹⁶¹, J. Tojo⁶⁶, S. Tokár¹⁴³, K. Tokushuku⁶⁶, K. Tollefson⁸⁸, L. Tomasek¹²⁴, M. Tomasek¹²⁴, F. Tomasz¹⁴³, M. Tomoto¹⁰¹, D. Tompkins⁶,

L. Tompkins¹⁴, K. Toms¹⁰³, G. Tong³², A. Tonoyan¹³, C. Topfel¹⁶, N.D. Topilin⁶⁵, E. Torrence¹¹³, E. Torró Pastor¹⁶⁵, J. Toth^{83,x}, F. Touchard⁸³, D.R. Tovey¹³⁸, S.N. Tovey⁸⁶, T. Trefzger¹⁷¹, L. Tremblet²⁹, A. Tricoli²⁹, I.M. Trigger^{157a}, S. Trincas-Duvoid⁷⁸, T.N. Trinh⁷⁸, M.F. Tripania⁷⁰, N. Triplett⁶⁴, A. Trivedi^{24,w}, B. Trocme⁵⁵, C. Troncon^{89a}, A. Trzupek³⁸, C. Tsarouchas⁹, J.C.-L. Tseng¹¹⁷, I. Tsiakis¹⁵², M. Tsiakiris¹⁰⁵, P.V. Tsiarehsha⁹⁰, D. Tsiouni¹³⁸, G. Tsipolitis⁹, V. Tsiskaridze⁵¹, E.G. Tskhadadze⁵¹, I.I. Tsukerman⁹⁵, V. Tsulaia¹²², J.-W. Tsung²⁰, S. Tsuno⁶⁶, D. Tsybychev¹⁴⁶, M. Turala³⁸, D. Turecek¹²⁶, I. Turk Cakir^{3,ab}, E. Turlay¹¹⁴, P.M. Tuts³⁴, M.S. Twomey¹³⁷, M. Tylmad¹⁴⁴, M. Tyndel¹²⁸, G. Tzanakos⁸, K. Uchida¹¹⁵, I. Ueda¹⁵³, M. Uhlenbrock²⁰, M. Uhrmacher⁵⁴, F. Ukegawa¹⁵⁸, G. Unal²⁹, D.G. Underwood⁵, A. Undrus²⁴, G. Unel¹⁶¹, Y. Unno⁶⁶, D. Urbaniec³⁴, E. Urkovsky¹⁵¹, P. Urquijo⁴⁹, P. Urrejola^{31a}, G. Usai⁷, M. Uslenghi^{118a,118b}, L. Vacavant⁸³, V. Vacek¹²⁶, B. Vachon⁸⁵, S. Vahsen¹⁴, J. Valenta¹²⁴, P. Valente^{131a}, S. Valentini^{19a,19b}, S. Valkar¹²⁵, E. Valladolid Gallego¹⁶⁵, S. Vallecorsa¹⁵⁰, J.A. Valls Ferrer¹⁶⁵, R. Van Berg¹¹⁹, H. van der Graaf¹⁰⁵, E. van der Kraaij¹⁰⁵, E. van der Poel¹⁰⁵, D. Van Der Ster²⁹, N. van Eldik⁸⁴, P. van Gemmeren⁵, Z. van Kesteren¹⁰⁵, I. van Vulpen¹⁰⁵, W. Vandelli²⁹, G. Vandoni²⁹, A. Vaniachine⁵, P. Vankov⁷³, F. Vannucci⁷⁸, F. Varela Rodriguez²⁹, R. Vari^{131a}, E.W. Varnes⁶, D. Varouchas¹⁴, A. Vartapetian⁷, K.E. Varvell¹⁴⁸, L. Vasilyeva⁹⁴, V.I. Vassilakopoulos⁵⁶, F. Vazeille³³, G. Vegni^{89a,89b}, J.J. Veillet¹¹⁴, C. Vellidis⁸, F. Veloso^{123b}, R. Veness²⁹, S. Veneziano^{131a}, A. Ventura^{72a,72b}, D. Ventura¹³⁷, M. Venturi⁴⁸, N. Venturi¹⁶, V. Vercesi^{118a}, M. Verducci¹⁷¹, W. Verkerke¹⁰⁵, J.C. Vermeulen¹⁰⁵, M.C. Vetterli^{141,b}, I. Vichou¹⁶³, T. Vickey¹⁷⁰, G.H.A. Viehhauser¹¹⁷, M. Villa^{19a,19b}, E.G. Villani¹²⁸, M. Villaplana Perez¹⁶⁵, J. Villate^{123b}, E. Vilucchi⁴⁷, M.G. Vinciter²⁸, E. Vinek²⁹, V.B. Vinogradov⁶⁵, S. Viret³³, J. Virzi¹⁴, A. Vitale^{19a,19b}, O.V. Vitells¹⁶⁹, I. Vivarelli⁴⁸, F. Vives Vagues¹¹, S. Vlachos⁹, M. Vlasak¹²⁶, N. Vlasov²⁰, H. Vogt⁴¹, P. Vokac¹²⁶, M. Volpi¹¹, G. Volpini^{89a,89b}, H. von der Schmitt⁹⁹, J. von Loeben⁹⁹, H. von Radziewski⁴⁸, E. von Toerne²⁰, V. Vorobel¹²⁵, A.P. Vorobiev¹²⁷, V. Vorwerk¹¹, M. Vos¹⁶⁵, R. Voss²⁹, T.T. Voss¹⁷², J.H. Vossebeld⁷³, N. Vranjes^{12a}, M. Vranjes Milosavljevic^{12a}, V. Vrba¹²⁴, M. Vreeswijk¹⁰⁵, T. Vu Anh⁸¹, D. Vudragovic^{12a}, R. Vuillermet²⁹, I. Vukotic¹¹⁴, P. Wagner¹¹⁹, H. Wahlen¹⁷², J. Walbersloh⁴², J. Walder⁷¹, R. Walker⁹⁸, W. Walkowiak¹⁴⁰, R. Wall¹⁷³, C. Wang⁴⁴, H. Wang¹⁷⁰, J. Wang⁵⁵, J.C. Wang¹³⁷, S.M. Wang¹⁴⁹, C.P. Ward²⁷, M. Warsinsky⁴⁸, R. Wastie¹¹⁷, P.M. Watkins¹⁷, A.T. Watson¹⁷, M.F. Watson¹⁷, G. Watts¹³⁷, S. Watts⁸², A.T. Waugh¹⁴⁸, B.M. Waugh⁷⁷, M. Weber⁴⁸, J. Weber⁴², M.D. Weber¹⁶, M. Weber¹²⁸, M.S. Weber¹⁶, P. Weber^{58a}, A.R. Weidberg¹¹⁷, J. Weingarten⁵⁴, C. Weiser⁴⁸, H. Wellenstein²², P.S. Wells²⁹, M. Wen⁴⁷, T. Wenaus²⁴, S. Wendler¹²², T. Wengler⁸², S. Wenig²⁹, N. Wermes²⁰, M. Werner⁴⁸, P. Werner²⁹, M. Werth¹⁶¹, U. Werthenbach¹⁴⁰, M. Wessels^{58a}, K. Whalen²⁸, S.J. Wheeler-Ellis¹⁶¹, S.P. Whitaker²¹, A. White⁷, M.J. White²⁷, S. White²⁴, D. Whiteson¹⁶¹, D. Whittington⁶¹, F. Wicek¹¹⁴, D. Wicke⁸¹, F.J. Wickens¹²⁸, W. Wiedenmann¹⁷⁰, M. Wielers¹²⁸, P. Wienemann²⁰, C. Wiglesworth⁷³, L.A.M. Wiik⁴⁸, A. Wildauer¹⁶⁵, M.A. Wildt^{41,q}, I. Wilhelm¹²⁵, H.G. Wilkens²⁹, E. Williams³⁴, H.H. Williams¹¹⁹, W. Willis³⁴, S. Willocq⁸⁴, J.A. Wilson¹⁷, M.G. Wilson¹⁴², A. Wilson⁸⁷, I. Wingerter-Seez⁴, F. Winklmeier²⁹, M. Wittgen¹⁴², M.W. Wolter³⁸, H. Wolters^{123b}, B.K. Wosiek³⁸, J. Wotschack²⁹, M.J. Woudstra⁸⁴, K. Wraight⁵³, C. Wright⁵³, D. Wright¹⁴², B. Wrona⁷³, S.L. Wu¹⁷⁰, X. Wu⁴⁹, E. Wulf³⁴, S. Xella³⁵, S. Xie⁴⁸, Y. Xie³², D. Xu¹³⁸, N. Xu¹⁷⁰, M. Yamada¹⁵⁸, A. Yamamoto⁶⁶, S. Yamamoto¹⁵³, T. Yamamura¹⁵³, K. Yamanaka⁶⁴, J. Yamaoka⁴⁴, T. Yamazaki¹⁵³, Y. Yamazaki⁶⁷, Z. Yan²¹, H. Yang⁸⁷, U.K. Yang⁸², Y. Yang³², Z. Yang¹⁴⁴, W.-M. Yao¹⁴, Y. Yao¹⁴, Y. Yasu⁶⁶, J. Ye³⁹, S. Ye²⁴, M. Yilmaz^{3,ac}, R. Yoosoofmiya¹²², K. Yorita¹⁶⁸, R. Yoshida⁵, C. Young¹⁴², S.P. Youssef²¹, D. Yu²⁴, J. Yu⁷, M. Yu^{58c}, X. Yu³², J. Yuan⁹⁹, L. Yuan⁷⁸, A. Yurkewicz¹⁴⁶, R. Zaidan⁶³, A.M. Zaitsev¹²⁷, Z. Zajacova²⁹, V. Zambrano⁴⁷, L. Zanello^{131a,131b}, P. Zarzhitsky³⁹, A. Zaytsev¹⁰⁶, C. Zeitnitz¹⁷², M. Zeller¹⁷³, P.F. Zema²⁹, A. Zemla³⁸, C. Zendler²⁰, O. Zenin¹²⁷, T. Zenis¹⁴³, Z. Zenonos^{121a,121b}, S. Zenz¹⁴, D. Zerwas¹¹⁴, G. Zevi della Porta⁵⁷, Z. Zhan³², H. Zhang⁸³, J. Zhang⁵, Q. Zhang⁵, X. Zhang³², L. Zhao¹⁰⁷, T. Zhao¹³⁷, Z. Zhao³², A. Zhemchugov⁶⁵, S. Zheng³², J. Zhong^{149,ad}, B. Zhou⁸⁷, N. Zhou³⁴, Y. Zhou¹⁴⁹, C.G. Zhu³², H. Zhu⁴¹, Y. Zhu¹⁷⁰, X. Zhuang⁹⁸, V. Zhuravlov⁹⁹, B. Zilka¹⁴³, R. Zimmermann²⁰, S. Zimmermann²⁰, S. Zimmermann⁴⁸, M. Ziolkowski¹⁴⁰, R. Zitoun⁴, L. Živković³⁴, V.V. Zmouchko^{127,*}, G. Zobernig¹⁷⁰, A. Zoccoli^{19a,19b}, M. zur Nedden¹⁵, and V. Zutshi⁵

¹ University at Albany, 1400 Washington Ave, Albany, NY 12222, United States of America

² University of Alberta, Department of Physics, Centre for Particle Physics, Edmonton, AB T6G 2G7, Canada

³ Ankara University, Faculty of Sciences, Department of Physics, TR 061000 Tandogan, Ankara, Turkey

⁴ LAPP, Université de Savoie, CNRS/IN2P3, Annecy-le-Vieux, France

⁵ Argonne National Laboratory, High Energy Physics Division, 9700 S. Cass Avenue, Argonne IL 60439, United States of America

⁶ University of Arizona, Department of Physics, Tucson, AZ 85721, United States of America

⁷ The University of Texas at Arlington, Department of Physics, Box 19059, Arlington, TX 76019, United States of America

⁸ University of Athens, Nuclear & Particle Physics, Department of Physics, Panepistimiopouli, Zografou, GR 15771 Athens, Greece

⁹ National Technical University of Athens, Physics Department, 9-Iroon Polytechniou, GR 15780 Zografou, Greece

¹⁰ Institute of Physics, Azerbaijan Academy of Sciences, H. Javid Avenue 33, AZ 143 Baku, Azerbaijan

¹¹ Institut de Física d'Altes Energies, IFAE, Edifici Cn, Universitat Autònoma de Barcelona, ES - 08193 Bellaterra (Barcelona), Spain

¹² ^(a) University of Belgrade, Institute of Physics, P.O. Box 57, 11001 Belgrade; Vinca Institute of Nuclear Sciences ^(b), Mihajla Petrovica Alasa 12-14, 11001 Belgrade, Serbia

- ¹³ University of Bergen, Department for Physics and Technology, Allegaten 55, NO - 5007 Bergen, Norway
- ¹⁴ Lawrence Berkeley National Laboratory and University of California, Physics Division, MS50B-6227, 1 Cyclotron Road, Berkeley, CA 94720, United States of America
- ¹⁵ Humboldt University, Institute of Physics, Berlin, Newtonstr. 15, D-12489 Berlin, Germany
- ¹⁶ University of Bern
- ¹⁷ Albert Einstein Center for Fundamental Physics, Laboratory for High Energy Physics, Sidlerstrasse 5, CH - 3012 Bern, Switzerland
- University of Birmingham, School of Physics and Astronomy, Edgbaston, Birmingham B15 2TT, United Kingdom
- ¹⁸ Bogazici University, Faculty of Sciences, Department of Physics, TR - 80815 Bebek-Istanbul, Turkey
- ¹⁹ INFN Sezione di Bologna^(a); Università di Bologna, Dipartimento di Fisica^(b), viale C. Berti Pichat, 6/2, IT - 40127 Bologna, Italy
- ²⁰ University of Bonn, Physikalisches Institut, Nussallee 12, D - 53115 Bonn, Germany
- ²¹ Boston University, Department of Physics, 590 Commonwealth Avenue, Boston, MA 02215, United States of America
- ²² Brandeis University, Department of Physics, MS057, 415 South Street, Waltham, MA 02454, United States of America
- ²³ Universidade Federal do Rio De Janeiro, Instituto de Fisica^(a), Caixa Postal 68528, Ilha do Fundao, BR - 21945-970 Rio de Janeiro; ^(b)Universidade de Sao Paulo, Instituto de Fisica, R.do Matao Trav. R.187, Sao Paulo - SP, 05508 - 900, Brazil
- ²⁴ Brookhaven National Laboratory, Physics Department, Bldg. 510A, Upton, NY 11973, United States of America
- ²⁵ National Institute of Physics and Nuclear Engineering^(a), Bucharest-Magurele, Str. Atomistilor 407, P.O. Box MG-6, R-077125, Romania; ^(b)University Politehnica Bucharest, Rectorat - AN 001, 313 Splaiul Independentei, sector 6, 060042 Bucuresti; ^(c)West University in Timisoara, Bd. Vasile Parvan 4, Timisoara, Romania
- ²⁶ Universidad de Buenos Aires, FCEyN, Dto. Fisica, Pab I - C. Universitaria, 1428 Buenos Aires, Argentina
- ²⁷ University of Cambridge, Cavendish Laboratory, J J Thomson Avenue, Cambridge CB3 0HE, United Kingdom
- ²⁸ Carleton University, Department of Physics, 1125 Colonel By Drive, Ottawa ON K1S 5B6, Canada
- ²⁹ CERN, CH - 1211 Geneva 23, Switzerland
- ³⁰ University of Chicago, Enrico Fermi Institute, 5640 S. Ellis Avenue, Chicago, IL 60637, United States of America
- ³¹ Pontificia Universidad Católica de Chile, Facultad de Fisica, Departamento de Fisica^(a), Avda. Vicuna Mackenna 4860, San Joaquin, Santiago; Universidad Técnica Federico Santa María, Departamento de Física^(b), Avda. España 1680, Casilla 110-V, Valparaíso, Chile
- ³² Institute of HEP, Chinese Academy of Sciences, P.O. Box 918, CN-100049 Beijing; USTC, Department of Modern Physics, Hefei, CN-230026 Anhui; Nanjing University, Department of Physics, CN-210093 Nanjing; Shandong University, HEP Group, CN-250100 Shadong, China
- ³³ Laboratoire de Physique Corpusculaire, CNRS-IN2P3, Université Blaise Pascal, FR - 63177 Aubiere Cedex, France
- ³⁴ Columbia University, Nevis Laboratory, 136 So. Broadway, Irvington, NY 10533, United States of America
- ³⁵ University of Copenhagen, Niels Bohr Institute, Blegdamsvej 17, DK - 2100 Kobenhavn 0, Denmark
- ³⁶ INFN Gruppo Collegato di Cosenza^(a); Università della Calabria, Dipartimento di Fisica^(b), IT-87036 Arcavacata di Rende, Italy
- ³⁷ Faculty of Physics and Applied Computer Science of the AGH-University of Science and Technology, (FPACS, AGH-UST), al. Mickiewicza 30, PL-30059 Cracow, Poland
- ³⁸ The Henryk Niewodniczanski Institute of Nuclear Physics, Polish Academy of Sciences, ul. Radzikowskiego 152, PL - 31342 Krakow, Poland
- ³⁹ Southern Methodist University, Physics Department, 106 Fondren Science Building, Dallas, TX 75275-0175, United States of America
- ⁴⁰ University of Texas at Dallas, 800 West Campbell Road, Richardson, TX 75080-3021, United States of America
- ⁴¹ DESY, Notkestr. 85, D-22603 Hamburg, Germany and Platanenalle 6, D-15738 Zeuthen, Germany
- ⁴² TU Dortmund, Experimentelle Physik IV, DE - 44221 Dortmund, Germany
- ⁴³ Technical University Dresden, Institut fuer Kern- und Teilchenphysik, Zellescher Weg 19, D-01069 Dresden, Germany
- ⁴⁴ Duke University, Department of Physics, Durham, NC 27708, United States of America
- ⁴⁵ University of Edinburgh, School of Physics & Astronomy, James Clerk Maxwell Building, The Kings Buildings, Mayfield Road, Edinburgh EH9 3JZ, United Kingdom
- ⁴⁶ Fachhochschule Wiener Neustadt; Johannes Gutenbergstrasse 3 AT - 2700 Wiener Neustadt, Austria
- ⁴⁷ INFN Laboratori Nazionali di Frascati, via Enrico Fermi 40, IT-00044 Frascati, Italy
- ⁴⁸ Albert-Ludwigs-Universität, Fakultät für Mathematik und Physik, Hermann-Herder Str. 3, D - 79104 Freiburg i.Br., Germany
- ⁴⁹ Université de Genève, Section de Physique, 24 rue Ernest Ansermet, CH - 1211 Geneve 4, Switzerland
- ⁵⁰ INFN Sezione di Genova^(a); Università di Genova, Dipartimento di Fisica^(b), via Dodecaneso 33, IT - 16146 Genova, Italy
- ⁵¹ Institute of Physics of the Georgian Academy of Sciences, 6 Tamarashvili St., GE - 380077 Tbilisi; Tbilisi State University, HEP Institute, University St. 9, GE - 380086 Tbilisi, Georgia
- ⁵² Justus-Liebig-Universität Giessen, II Physikalisches Institut, Heinrich-Buff Ring 16, D-35392 Giessen, Germany
- ⁵³ University of Glasgow, Department of Physics and Astronomy, Glasgow G12 8QQ, United Kingdom
- ⁵⁴ Georg-August-Universität, II. Physikalisches Institut, Friedrich-Hund Platz 1, D-37077 Goettingen, Germany
- ⁵⁵ Laboratoire de Physique Subatomique et de Cosmologie, CNRS/IN2P3, Université Joseph Fourier, INPG, 53 avenue des Martyrs, FR - 38026 Grenoble Cedex, France

- 56 Hampton University, Department of Physics, Hampton, VA 23668, United States of America
- 57 Harvard University, Laboratory for Particle Physics and Cosmology, 18 Hammond Street, Cambridge, MA 02138, United States of America
- 58 Ruprecht-Karls-Universität Heidelberg, Kirchhoff-Institut fuer Physik^(a), Im Neuenheimer Feld 227, DE - 69120 Heidelberg; ^(b)Physikalisches Institut, Philosophenweg 12, D-69120 Heidelberg; ZITI Ruprecht-Karls-Universität Heidelberg^(c), Lehrstuhl fuer Informatik V, B6, 23-29, DE - 68131 Mannheim, Germany
- 59 Hiroshima University, Faculty of Science, 1-3-1 Kagamiyama, Higashihiroshima-shi, JP - Hiroshima 739-8526, Japan
- 60 Hiroshima Institute of Technology, Faculty of Applied Information Science, 2-1-1 Miyake Saeki-ku, Hiroshima-shi, JP - Hiroshima 731-5193, Japan
- 61 Indiana University, Department of Physics, Swain Hall West 117, Bloomington, IN 47405-7105, United States of America
- 62 Institut fuer Astro- und Teilchenphysik, Technikerstrasse 25, A - 6020 Innsbruck, Austria
- 63 University of Iowa, 203 Van Allen Hall, Iowa City, IA 52242-1479, United States of America
- 64 Iowa State University, Department of Physics and Astronomy, Ames High Energy Physics Group, Ames, IA 50011-3160, United States of America
- 65 Joint Institute for Nuclear Research, JINR Dubna, RU - 141 980 Moscow Region, Russia
- 66 KEK, High Energy Accelerator Research Organization, 1-1 Oho, Tsukuba-shi, Ibaraki-ken 305-0801, Japan
- 67 Kobe University, Graduate School of Science, 1-1 Rokkodai-cho, Nada-ku, JP Kobe 657-8501, Japan
- 68 Kyoto University, Faculty of Science, Oiwake-cho, Kitashirakawa, Sakyou-ku, Kyoto-shi, JP - Kyoto 606-8502, Japan
- 69 Kyoto University of Education, 1 Fukakusa, Fujimori, Fushimi-ku, Kyoto-shi, JP - Kyoto 612-8522, Japan
- 70 Universidad Nacional de La Plata, FCE, Departamento de Física, IFLP (CONICET-UNLP), C.C. 67, 1900 La Plata, Argentina
- 71 Lancaster University, Physics Department, Lancaster LA1 4YB, United Kingdom
- 72 INFN Sezione di Lecce^(a); Università del Salento, Dipartimento di Fisica^(b) Via Arnesano IT - 73100 Lecce, Italy
- 73 University of Liverpool, Oliver Lodge Laboratory, P.O. Box 147, Oxford Street, Liverpool L69 3BX, United Kingdom
- 74 Jožef Stefan Institute and University of Ljubljana, Department of Physics, SI-1000 Ljubljana, Slovenia
- 75 Queen Mary University of London, Department of Physics, Mile End Road, London E1 4NS, United Kingdom
- 76 Royal Holloway, University of London, Department of Physics, Egham Hill, Egham, Surrey TW20 0EX, United Kingdom
- 77 University College London, Department of Physics and Astronomy, Gower Street, London WC1E 6BT, United Kingdom
- 78 Laboratoire de Physique Nucléaire et de Hautes Energies, Université Pierre et Marie Curie (Paris 6), Université Denis Diderot (Paris-7), CNRS/IN2P3, Tour 33, 4 place Jussieu, FR - 75252 Paris Cedex 05, France
- 79 Lunds universitet, Naturvetenskapliga fakulteten, Fysiska institutionen, Box 118, SE - 221 00 Lund, Sweden
- 80 Universidad Autonoma de Madrid, Facultad de Ciencias, Departamento de Física Teórica, ES - 28049 Madrid, Spain
- 81 Universität Mainz, Institut fuer Physik, Staudinger Weg 7, DE - 55099 Mainz, Germany
- 82 University of Manchester, School of Physics and Astronomy, Manchester M13 9PL, United Kingdom
- 83 CPPM, Aix-Marseille Université, CNRS/IN2P3, Marseille, France
- 84 University of Massachusetts, Department of Physics, 710 North Pleasant Street, Amherst, MA 01003, United States of America
- 85 McGill University, High Energy Physics Group, 3600 University Street, Montreal, Quebec H3A 2T8, Canada
- 86 University of Melbourne, School of Physics, AU - Parkville, Victoria 3010, Australia
- 87 The University of Michigan, Department of Physics, 2477 Randall Laboratory, 500 East University, Ann Arbor, MI 48109-1120, United States of America
- 88 Michigan State University, Department of Physics and Astronomy, High Energy Physics Group, East Lansing, MI 48824-2320, United States of America
- 89 INFN Sezione di Milano^(a); Università di Milano, Dipartimento di Fisica^(b), via Celoria 16, IT - 20133 Milano, Italy
- 90 B.I. Stepanov Institute of Physics, National Academy of Sciences of Belarus, Independence Avenue 68, Minsk 220072, Republic of Belarus
- 91 National Scientific & Educational Centre for Particle & High Energy Physics, NC PHEP BSU, M. Bogdanovich St. 153, Minsk 220040, Republic of Belarus
- 92 Massachusetts Institute of Technology, Department of Physics, Room 24-516, Cambridge, MA 02139, United States of America
- 93 University of Montreal, Group of Particle Physics, C.P. 6128, Succursale Centre-Ville, Montreal, Quebec, H3C 3J7, Canada
- 94 P.N. Lebedev Institute of Physics, Academy of Sciences, Leninsky pr. 53, RU - 117 924 Moscow, Russia
- 95 Institute for Theoretical and Experimental Physics (ITEP), B. Cheremushkinskaya ul. 25, RU 117 218 Moscow, Russia
- 96 Moscow Engineering & Physics Institute (MEPhI), Kashirskoe Shosse 31, RU - 115409 Moscow, Russia
- 97 Lomonosov Moscow State University Skobeltsyn Institute of Nuclear Physics (MSU SINP), 1(2), Leninskie gory, GSP-1, Moscow 119991 Russian Federation, Russia
- 98 Ludwig-Maximilians-Universität München, Fakultät für Physik, Am Coulombwall 1, DE - 85748 Garching, Germany
- 99 Max-Planck-Institut für Physik, (Werner-Heisenberg-Institut), Föhringer Ring 6, 80805 München, Germany
- 100 Nagasaki Institute of Applied Science, 536 Aba-machi, JP Nagasaki 851-0193, Japan
- 101 Nagoya University, Graduate School of Science, Furo-Cho, Chikusa-ku, Nagoya, 464-8602, Japan
- 102 INFN Sezione di Napoli^(a); Università di Napoli, Dipartimento di Scienze Fisiche^(b), Complesso Universitario di Monte Sant'Angelo, via Cinthia, IT - 80126 Napoli, Italy

- University of New Mexico, Department of Physics and Astronomy, MSC07 4220, Albuquerque, NM 87131 USA, United States of America
- Radboud University Nijmegen/NIKHEF, Department of Experimental High Energy Physics, Toernooiveld 1, NL - 6525 ED Nijmegen, Netherlands
- Nikhef National Institute for Subatomic Physics, and University of Amsterdam, Science Park 105, 1098 XG Amsterdam, Netherlands
- Budker Institute of Nuclear Physics (BINP), RU - Novosibirsk 630 090, Russia
- New York University, Department of Physics, 4 Washington Place, New York NY 10003, USA, United States of America
- Ohio State University, 191 West Woodruff Ave, Columbus, OH 43210-1117, United States of America
- Okayama University, Faculty of Science, Tsushimanaka 3-1-1, Okayama 700-8530, Japan
- University of Oklahoma, Homer L. Dodge Department of Physics and Astronomy, 440 West Brooks, Room 100, Norman, OK 73019-0225, United States of America
- Oklahoma State University, Department of Physics, 145 Physical Sciences Building, Stillwater, OK 74078-3072, United States of America
- Palacký University, 17.listopadu 50a, 772 07 Olomouc, Czech Republic
- University of Oregon, Center for High Energy Physics, Eugene, OR 97403-1274, United States of America
- LAL, Univ. Paris-Sud, IN2P3/CNRS, Orsay, France
- Osaka University, Graduate School of Science, Machikaneyama-machi 1-1, Toyonaka, Osaka 560-0043, Japan
- University of Oslo, Department of Physics, P.O. Box 1048, Blindern, NO - 0316 Oslo 3, Norway
- Oxford University, Department of Physics, Denys Wilkinson Building, Keble Road, Oxford OX1 3RH, United Kingdom
- INFN Sezione di Pavia^(a); Università di Pavia, Dipartimento di Fisica Nucleare e Teorica^(b), Via Bassi 6, IT-27100 Pavia, Italy
- University of Pennsylvania, Department of Physics, High Energy Physics Group, 209 S. 33rd Street, Philadelphia, PA 19104, United States of America
- Petersburg Nuclear Physics Institute, RU - 188 300 Gatchina, Russia
- INFN Sezione di Pisa^(a); Università di Pisa, Dipartimento di Fisica E. Fermi^(b), Largo B. Pontecorvo 3, IT - 56127 Pisa, Italy
- University of Pittsburgh, Department of Physics and Astronomy, 3941 O'Hara Street, Pittsburgh, PA 15260, United States of America
- ^(a)Universidad de Granada, Departamento de Fisica Teorica y del Cosmos and CAFPE, E-18071 Granada; Laboratorio de Instrumentacao e Fisica Experimental de Particulas - LIP^(b), Avenida Elias Garcia 14-1, PT - 1000-149 Lisboa, Portugal
- Institute of Physics, Academy of Sciences of the Czech Republic, Na Slovance 2, CZ - 18221 Praha 8, Czech Republic
- Charles University in Prague, Faculty of Mathematics and Physics, Institute of Particle and Nuclear Physics, V Holesovickach 2, CZ - 18000 Praha 8, Czech Republic
- Czech Technical University in Prague, Zikova 4, CZ - 166 35 Praha 6, Czech Republic
- State Research Center Institute for High Energy Physics, Moscow Region, 142281, Protvino, Pobeda street, 1, Russia
- Rutherford Appleton Laboratory, Science and Technology Facilities Council, Harwell Science and Innovation Campus, Didcot OX11 0QX, United Kingdom
- University of Regina, Physics Department, Canada
- Ritsumeikan University, Noji Higashi 1 chome 1-1, JP - Kusatsu, Shiga 525-8577, Japan
- INFN Sezione di Roma I^(a); Università La Sapienza, Dipartimento di Fisica^(b), Piazzale A. Moro 2, IT- 00185 Roma, Italy
- INFN Sezione di Roma Tor Vergata^(a); Università di Roma Tor Vergata, Dipartimento di Fisica^(b), via della Ricerca Scientifica, IT-00133 Roma, Italy
- INFN Sezione di Roma Tre^(a); Università Roma Tre, Dipartimento di Fisica^(b), via della Vasca Navale 84, IT-00146 Roma, Italy
- Université Hassan II, Faculté des Sciences Ain Chock^(a), B.P. 5366, MA - Casablanca; Centre National de l'Energie des Sciences Techniques Nucleaires (CNESTEN)^(b), B.P. 1382 R.P. 10001 Rabat 10001; Université Mohamed Premier^(c), LPTPM, Faculté des Sciences, B.P.717. Bd. Mohamed VI, 60000, Oujda ; Université Mohammed V, Faculté des Sciences^(d), LPNR, BP 1014, 10000 Rabat, Morocco
- CEA, DSM/IRFU, Centre d'Etudes de Saclay, FR - 91191 Gif-sur-Yvette, France
- University of California Santa Cruz, Santa Cruz Institute for Particle Physics (SCIPP), Santa Cruz, CA 95064, United States of America
- University of Washington, Seattle, Department of Physics, Box 351560, Seattle, WA 98195-1560, United States of America
- University of Sheffield, Department of Physics & Astronomy, Hounsfield Road, Sheffield S3 7RH, United Kingdom
- Shinshu University, Department of Physics, Faculty of Science, 3-1-1 Asahi, Matsumoto-shi, JP - Nagano 390-8621, Japan
- Universitaet Siegen, Fachbereich Physik, D 57068 Siegen, Germany
- Simon Fraser University, Department of Physics, 8888 University Drive, CA - Burnaby, BC V5A 1S6, Canada
- SLAC National Accelerator Laboratory, Stanford, California 94309, United States of America
- Comenius University, Faculty of Mathematics, Physics & Informatics, Mlynska dolina F2, SK - 84248 Bratislava; Institute of Experimental Physics of the Slovak Academy of Sciences, Dept. of Subnuclear Physics, Watsonova 47, SK - 04353 Kosice, Slovak Republic
- Stockholm University, Department of Physics, AlbaNova, SE - 106 91 Stockholm, Sweden

- 145 Royal Institute of Technology (KTH), Physics Department, SE - 106 91 Stockholm, Sweden
- 146 Stony Brook University, Department of Physics and Astronomy, Nicolls Road, Stony Brook, NY 11794-3800, United States of America
- 147 University of Sussex, Department of Physics and Astronom
- 148 Pevensey 2 Building, Falmer, Brighton BN1 9QH, United Kingdom
- University of Sydney, School of Physics, AU - Sydney NSW 2006, Australia
- 149 Insitute of Physics, Academia Sinica, TW - Taipei 11529, Taiwan
- 150 Technion, Israel Inst. of Technology, Department of Physics, Technion City, IL - Haifa 32000, Israel
- 151 Tel Aviv University, Raymond and Beverly Sackler School of Physics and Astronomy, Ramat Aviv, IL - Tel Aviv 69978, Israel
- 152 Aristotle University of Thessaloniki, Faculty of Science, Department of Physics, Division of Nuclear & Particle Physics, University Campus, GR - 54124, Thessaloniki, Greece
- 153 The University of Tokyo, International Center for Elementary Particle Physics and Department of Physics, 7-3-1 Hongo, Bunkyo-ku, JP - Tokyo 113-0033, Japan
- 154 Tokyo Metropolitan University, Graduate School of Science and Technology, 1-1 Minami-Osawa, Hachioji, Tokyo 192-0397, Japan
- 155 Tokyo Institute of Technology, 2-12-1-H-34 O-Okayama, Meguro, Tokyo 152-8551, Japan
- 156 University of Toronto, Department of Physics, 60 Saint George Street, Toronto M5S 1A7, Ontario, Canada
- 157 TRIUMF^(a), 4004 Wesbrook Mall, Vancouver, B.C. V6T 2A3; ^(b)York University, Department of Physics and Astronomy, 4700 Keele St., Toronto, Ontario, M3J 1P3, Canada
- 158 University of Tsukuba, Institute of Pure and Applied Sciences, 1-1-1 Tennoudai, Tsukuba-shi, JP - Ibaraki 305-8571, Japan
- 159 Tufts University, Science & Technology Center, 4 Colby Street, Medford, MA 02155, United States of America
- 160 Universidad Antonio Narino, Centro de Investigaciones, Cra 3 Este No.47A-15, Bogota, Colombia
- 161 University of California, Irvine, Department of Physics & Astronomy, CA 92697-4575, United States of America
- 162 INFN Gruppo Collegato di Udine^(a); ICTP^(b), Strada Costiera 11, IT-34014, Trieste; Università di Udine, Dipartimento di Fisica^(c), via delle Scienze 208, IT - 33100 Udine, Italy
- 163 University of Illinois, Department of Physics, 1110 West Green Street, Urbana, Illinois 61801, United States of America
- 164 University of Uppsala, Department of Physics and Astronomy, P.O. Box 516, SE -751 20 Uppsala, Sweden
- 165 Instituto de Física Corpuscular (IFIC) Centro Mixto UVEG-CSIC, Apdo. 22085 ES-46071 Valencia, Dept. Física At. Mol. y Nuclear; Univ. of Valencia, and Instituto de Microelectrónica de Barcelona (IMB-CNM-CSIC) 08193 Bellaterra Barcelona, Spain
- 166 University of British Columbia, Department of Physics, 6224 Agricultural Road, CA - Vancouver, B.C. V6T 1Z1, Canada
- 167 University of Victoria, Department of Physics and Astronomy, P.O. Box 3055, Victoria B.C., V8W 3P6, Canada
- 168 Waseda University, WISE, 3-4-1 Okubo, Shinjuku-ku, Tokyo, 169-8555, Japan
- 169 The Weizmann Institute of Science, Department of Particle Physics, P.O. Box 26, IL - 76100 Rehovot, Israel
- 170 University of Wisconsin, Department of Physics, 1150 University Avenue, WI 53706 Madison, Wisconsin, United States of America
- 171 Julius-Maximilians-University of Würzburg, Physikalisches Institute, Am Hubland, 97074 Wuerzburg, Germany
- 172 Bergische Universitaet, Fachbereich C, Physik, Postfach 100127, Gauss-Strasse 20, D- 42097 Wuppertal, Germany
- 173 Yale University, Department of Physics, PO Box 208121, New Haven CT, 06520-8121, United States of America
- 174 Yerevan Physics Institute, Alikhanian Brothers Street 2, AM - 375036 Yerevan, Armenia
- 175 ATLAS-Canada Tier-1 Data Centre 4004 Wesbrook Mall, Vancouver, BC, V6T 2A3, Canada
- 176 GridKA Tier-1 FZK, Forschungszentrum Karlsruhe GmbH, Steinbuch Centre for Computing (SCC), Hermann-von-Helmholtz-Platz 1, 76344 Eggenstein-Leopoldshafen, Germany
- 177 Port d'Informacio Cientifica (PIC), Universitat Autònoma de Barcelona (UAB), Edifici D, E-08193 Bellaterra, Spain
- 178 Centre de Calcul CNRS/IN2P3, Domaine scientifique de la Doua, 27 bd du 11 Novembre 1918, 69622 Villeurbanne Cedex, France
- 179 INFN-CNAF, Viale Berti Pichat 6/2, 40127 Bologna, Italy
- 180 Nordic Data Grid Facility, NORDUnet A/S, Kastruplundgade 22, 1, DK-2770 Kastrup, Denmark
- 181 SARA Reken- en Netwerkdiensten, Science Park 121, 1098 XG Amsterdam, Netherlands
- 182 Academia Sinica Grid Computing, Institute of Physics, Academia Sinica, No.128, Sec. 2, Academia Rd., Nankang, Taipei, Taiwan 11529, Taiwan
- 183 UK-T1-RAL Tier-1, Rutherford Appleton Laboratory, Science and Technology Facilities Council, Harwell Science and Innovation Campus, Didcot OX11 0QX, United Kingdom
- 184 RHIC and ATLAS Computing Facility, Physics Department, Building 510, Brookhaven National Laboratory, Upton, New York 11973, United States of America
- ^a Also at CPPM, Marseille.
- ^b Also at TRIUMF, 4004 Wesbrook Mall, Vancouver, B.C. V6T 2A3, Canada
- ^c Also at Gaziantep University, Turkey
- ^d Also at Faculty of Physics and Applied Computer Science of the AGH-University of Science and Technology, (FPACS, AGH-UST), al. Mickiewicza 30, PL-30059 Cracow, Poland

- ^e Also at Institute for Particle Phenomenology, Ogden Centre for Fundamental Physics, Department of Physics, University of Durham, Science Laboratories, South Rd, Durham DH1 3LE, United Kingdom
- ^f Currently at Dogus University, Kadik
- ^g Also at Università di Napoli Parthenope, via A. Acton 38, IT - 80133 Napoli, Italy
- ^h Also at Institute of Particle Physics (IPP), Canada
- ⁱ Louisiana Tech University, 305 Wisteria Street, P.O. Box 3178, Ruston, LA 71272, United States of America
- ^j Currently at Dumlupinar University, Kutahya, Turkey
- ^k Currently at Department of Physics, University of Helsinki, P.O. Box 64, FI-00014, Finland
- ^l At Department of Physics, California State University, Fresno, 2345 E. San Ramon Avenue, Fresno, CA 93740-8031, United States of America
- ^m Also at TRIUMF, 4004 Wesbrook Mall, Vancouver, B.C. V6T 2A3, Canada
- ⁿ Currently at Istituto Universitario di Studi Superiori IUSS, V.le Lungo Ticino Sforza 56, 27100 Pavia, Italy
- ^o Also at California Institute of Technology, Physics Department, Pasadena, CA 91125, United States of America
- ^p Also at University of Montreal
- ^q Also at Institut für Experimentalphysik, Universität Hamburg, Luruper Chaussee 149, 22761 Hamburg, Germany
- ^r Also at Petersburg Nuclear Physics Institute, RU - 188 300 Gatchina, Russia
- ^s Also at school of physics and engineering, Sun Yat-sen University
- ^t Also at school of physics, Shandong university, Jinan
- ^u Also at Rutherford Appleton Laboratory, Science and Technology Facilities Council, Harwell Science and Innovation Campus, Didcot OX11 0QX
- ^v Also at Rutherford Appleton Laboratory, Science and Technology Facilities Council, Harwell Science and Innovation Campus, Didcot OX11 0QX, United Kingdom
- ^w University of South Carolina, Dept. of Physics and Astronomy, 700 S. Main St, Columbia, SC 29208, United States of America
- ^x Also at KFKI Research Institute for Particle and Nuclear Physics, Budapest, Hungary
- ^y Also at Institute of Physics, Jagiellonian University, Cracow, Poland
- ^z also at school of physics and engineering, Sun Yat-sen University
- ^{aa} Currently at TOBB University, Ankara, Turkey
- ^{ab} Currently at TAEA, Ankara, Turkey
- ^{ac} Currently at Gazi University, Ankara, Turkey
- ^{ad} Also at Dept of Physics, Nanjing University
- ^{*} Deceased

Received: date / Revised version: date

Abstract. The ATLAS liquid argon calorimeter has been operating continuously since August 2006. At this time, only part of the calorimeter was readout, but since the beginning of 2008, all calorimeter cells have been connected to the ATLAS readout system in preparation for LHC collisions. This paper gives an overview of the liquid argon calorimeter performance measured in situ with random triggers, calibration data, cosmic muons, and LHC beam splash events. Results on the detector operation, timing performance, electronics noise, and gain stability are presented. High energy deposits from radiative cosmic muons and beam splash events allow to check the intrinsic constant term of the energy resolution. The uniformity of the electromagnetic barrel calorimeter response along η (averaged over ϕ) is measured at the percent level using minimum ionizing cosmic muons. Finally, studies of electromagnetic showers from radiative muons have been used to cross-check the Monte Carlo simulation. The performance results obtained using the ATLAS readout, data acquisition, and reconstruction software indicate that the liquid argon calorimeter is well-prepared for collisions at the dawn of the LHC era.

1 Introduction

Installation of the liquid argon (LAr) calorimeter in the ATLAS [1] experimental hall was completed in early 2008. Until recently, the expected performance of the LAr calorimeter was extrapolated from intensive testing of a few modules with electron and pion beams from 1998 to 2003 (Ref. [2, 3, 4, 5, 6, 7, 8, 9, 10]), and in 2004 of a complete ATLAS detector slice [11, 12, 13]. The 20 months separating the completion of the installation from the first LHC collisions have been used to commission the LAr calorimeter. This paper reviews the first in situ measurements of the electronics stability, the quality of the energy re-

construction, the calorimeter response uniformity and the agreement between data and the Monte Carlo simulation of electromagnetic shower shapes. The measurements are performed using calibration triggers, cosmic muons, and the first LHC beam events collected during this 20 months period. The results and the experience gained in the operation of the LAr calorimeter provide the foundation for a more rapid understanding of the experimental signatures of the first LHC collisions, involving electrons, photons, missing transverse energy (E_T^{miss}), jets, and τ s where the LAr calorimeter plays a central role.

This paper is organized as follows. Section 2 gives the present hardware status of the LAr calorimeter. Section 3 details the level of understanding of the ingredients entering the cell energy reconstruction: pedestals, noise, electronic gains, timing, and the quality of the signal pulse shape predictions. The current understanding of the first level trigger energy computation is also discussed. Section 4 describes the in situ performance of the electromagnetic LAr calorimeter using ionizing and radiating cosmic muons. Lastly, Section 5 draws the conclusions.

2 LAr calorimeter hardware status and data taking conditions

The LAr calorimeter is composed of electromagnetic and hadronic sub-detectors of which the main characteristics are described in Section 2.1. During the detector and electronics construction and installation, regular and stringent quality tests were performed, resulting in a fully functional LAr calorimeter. The operational stability of the cryostats since March 2008 is discussed in Section 2.2. The current status of the high voltage and the cell readout are discussed in Sections 2.3 and 2.4 respectively. Finally, the general data taking conditions are given in Section 2.5. In ATLAS, the positive x -axis is defined as pointing from the interaction point to the center of the LHC ring, the positive y -axis is defined as pointing upwards, and the positive z -axis corresponds to protons running anti-clockwise. The polar angle θ is measured from the beam axis (z -axis), the azimuthal angle ϕ is measured in the transverse (xy)-plane, and the pseudorapidity is defined as $\eta = -\ln \tan(\theta/2)$.

2.1 Main characteristics of the LAr calorimeter

The LAr calorimeter [1], shown in Figure 1, is composed of sampling detectors with full azimuthal symmetry, housed in one barrel and two endcap cryostats. More specifically, a highly granular electromagnetic (EM) calorimeter with accordion-shaped electrodes and lead absorbers in liquid argon covers the pseudorapidity range $|\eta| < 3.2$, and contains a barrel part (EMB [14], $|\eta| < 1.475$) and an endcap part (EMEC [15], $1.375 < |\eta| < 3.2$). For $|\eta| < 1.8$, a pre-sampler (PS [16,15]), consisting of an active LAr layer and installed directly in front of the EM calorimeters, provides a measurement of the energy lost upstream. Located behind the EMEC is a copper-liquid argon hadronic endcap calorimeter (HEC [17], $1.5 < |\eta| < 3.2$), and a copper/tungsten-liquid argon forward calorimeter (FCal [18]) covers the region closest to the beam at $3.1 < |\eta| < 4.9$. An hadronic Tile calorimeter ($|\eta| < 1.7$) surrounding the LAr cryostats completes the ATLAS calorimetry.

All the LAr detectors are segmented transversally and divided in three or four layers in depth, and correspond to a total of 182,468 readout cells, i.e. 97.2% of the full ATLAS calorimeter readout.

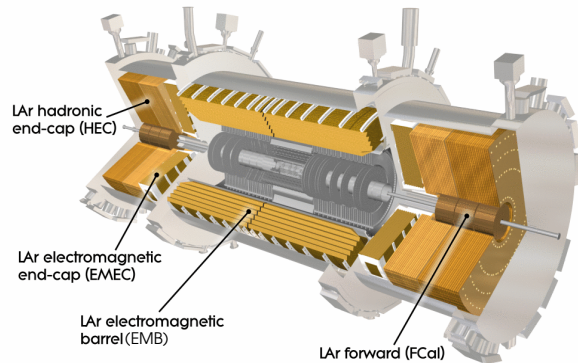


Fig. 1. Cut-away view of the LAr calorimeter, 17 m long (barrel + endcaps) and 4 m of diameter.

The relative energy resolution of the LAr calorimeter is usually parameterized by:

$$\frac{\sigma_E}{E} = \frac{a}{\sqrt{E}} \oplus \frac{b}{E} \oplus c, \quad (1)$$

where (a) is the stochastic term, (b) the noise term and (c) the constant term. The target values for these terms are respectively $a \simeq 10\%$, $b \simeq 170$ MeV (without pile-up) and $c = 0.7\%$.

2.2 Cryostat operation

Variations of the liquid argon temperature have a direct impact on the readout signal, and consequently on the energy scale, partly through the effect on the argon density, but mostly through the effect on the ionization electron drift velocity in the LAr. Overall, a $-2\%/K$ signal variation is expected [19]. The need to keep the corresponding contribution to the constant term of the energy resolution (Eq. 1) negligible (i.e. well below 0.2%) imposes a temperature uniformity requirement of better than 100 mK in each cryostat. In the liquid, ~ 500 temperature probes (PT100 platinum resistors) are fixed on the LAr detector components and read out every minute. In 2008-2009, installation activities in the ATLAS cavern prevented a stable cryostat temperature. A quiet period of ten days around the 2008 Christmas break, representative of what is expected during LHC collisions, allowed a check of the temperature stability in the absence of these external factors. The average dispersion (RMS) of the measurements of each temperature probe over this period is 1.6 mK (5 mK maximum), showing that no significant local temperature variation in time is observed in the three cryostats. Over this period, the temperature uniformity (RMS of all probes per cryostat) is illustrated for the barrel in Figure 2 and gives 59 mK. Results for the two endcap cryostats are also in the range 50-70 mK, below the required level of 100 mK. The average cryostat temperatures are slightly

different for the barrel (88.49 K) and the two endcaps (88.67 and 88.45 K) because they are independently regulated. An energy scale correction per cryostat will therefore be applied.

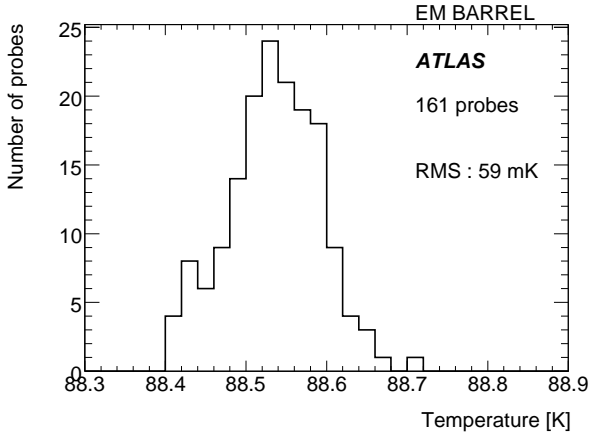


Fig. 2. Distribution of barrel cryostat probe temperatures averaged over a period of ten days.

To measure the effects of possible out-gassing of calorimeter materials under irradiation, which has been minimized by careful screening of components, 30 purity monitors measuring the energy deposition of radioactive sources in the LAr are installed in each cryostat and read every 15 minutes. The contribution to the constant term of the energy resolution is negligible for a level of electronegative impurities below 1000 ppb O_2 equivalent. All argon purity measurements over a period of two years are stable, in the range 200 ± 100 ppb O_2 equivalent, well below this requirement.

In summary, measurements of the liquid argon temperature and purity demonstrate that the stability of the operation of the three LAr cryostats is in the absence of proton beams within the required limits ensuring a negligible contribution to the energy resolution constant term.

2.3 High voltage status

The electron/ion drift speed in the LAr gap depends on the electric field, typically 1 kV/mm. Sub-detector-specific high voltage (HV) settings are applied. In the EM barrel, the high voltage is constant along η , while in the EMEC, where the gap varies continuously with radius, it is adjusted in steps along η . The HV supply granularity is typically in sectors of $\Delta\eta \times \Delta\phi = 0.2 \times 0.2$. For redundancy, each side of an EM electrode, which is in the middle of the LAr gap, is powered separately. In the HEC, each sub-gap is serviced by one of four different HV lines, while for the FCal each of the four electrode groups forming a normal readout channel is served by an independent HV line.

For HV sectors with non-optimal behavior, solutions were implemented in order to recover the corresponding

region. For example, in the EM calorimeter, faulty electrodes were connected to separate HV lines during the assembly phase at room temperature while, if the defect was identified during cryostat cold testing, the high voltage sector was divided into two in ϕ , each connected separately. The effect of zero voltage on one side of an electrode was studied in beam tests proving that with offline corrections the energy can still be measured, with only a small loss in accuracy. Finally, for HV sectors with a permanent short-circuit, high voltage modules permitting large DC current draws of up to 3 mA (more than three orders of magnitude above the nominal limit) are used in order to operate the faulty sector at 1000 V or above.

As a result, 93.9% of readout cells are operating under nominal conditions and the rest sees a reduced high voltage. However, even with a reduced high voltage, signals can be well reconstructed by using a correction scale factor. Figure 3 shows the distribution of all HV correction factors for the EM, HEC and FCal cells as of the end of September 2009. Since the beginning of 2008, no changes have been observed. The largest correction occurs if one side of an EM electrode is not powered, and only half of the signal is collected. For the faulty cells, this correction factor is applied online at the energy reconstruction level. A similar correction is currently being implemented at the first level (L1) trigger.

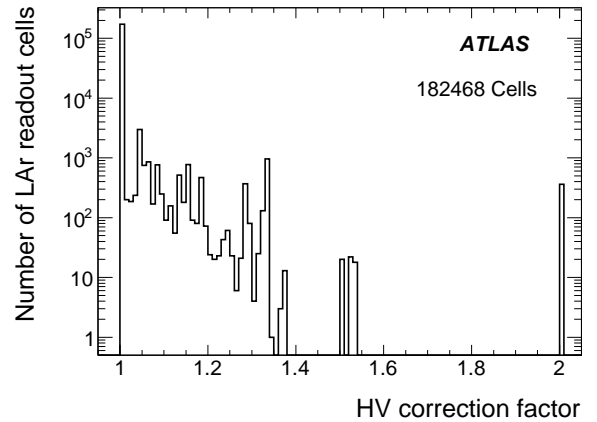


Fig. 3. High voltage correction factors for all LAr cells at the end of September 2009.

In conclusion, since the beginning of 2008, all 182,468 readout cells are powered with high voltage, and no dead region exists. Signals from regions with non-nominal high voltage are easily corrected and their impact on physics is negligible.

2.4 Readout cell status

The cell signals are read out through 1524 Front-End Boards (FEBs [20,21]) with 128 channels each, which sit inside front-end crates that are located around the periphery of the cryostats. The FEBs perform analog processing

(amplification and shaping - except for the HEC where the amplification is done inside the cryostat), store the signal while waiting for the L1 trigger decision, and digitize the accepted signals. The FEBs also perform fast analog summing of cell signals in predefined projective “towers” for the L1 trigger.

The digitized signals are transmitted via optical fibers to the Readout Drivers (RODs) [22] located in the counting room 70 m away. The cell energy is reconstructed on-line in the ROD modules up to a nominal maximum L1 rate of 75 kHz. The cell and trigger tower energy reconstruction is described in detail in Section 3.

The response of the 182,468 readout cells is regularly monitored using 122 calibration boards [23] located in the front-end crates. These boards inject calibrated current pulses through high-precision resistors to simulate energy deposits in the calorimeters. At the end of September 2009, 1.3% of cells have problems. The majority of them, i.e. 1.2% of the total number of cells, are not read-out because they are connected to 17 non-functioning FEBs. On these FEBs, the active part (VCSEL) of the optical transmitter to the ROD has failed. This failure, occurring at a rate of two or three devices per month, is under intensive investigation and are expected to be fixed during the next LHC shutdown. The remaining 0.1% of cells with problems can be split in three sub-types: incurable cells, i.e. cells not responding to the input pulse (0.02%), or which are permanently (0.03%) or sporadically (0.07%) very noisy. The first two types are always masked in the event reconstruction (121 cells), while the sporadically very noisy cells, not yet well understood, are masked on an event by event basis. For cells which do not receive calibration signals (0.3%) average calibration constants computed among neighboring cells are used. For cells with non-nominal high voltage (6.1%) a software correction factor is applied. Both have very limited impact on the energy reconstruction.

In total, 180,128 cells, representing 98.7% of the total number of cells in the LAr calorimeter, are used for event reconstruction at the end of September 2009. The number of inactive cells (1.3%) is dominated by the cells lost due to faulty optical drivers (1.2%): apart from these, the number of inactive cells has been stable in time.

2.5 Data taking conditions

The results presented here focus on the period starting in September 2008 when all the ATLAS sub-detectors were completed and integrated into the data acquisition. Apart from regular electronics calibration runs, two interesting types of data are used to commission the LAr calorimeter: the beam splash events and the cosmic muons. The first type corresponds to LHC events of September 10th 2008 when the first LHC beam hit the collimators located 200 m upstream of the ATLAS interaction point. A cascade of pions and muons parallel to the beam axis fired the beam related trigger, illuminated the whole ATLAS detector and deposited several PeV per event in the LAr calorimeter. The second type corresponds to long cosmic

muon runs acquired on September-October 2008 and on June-July 2009 where more than 300 million events were recorded, corresponding to more than 500 TB of data.

For the LAr commissioning, L1 calorimeter triggers are used to record radiative energy losses from cosmic muons while the first level muon spectrometer and second level inner detector triggers are used to study pseudo-projective minimum ionizing muons. In most of the runs analyzed, the toroidal and solenoidal magnetic fields were at the nominal value.

3 Electronic performance and quality of cell energy reconstruction

The robustness of the LAr calorimeter energy reconstruction has been studied in detail using calibration and randomly triggered events, cosmic muons and beam splash events. Section 3.1 briefly describes the energy reconstruction method in the trigger towers and in the cells, as well as a validation study of the trigger. The time stability of the electronics is discussed in Section 3.2. The status of the electronics timing for the first LHC collisions is presented in Section 3.3, and the quality of the LAr calorimeter energy reconstruction is assessed in Section 3.4.

3.1 Energy reconstruction in the LAr calorimeter

When charged particles cross the LAr gap between electrodes and absorbers, they ionize the liquid argon. Under the influence of the electric field, the ionization electrons drift towards the electrode inducing a current. The initial current is proportional to the energy deposited in the liquid argon. The calorimeter signals are then used to compute the energy per trigger tower or per cell as discussed in this section.

3.1.1 Energy reconstruction at the first level calorimeter trigger

The timing requirements for the L1 trigger latency can only be met with fast analogue summing in coarse granularity. In the EM part, the pre-summation of analog signals per layer on the FEBs serves as input to tower builder boards where the final trigger tower signal sum and shaping is performed. In the HEC and FCal, the summation is performed on the FEBs and transmitted to tower driver boards where only shaping is done. The tower sizes are $\Delta\eta \times \Delta\phi = 0.1 \times 0.1$ for $|\eta| < 2.5$ and go up to $\Delta\eta \times \Delta\phi = 0.4 \times 0.4$ for $3.1 < |\eta| < 4.9$. The analog trigger sum signals are sent to receiver modules in the service cavern. The main function of these modules is to compensate for the differences in energy calibration and signal attenuation over the long cables using programmable amplifier gains (g_R). The outputs are sent to L1 trigger pre-processor boards which perform the sampling at 40 MHz and the digitization of five samples. At this stage, both

the transverse energy and bunch crossing are determined using a finite impulse response filter, in order to maximize the signal-to-noise ratio and bunch crossing identification efficiency. During ATLAS operation, the output $g_R A^{L1}$ of the filter, which uses optimal filtering, is passed to a look-up table where pedestal (P in ADC counts) subtraction, noise suppression and the conversion from ADC counts to transverse energy in GeV ($F_{\text{ADC} \rightarrow \text{GeV}}^{L1}$) is performed in order to extract the final transverse energy value (E_T^{L1}) for each trigger tower:

$$E_T^{L1} = F_{\text{ADC} \rightarrow \text{GeV}}^{L1} (g_R A^{L1} - g_R P). \quad (2)$$

Arrays (in η - ϕ) of these E_T^{L1} energies, merged with similar information coming from the Tile calorimeter, are subsequently used to trigger on electrons, photons, jets, τ s and events with large missing transverse energy.

3.1.2 Energy reconstruction at cell level

At the cell level, the treatment of the analog signal is also performed in the front-end electronics. After shaping, the signal is sampled at 40 MHz and digitized if the event was selected by the L1 trigger. The reconstruction of the cell energy, performed in the ROD, is based on an optimal filtering algorithm applied to the samples s_j [24]. The amplitude A , in ADC counts, is computed as:

$$A = \sum_{j=1}^{N_{\text{samples}}} a_j (s_j - p), \quad (3)$$

where p is the ADC pedestal (Section 3.2.1). The Optimal Filtering Coefficients (OFCs) a_j are computed per cell from the predicted ionization pulse shape and the measured noise autocorrelation to minimize the noise and pile-up contributions to A . For cells with sufficient signal, the difference (Δt in ns) between the digitization time and the chosen phase is obtained from:

$$\Delta t = \frac{1}{A} \sum_{j=1}^{N_{\text{samples}}} b_j (s_j - p), \quad (4)$$

where b_j are time-OFCs. For a perfectly timed detector and in-time particles $|\Delta t|$ must be close to zero, while larger values indicate the need for better timing or the presence of out-of-time particles in the event.

The default number of samples used for A and Δt computation is $N_{\text{samples}} = 5$, but for some specific analyses more samples, up to a maximum of 32, are recorded. Finally, including the relevant electronic calibration constants, the deposited energy (in MeV) is extracted with:

$$E_{\text{cell}} = F_{\mu A \rightarrow \text{MeV}} \times F_{\text{DAC} \rightarrow \mu A} \times \frac{1}{\frac{M_{\text{phys}}}{M_{\text{cali}}}} \times G \times A, \quad (5)$$

where the various constants are linked to the calibration system: the cell gain G (to cover energies ranging from a maximum of 3 TeV down to noise level, three linear gains

are used: low, medium and high with ratios $\sim 1/10/100$) is computed by injecting a known calibration signal and reconstructing the corresponding cell response; the factor $1/\frac{M_{\text{phys}}}{M_{\text{cali}}}$ quantifies the ratio of response to a calibration pulse and an ionization pulse corresponding to the same input current; the factor $F_{\text{DAC} \rightarrow \mu A}$ converts digital-to-analog converter (DAC) counts set on the calibration board to μA ; finally, the factor $F_{\mu A \rightarrow \text{MeV}}$ is estimated from simulations and beam test results, and includes high voltage corrections for non-nominal settings (see Sec 2.3). Note that the crosstalk bias in the finely segmented first layer of the electromagnetic calorimeter is corrected for in the gain G [4].

3.1.3 Check of the first level tower trigger energy computation

The trigger decision is of utmost importance for ATLAS during LHC collisions since the data-taking rate is at maximum 200 Hz because of bandwidth limitations, i.e. a factor 2×10^5 smaller than the 40 MHz LHC clock. It is therefore important to check that no systematic bias is introduced in the computation of the L1 trigger energy and that the trigger energy resolution is not too degraded with respect to the offline reconstruction. In the following, this check is performed with the most granular part of the LAr calorimeter, the barrel part of the EM calorimeter, where 60 cell signals are summed per trigger tower.

Since cosmic muon events occur asynchronously with respect to the LHC clock, and the electronics for both the trigger and the standard readout is loaded with one set of filtering coefficients (corresponding to beam crossing), the reconstructed energy is biased by up to 10%, depending on the phase. For the study presented here, A^{L1} is recomputed offline by fitting a second-order polynomial to the three highest samples transmitted through the processors. The most critical part in the trigger energy computation is then to calibrate the individual receiver gains g_R . For that purpose, a common linearly increasing calibration pulse is sent to both the L1 trigger and the normal cell circuits: the inverse receiver gain $1/g_R$ is obtained by fitting the correlation between the L1 calorimeter transverse energy (E_T^{L1}) and the sum of cell transverse energies in the same trigger tower, later called *offline* trigger tower (E_T^{LAr}). In cosmic muon runs, receiver gains are set to 1.0 and are recomputed offline with dedicated calibration runs. As a cross check, the gain was also extracted using LHC beam splash event data which covers the full detector. In both cases, the L1 transverse energy is computed as in Eq. 2.

In the EM calorimeter, radiating cosmic muons may produce a local energy deposit of a few GeV, and fire the EM calorimeter trigger condition EM3 that requires a transverse energy greater than 3 GeV in a sum of four adjacent EM trigger towers. To mimic an electron coming from the interaction point, only those events that contain a track reconstructed with strict projectivity cuts are considered. Here, the L1 calorimeter transverse energy is computed using the gains determined with calibration runs. Figure 4 shows the correlation between E_T^{L1} and E_T^{LAr} .

Computing the ratio of E_T^{L1} and E_T^{LAr} gives a Gaussian distribution with a mean of 1.015 ± 0.002 , showing the very good correspondence between these two quantities, especially at low energy. This also shows that the trigger energy is well calibrated and almost unbiased with respect to the LAr readout.

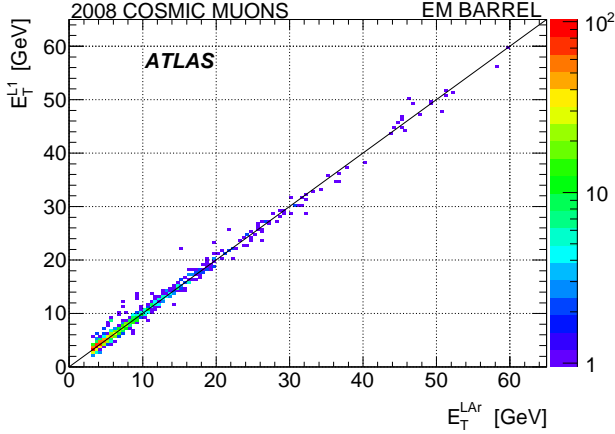


Fig. 4. $L1$ transverse energy (E_T^{L1}) computed with the receiver gains extracted from calibration runs versus the sum of cell transverse energies in the same trigger tower (E_T^{LAr}).

Figure 5 shows the corresponding resolution computed as the relative difference of E_T^{L1} and E_T^{LAr} . At low energy, the difference is dominated by electronic noise since the two readout paths have only part of their electronics in common. The ATLAS specification of 5% of $L1$ transverse energy resolution is reached for energies greater than 10 GeV. The $L1$ transverse energy resolution reaches around 3% at high energy.

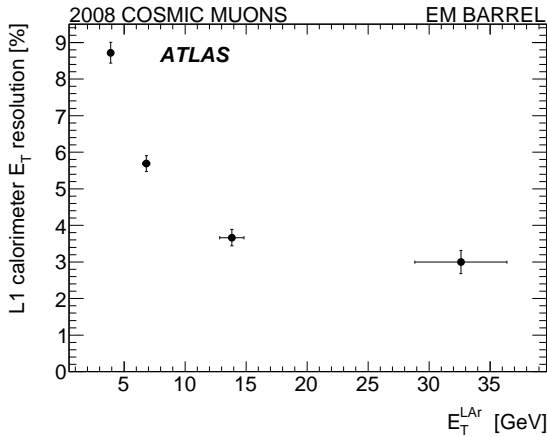


Fig. 5. Relative difference of E_T^{L1} and E_T^{LAr} ($L1$ Calorimeter E_T resolution) as a function of E_T^{LAr} . Strict projectivity cuts for the track pointing to the EM shower are applied. Horizontal error bars reflect the RMS of E_T^{LAr} in each bin.

As a crosscheck, a similar study was performed with gains computed from the beam splash events, without the projectivity cut. A slight degradation of the resolution is observed at high energy, but not at low energy where the noise dominates. Taking advantage of the higher statistics, it is possible to compute the 5 GeV “turn-on curve”, i.e. the relative efficiency for an offline trigger tower to meet the requirement $E_T^{L1} \geq 5$ GeV as a function of E_T^{LAr} . This is not the absolute efficiency as the calorimeter trigger condition EM3 is used to trigger the events. The efficiency is shown in Figure 6, where a sharp variation around a $E_T^{L1} = 5$ GeV energy threshold is observed.

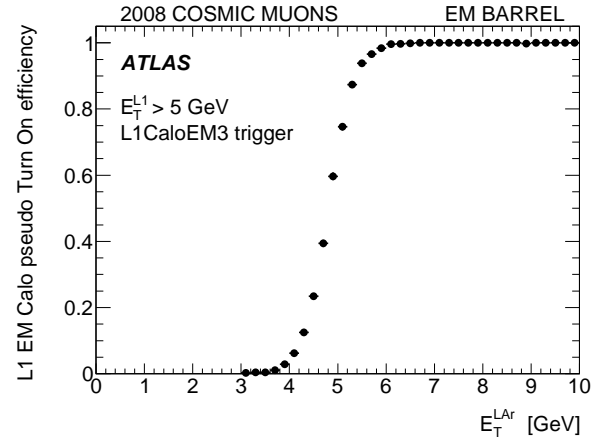


Fig. 6. Turn-on curve efficiency for $E_T^{L1} > 5$ GeV requirement obtained with events triggered by the EM3 $L1$ Calorimeter trigger.

These results give confidence that EM showers (electrons and photons) will be triggered efficiently in LHC events. After this study, the gains g_R were extracted from dedicated calibration runs and loaded into the receivers to be used for the first LHC collisions.

3.2 Electronic stability

Hundreds of millions of randomly triggered and calibration events can be used for a study of the stability of the properties of each readout channel, such as the pedestal, noise and gain. The first two quantities are computed for each cell as the mean (pedestal) of the signal samples s_j in ADC counts, and the width (noise) of the energy distribution. The gain is extracted by fitting the output pulse amplitudes against calibration pulses with increasing amplitudes.

3.2.1 Pedestal

The stability of the pedestals is monitored by measuring variations with respect to a reference pedestal value for each cell. For each FEB, an average over the 128 channels is computed.

As an example, Figure 7 illustrates the results for the 48 HEC FEBs over a period of six months in 2009. A slight drift of the pedestal with time, uncorrelated with the FEB temperature and/or magnetic field configurations, is observed. Overall, the FEB pedestal variations follow a Gaussian distribution with a standard deviation of 0.02 ADC counts, i.e. below 2 MeV. The same checks have been performed on all other FEBs, and give typical variations of around 1 (0.1) MeV and 10 (1) MeV in the EM and FCal calorimeters respectively, in medium (high) gain. These variations are much lower for the EM and HEC or at the same level for the FCal than the numerical precision of the energy computation, which is 8 (1) MeV in medium (high) gain.

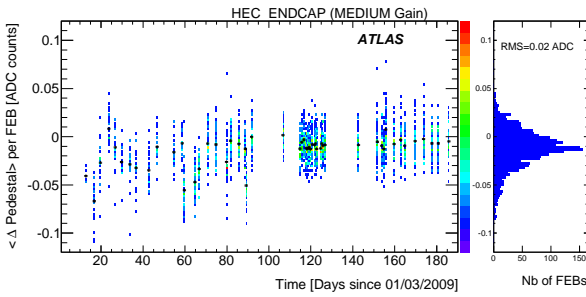


Fig. 7. Average FEB pedestal variations in ADC counts, in medium gain, for the HEC during 6 months of data taking in 2009. The crosses indicate the mean value for each time slice.

During the LHC running, it is foreseen to acquire pedestal and calibration runs between fills, thus it will be possible to correct for any small time dependence such as observed in Figure 7. In the same spirit, random triggers collected during physics runs can be used to track any pedestal variations during an LHC fill.

3.2.2 Noise

Figure 8 shows the noise measured in randomly triggered events at the cell level as a function of η for all layers of the LAr calorimeters. In all layers, a good agreement with the expected noise [1] is observed. Noise values are symmetric with respect to $\eta = 0$ and uniformly in ϕ within few percents. In the EM calorimeters, the noise ranges from 10 to 50 MeV, while it is typically a factor of 10 greater in the hadronic endcap and forward calorimeters where the granularity is 20 times coarser and the sampling fractions are lower. It should be noted that these results are obtained using five samples in Eq. (3) and (5), i.e. the noise is reduced by a factor varying from 1.5 to 1.8, depending on η , with respect to the single-sample noise value.

The coherent noise over the many cells used to measure electron and photon energies in the EM calorimeters should be kept below 5% [25] of the incoherent noise (i.e. the quadratic sum of all channel noise). For the second layer of the EM calorimeter, the contribution from the

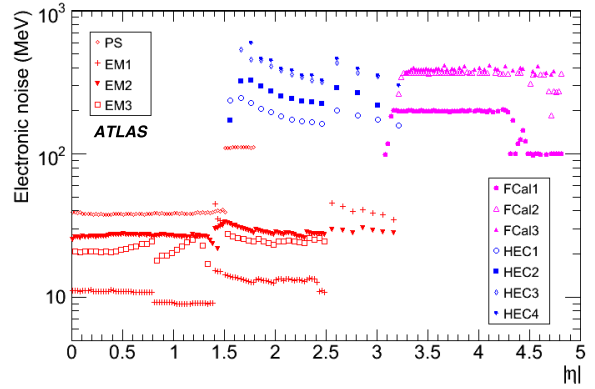


Fig. 8. Electronic noise (σ_{noise}) in randomly triggered events at the EM scale in individual cells for each layer of the calorimeter as a function of $|\eta|$. Results are averaged over ϕ .

coherent noise has been estimated to 2%, by studying simultaneous increase of noise in a group of channels.

Systematic studies of noise stability have been pursued: all noise variations are typically within ± 1 keV, 0.1 MeV and 1 MeV for EM, HEC and FCal, respectively. No correlations with the FEB temperature and/or changes of magnetic field conditions have been observed.

3.2.3 Gain

The calibration pulse is an exponential signal (controlled by two parameters, f_{step} and τ_{cali}) which emulates the triangular ionization signal. It is injected on the detector as close as possible to the electrodes, except for the FCal where it is applied at the base-plane of the front-end crates [18]. Thus, the analog cell response is treated by the FEBs in the same way as an ionization signal, but it is typically averaged over 100 triggers in the RODs and transmitted offline where the average signal peak height is computed. The cell gain is extracted as the inverse ratio of the response signal in ADC counts to the injected calibration signal in DAC counts.

The stability of the cell gain is monitored by looking at the relative gain difference averaged over 128 FEB channels. This is illustrated in Figure 9 for the 1448 FEBs of the EM calorimeter, in high gain. All variations are within $\pm 0.3\%$ and similar results are obtained for medium and low gains. An effect of 0.2% on the gains has recently been identified as coming from a particular setting of the FEBs. The two populations are most probably coming from this effect. Regular update of calibration database take account of the variations. Similar results are obtained for the HEC, and variations within $\pm 0.1\%$ are measured for the FCal.

In conclusion, results presented for the pedestals, noise, and gains illustrate the stability of the LAr electronics over several months of data taking. Values are stored in the ATLAS calibration database and are used for online and offline reconstruction.

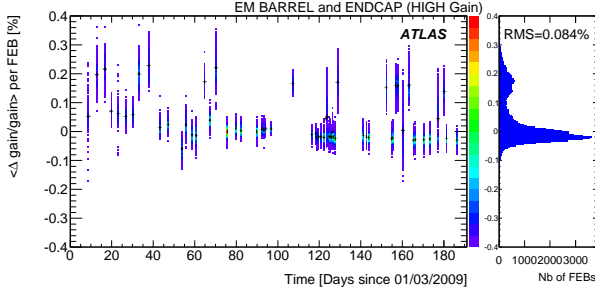


Fig. 9. Average FEB (high) gain variations during 6 months of 2009 data taking, in the EM part of the calorimeter. The crosses indicate the mean value for each time slice.

3.2.4 Global check with E_T^{miss} variable

Another way to investigate the level of understanding of pedestals and noise in the LAr calorimeter is to compute global quantities in randomly triggered events with the calorimeter, such as the vector sum of transverse cell energies. The calorimetric missing transverse energy E_T^{miss} is defined as:

$$\begin{aligned} E_x^{\text{miss}} &= -\sum_{i=1}^{N_{\text{cell}}} E_i \sin \theta_i \cos \phi_i, \\ E_y^{\text{miss}} &= -\sum_{i=1}^{N_{\text{cell}}} E_i \sin \theta_i \sin \phi_i, \\ E_T^{\text{miss}} &= \sqrt{(E_x^{\text{miss}})^2 + (E_y^{\text{miss}})^2}, \end{aligned} \quad (6)$$

where E_i is the cell energy, θ_i its polar angle and ϕ_i its azimuthal angle. Because of the high granularity of the LAr calorimeter, it is crucial to suppress noise contributions to E_T^{miss} , i.e. limit the number of cells, N_{cell} , used in the sum. In ATLAS, this is done with two methods: *i*) a cell-based method in which only cells above a noise threshold of two standard deviations ($|E_i| > 2\sigma_{\text{noise}}$) are kept; *ii*) a cluster-based method which uses only cells belonging to three-dimensional topological clusters [26]. These clusters are built around $|E_i| > 4\sigma_{\text{noise}}$ seeds by iteratively gathering neighboring cells with $|E_i| > 2\sigma_{\text{noise}}$ and, in a final step, adding all direct neighbors of these accumulated secondary cells (Topocluster 4/2/0). In randomly triggered events, about 8500 and 500 LAr cells, respectively, are selected with these two noise-suppression methods.

The distributions of E_x^{miss} and E_y^{miss} should be Gaussian and centered on zero in randomly triggered events. The measurements are compared with a Gaussian noise model, where no pedestal shift or coherent noise is present, obtained by randomizing the cell energy according to a Gaussian model for the cell noise. For this E_T^{miss} computation, cells with very high noise (see Section 2.4) are removed from the computation.

Figure 10 shows the E_T^{miss} distributions for a randomly triggered data sample acquired in 15 hours. The two noise suppression methods are compared to the corresponding Gaussian noise model. For the cell-based method, a good agreement is observed between the data and the simple model. Because of the lower number of cells kept in the cluster-based method, a smaller noise contribution to E_T^{miss} is observed. The agreement between the data and the

model is not as good as for the cell-based method, reflecting the higher sensitivity of the cluster-based method to the noise description. In both cases, no E_T^{miss} tails are present, reflecting the absence of large systematic pedestal shifts or abnormal noise.

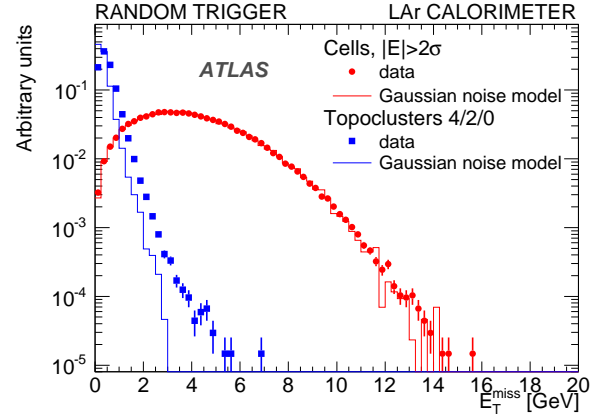


Fig. 10. E_T^{miss} distribution with LAr calorimeter cells for 135,000 randomly triggered events in June 2009. The dots (squares) show the cell-based (cluster-based) methods in the data, and the histograms show the equivalent distributions for the Gaussian noise model (see text).

Using E_T^{miss} it was possible to spot, in 2008, a high coherent noise due to the defective grounding of a barrel presampler HV cable and sporadic noise in a few preamplifiers. These two problems were repaired prior to the 2009 runs. The time stability of E_T^{miss} is regularly monitored using randomly triggered events by observing the mean and width of the E_x^{miss} and E_y^{miss} distributions. With the cluster-based method, the variation of all quantities was measured to be ± 0.1 GeV over 1.5 months. This variation is small compared to the expected E_T^{miss} resolution ($\simeq 5$ GeV for $W \rightarrow e\nu$ events) and can be controlled further by more frequent updates of the calibration constants.

A similar analysis was performed with L1 calorimeter triggered events, corresponding to radiative energy losses from cosmic muons, from the same run as used above. The L1 calorimeter trigger (L1calo) triggers events when either the sum of adjacent trigger tower transverse energies is above 3 GeV in the EM calorimeter (EM3) or 5 GeV when summing EM and hadronic towers [27]. The results are illustrated in Figure 11 for the cell-based noise suppression method. Most of these events are triggered by energy losses in the Tile calorimeter that do not spill in the LAr calorimeter, which therefore mainly records noise, leading to a E_T^{miss} distribution similar to the one obtained with random triggers. However, in few cases, events are triggered by the LAr calorimeter such as the EM3 trigger. The peak at 3 GeV is then shifted upwards to 6 GeV and the proportion of events with E_T^{miss} above 15 GeV is greatly enhanced.

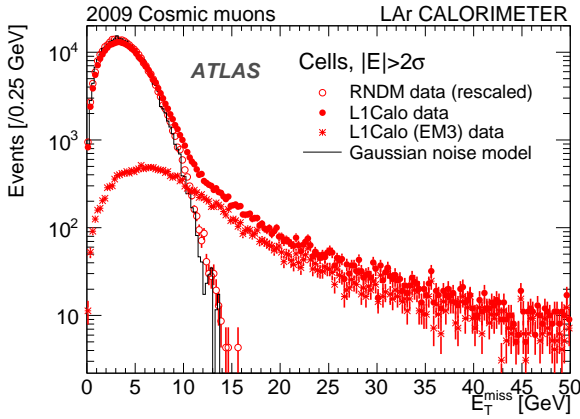


Fig. 11. E_T^{miss} distribution with LAr calorimeter cells for 300,000 L1 calorimeter (L1Calo) triggers reconstructed with the cell-based method. Results for EM3 trigger conditions (Section 3.1.3) from the same run are superimposed on the same plot and the results from randomly triggered events are again overlaid (open symbols and histogram).

3.3 LAr calorimeter timing

The energy reconstruction in each cell relies on the fact that in the standard (five samples) physics data acquisition mode, the third sample is located close to the signal maximum: this implies an alignment of the timing of all calorimeter cells to within a few ns.

Several parameters determine each cell timing: the first contribution comes from FEB internal delays which induce a cell timing variation of ± 2 ns within each FEB. This is accounted for when computing the optimal filtering coefficients. The second contribution concerns FEB to FEB variations due to different cable lengths to reach a given FEB: this relative FEB timing can vary by up to ± 10 ns and can be corrected for by setting an adjustable delay on each FEB.

The study presented here aims at predicting (using calibration data and additional hardware inputs) and measuring (using cosmic muons and beam splash data) this relative FEB timing in order to derive timing alignment delays for each FEB.

3.3.1 Timing prediction

The time of the signal maximum is different in a calibration run (t_{calib}) and in a physics run (t_{phys}). The main contribution to this time is the delay T_0 before the pulse starts to rise (the difference between the calibration and physics pulse widths is much smaller than this T_0 delay variation). This delay is driven by cable lengths which are different in these two configurations and additional delays in physics runs because of the particle time of flight, and the Timing, Trigger and Control (TTC) system configurations.

In a calibration run, a signal is injected from the calibration board through the calibration cables, and is then

read out through the physics signal cables. The value of the delay T_0^{calib} with respect to the signal injection can thus be computed for each FEB using the various cable lengths (L_{calib} , L_{physics}) and signal propagation speeds (v_{calib} , v_{physics}):

$$T_0^{\text{calib}} = \frac{L_{\text{calib}}}{v_{\text{calib}}} + \frac{L_{\text{physics}}}{v_{\text{physics}}}. \quad (7)$$

The above prediction is compared with the measured value in calibration runs. The measurement corresponds to the time at which the calibration pulse exceeds three standard deviations above the noise; it is found to agree with the prediction to within ± 2 ns, ignoring the variations within each FEB.

The time of the signal maximum t_{calib} is obtained by fitting the peak of the pulse of cells in a given FEB with a third order polynomial. As the cable length is a function of the cell position along the beam axis (z , η), the cell times are averaged per FEBs in a given layer (except for the HEC where layers are mixed inside a FEB) and a given η -bin in order to align the FEBs in time.

The time of the ionization pulse in each cell can then be predicted from the calibration time using the following formula:

$$t_{\text{phys}} = t_{\text{calib}} - \frac{L_{\text{calib}}}{v_{\text{calib}}} + t_{\text{flight}} + \Delta t_{\text{TTC}}, \quad (8)$$

where t_{calib} was defined in the previous paragraph; t_{flight} is the time of flight of an incident particle from the interaction point to the cell, which varies from 5 ns for a presampler cell at $\eta = 0$, to 19 ns for a back cell in the HEC; and Δt_{TTC} is a global correction for the six partitions due to the cabling of the TTC system which is needed to align all FEBs at the crate level. This predicted ionization pulse time is compared with the corresponding measurement in the next section.

3.3.2 Timing measurement

The ionization pulse time has been measured in beam splash and cosmic muon events. The time is reconstructed using optimal filtering coefficients. Since the arrival time of the particle is not known, one does not know in advance to which samples the time OFCs b_i should be applied (since these OFCs were computed for a particular set of samples around the pulse maximum). Therefore, an iterative procedure is used until the obtained Δt (see Eq. 4) is less than 3 ns.

The time is then corrected for two effects: first, the time-of-flight difference between the beam splash or cosmic muon configurations and the collision configuration, and second, the asynchronicity of the beam splash and cosmic muon events, where arrival times vary with respect to the TTC clock.

The comparison between the measured and the predicted (Eq. 8) ionization pulse time is shown in Figure 12 for the C-side ($\eta < 0$) of each LAr sub-detector.

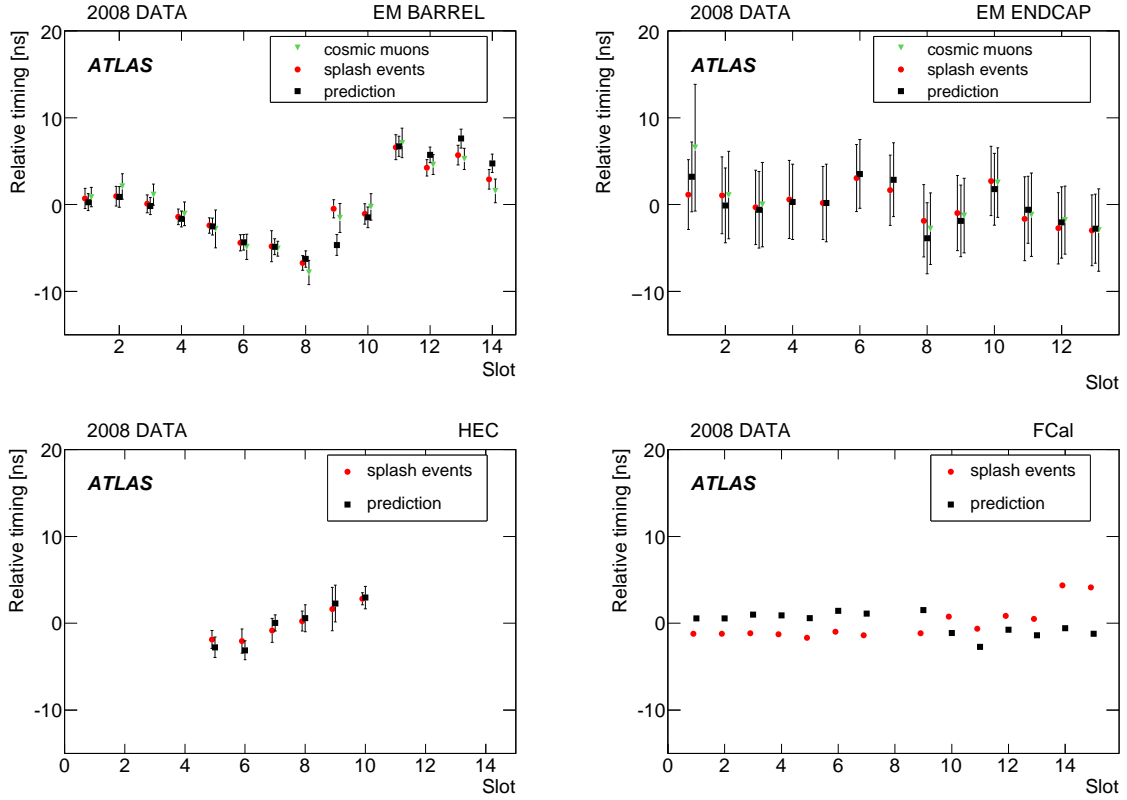


Fig. 12. Relative predicted and measured FEB times in the electromagnetic barrel (top left), electromagnetic endcap (top right), HEC (bottom left) and FCal (bottom right) calorimeters, for the C-side ($\eta < 0$). The x-axis (“Slot”) corresponds to a group of FEBs in a given layer (or a group of layers in the HEC) and η -range. The error bars show the width of the distributions in each slot.

This comparison is performed for each “slot” corresponding to a group of FEBs in a given layer and η -range, averaged over all calorimeter modules over ϕ . As mentioned in the introduction, the relative timing of each group of FEBs varies by ± 10 ns due to the different corresponding cable lengths.

On the plots, the error bars correspond to the RMS of values for all modules in a slot: in the FCal, there is only one module per slot, so no error bars are shown (also note that slot 8 is empty in the FCal). In some regions, the cosmic data statistics was not sufficient to extract the time: the corresponding bins are thus empty. The agreement between the prediction and the two measurements is within ± 2 ns (and at worse ± 5 ns for two slots of the FCal).

Finally, a set of FEB timing alignment delays is obtained from these well understood measured relative times. These delays will be used at the LHC startup and updated once the phase between the beam and the machine clock will be measured and shown to be stable. The desired precision of ± 1 ns should be reached then.

3.4 Signal reconstruction studies and impact on intrinsic global energy resolution constant term

The main ingredient for accurate energy and time reconstruction of signals from LHC collisions is the prediction of the ionization signal shape, from which the optimal filtering coefficients used in Eq. (3) are computed. After recalling the basics of the method used to predict the shape in Section 3.4.1, an estimate of the signal prediction quality with three samples in the EM calorimeter is presented in Section 3.4.2. The full 32 samples shape prediction is used to determine the ionization electron drift time needed for the OFC computation in the EM calorimeter (Section 3.4.3). Finally, from these two studies an estimate of the main contributions to the constant term in the global energy resolution of the EM calorimeter is given in Section 3.4.4.

3.4.1 Prediction of the ionization pulse shape

The standard ATLAS method for prediction of the ionization pulse shape in the EM and the HEC relies on the calibration system. A precisely known calibration signal is sent through the same path as seen by the ionization

pulses thus probing the actual electrical and readout properties of each calorimeter cell. In both the EM and the HEC, the calibration pulse properties are parameterized using two variables, f_{step} and τ_{cali} , which have been measured for all calibration boards [23] and are routinely extracted from calibration signals [28].

The predicted ionization shapes are calculated from the calibration pulses by modeling each readout cell as a resonant RLC circuit, where C is the cell capacitance, L the inductive path of ionization signal, and R the contact resistance between the cell electrode and the readout line. The effective LC and RC have been estimated from a frequency analysis of the output calibration pulse shape [28]. They were also measured with a network analyzer during the long validation period of the three cryostats [29,30,31]. For the HEC, calibration pulses are transformed into ionization signal predictions using a semi-analytical model of the readout electronics, with a functional form with zeros and poles accounting for the cable and pre-amplifier transfer functions [32,33]. The prediction of both the EM and HEC ionization pulses requires the knowledge of the electron drift time in liquid argon (T_{drift}), which can be inferred from the calorimeter properties or directly measured from data (see Section 3.4.3).

To illustrate the good quality of the pulse shape prediction, radiating cosmic muons depositing few GeV in a cell have been used. Figure 13 shows a typical 32-sample pulse recorded in the barrel (top left) and the endcap (top right) of the EM calorimeter, as well as in the HEC (bottom left). In each case, the pulse shape prediction, scaled to the measured cell energy, agrees at the few percent level with the measured pulse.

As already mentioned, in the FCal the calibration pulse is injected at the base-plane of the front-end crates, and therefore the response to a calibration signal differs significantly from the response to an ionization pulse, preventing the use of methods described above. Instead, seven sample pulse shapes recorded during the beam test campaign [9, 10] have been averaged to obtain a normalized reference pulse shape for each layer. Figure 13 (bottom right) shows a typical example where the agreement between the reference pulse shape and the data is at the 4% level.

3.4.2 Quality of signal reconstruction in the EM calorimeter

Several PeV were deposited in the full calorimeter in LHC beam splash events. As an example, Figure 14 shows the energy deposited in the second layer of the EM calorimeter. The structure in ϕ reflects the material encountered by the particle flux before hitting the calorimeter, such as the endcap toroid. In this layer, a total of 5×10^5 five sample signal shapes with at least 5 GeV of deposited energy were recorded. These events were used to estimate the quality of the pulse shape prediction for every cell.

For this purpose, a Q^2 -estimator is defined as :

$$Q^2 = \frac{1}{N_{\text{dof}}} \sum_{j=1}^{N_{\text{samples}}} \frac{(s_j - A g_j^{\text{phys}})^2}{\sigma_{\text{noise}}^2 + (kA)^2}, \quad (9)$$

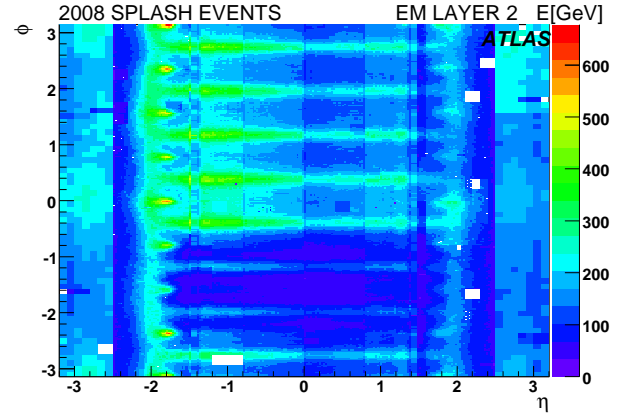


Fig. 14. Total energy deposited in the LHC beam splash events in every cell of the EM calorimeter second layer. Empty bins are due to non functioning electronics.

where the amplitude A (Eq. (3)) is computed with a number of samples $N_{\text{samples}} = 3$ (because the timing was not yet adjusted everywhere for the beam splash events, not all samples can be used), s_j is the amplitude of each sample j , in ADC counts, g_j^{phys} is the normalized predicted ionization shape and k is a factor quantifying the relative accuracy of the amplitude A . Assuming an accuracy of around 1%, with the 5 GeV energy cut applied one has $\sigma_{\text{noise}}^2 < (kA)^2$. In this regime, it is possible to fit a χ^2 function with 3 degree of freedom on the $Q^2 \times N_{\text{dof}}$ distribution over cells in the central region (where the Q^2 variation is small). Therefore, $N_{\text{dof}} = 3$. A given value of Q^2 can be interpreted as a precision on the amplitude at the level kQ .

Figure 15 shows the Q^2 -estimator in the second layer of the EM calorimeter averaged over ϕ , assuming $k = 1.5\%$ corresponding to $Q^2 \sim 1$ for $\eta \sim 0$. The accuracy is degraded by at most a factor of ~ 2 (i.e. $Q^2 \sim 4$) in some endcap regions. This shows that these data can be described with a reasonable precision.

3.4.3 Ionization electron drift time measurement in the EM calorimeter

During the 2008 cosmic runs, half a million pulses with 32 samples were recorded in the EM calorimeter from cells in which at least 1 GeV was reconstructed. Given the good accuracy of the predicted signal undershoot (see Figure 13), the drift time can be extracted from a fit to the measured signal [34].

Figure 16 shows the fitted drift time for all selected cells in the second layer using the standard pulse shape prediction method (Section 3.4.1). In the EMB, the drift time has also been measured with a method in which the shape is computed using a more analytical model and LC and RC extracted from network analyzer measurements [30]. The drift times extracted from the two methods are in excellent agreement, giving confidence in the

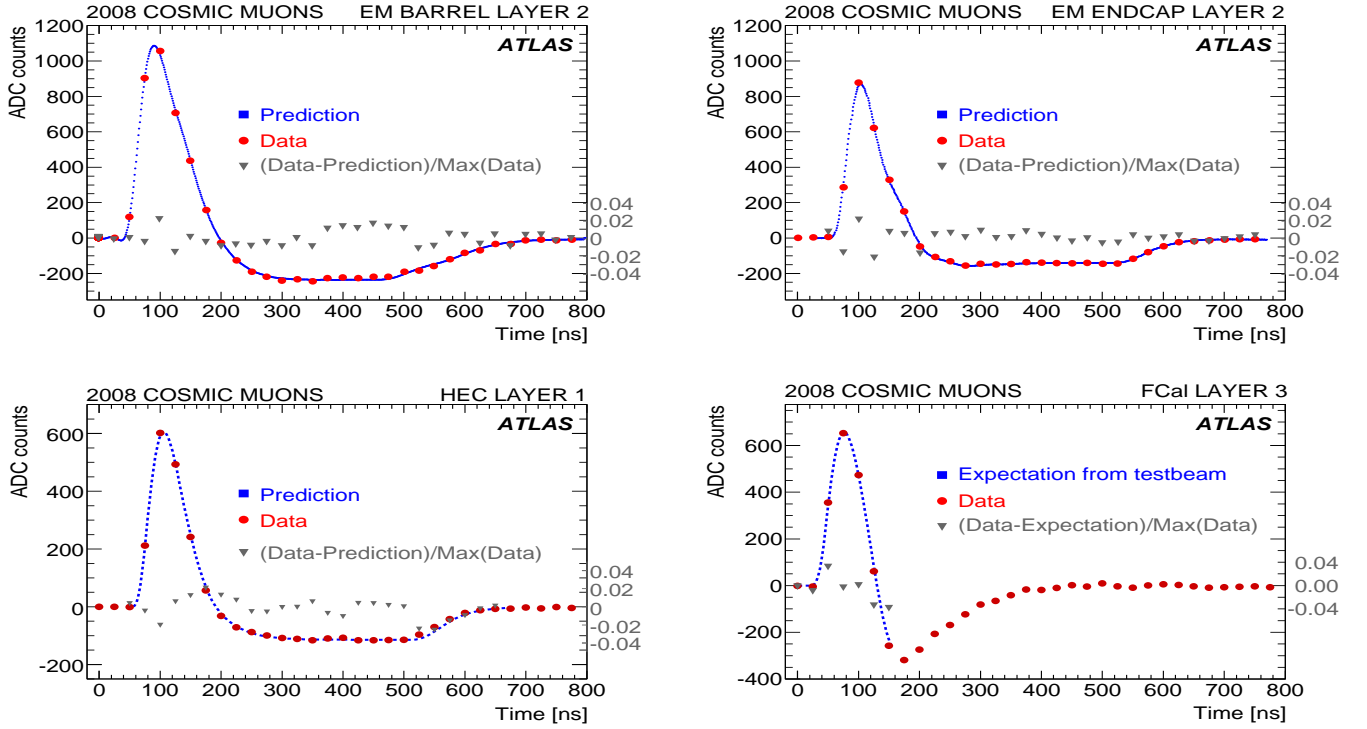


Fig. 13. Typical pulse shapes, recorded during the cosmic ray campaign, for a given cell in the second layer for the barrel (top left) and the endcap (top right) of the EM calorimeter, as well as in the first layer of the HEC (bottom left) and in the third layer of the FCal (bottom right). The relative difference between data and prediction is indicated by triangles on the right scale.

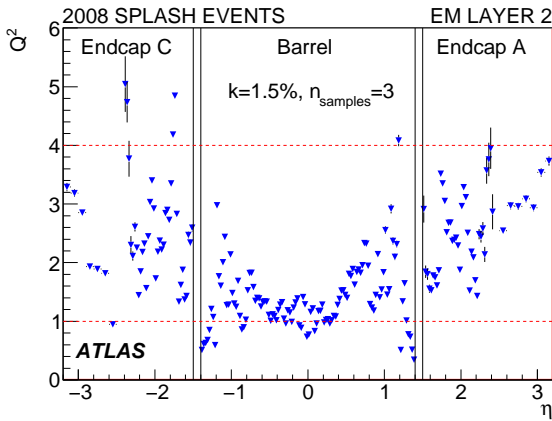


Fig. 15. Estimator Q^2 (defined in the text) as a function of η for 5×10^5 pulse shapes with $E > 5$ GeV in the EM calorimeter second layer cells. Q^2 is defined in Eq. (9) with $k = 1.5\%$.

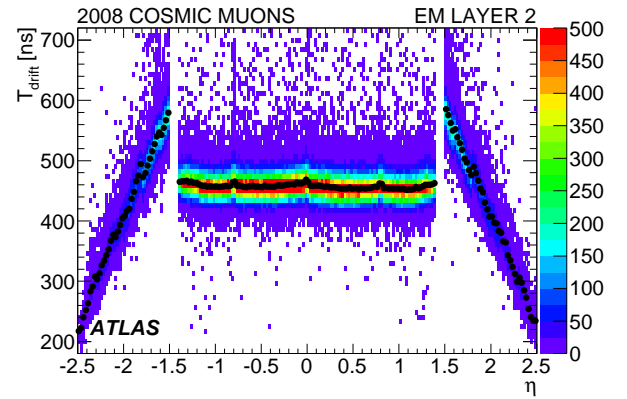


Fig. 16. Drift time measurement in the cells of the EM calorimeter second layer with $E > 1$ GeV for the 2008 cosmic muon run. The dots correspond to drift time values averaged in ϕ .

results: a constant value around the expected 460 ns is obtained, except near the electrode edges ($|\eta| = 0, 0.8$ and 1.4) where the electric field is lower. The decrease of the drift time in the EM endcap ($1.5 < |\eta| < 2.5$) reflects the decrease of the gap size with $|\eta|$. Similar results are obtained for the first and third layers of the EM calorimeters.

3.4.4 Impact on the global energy resolution constant term of the EM calorimeter

When five of the production EM calorimeter modules were tested individually in electron beams, the global constant term c of the energy resolution formula was measured to be $c \sim 0.5\%$ in the EM barrel and 0.7% in the EM end-

cap [4]. The main contributors are the signal reconstruction accuracy, the LAr gap uniformity, and the electronics calibration system. The first two contributions c_{SR} and c_{gap} can be investigated using results presented in Section 3.4.2 and 3.4.3, considering only the second layer of the EM calorimeter where most of the electromagnetic shower energy is deposited.

From Figure 15, one finds that $\langle Q^2 \rangle \sim 1.4$ in the EM barrel and 2.6 in endcap, and hence $\langle k \rangle = 1.8\%$ and 2.4% respectively. This corresponds to residuals between the predicted and measured pulses of 1 to 2% of the pulse amplitude (see Figure 13 for illustration), for samples around the signal maximum. Similar residuals were obtained in the electron beam test analysis [28]. At this time, the contribution of the signal reconstruction to the constant term was estimated to be $c_{SR} = 0.25\%$. Given the measured accuracy with beam splash events, the beam test result seems to be reachable with LHC collisions.

The drift time measured in Section 3.4.3 is a function of the gap thickness (w_{gap}) and the high voltage (V):

$$T_{drift} \sim \frac{w_{gap}^{\alpha+1}}{V^\alpha} \quad (10)$$

where $\alpha \simeq 0.3$ is empirically determined from measurements [19]. In the EM barrel, the electric field is constant, except in transition regions, and thus the drift time uniformity directly measures the LAr gap variations. To reduce statistical fluctuations, the measured drift time values are averaged over regions of $\Delta\eta \times \Delta\phi = 0.1 \times 0.1$. The distribution of the average drift time is shown in Figure 17 for the second layer of the EM barrel calorimeter.

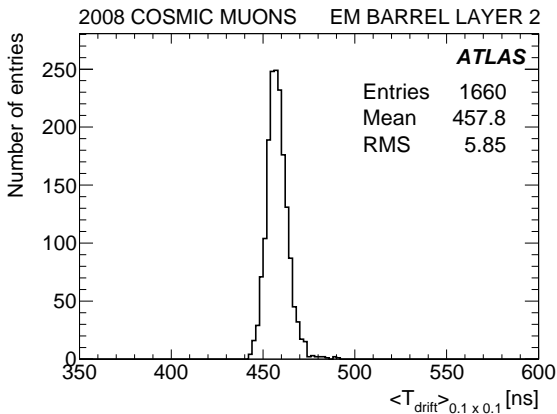


Fig. 17. Distribution of the local average drift time values in $\Delta\eta \times \Delta\phi = 0.1 \times 0.1$ bins, for the middle layer of the EM barrel.

The drift time uniformity, estimated as the ratio of the RMS of this distribution to its mean value, is $1.28 \pm 0.03\%$. Using the relation between the drift time and the gap from Equation 10, the drift time uniformity leads to a dispersion of the response due to the barrel calorimeter gap variations of $1.28\% \times \alpha / (1 + \alpha) = (0.29 \pm 0.01)\%$ [34],

representing an upper bound on the corresponding constant term c_{gap} . For comparison, during the EM calorimeter barrel module construction, the LAr gap thickness was measured, yielding an estimate of the constant term due to gap size variations of $c_{gap} = 0.16\%$ [14]. The measurement of the gap size uniformity presented here takes into account further effects like deformations in the assembled wheels and possible systematic uncertainties from the in situ cosmic muon analysis.

4 In situ EM calorimeter performance with cosmic muons

In the previous sections, we demonstrated the good performance of the electronics operation and the good understanding of the energy reconstruction. The cosmic ray events can therefore now be used to validate the Monte Carlo simulation that will be used for the first collisions.

Two such analyses are presented in this section: the first study aims to investigate the electromagnetic barrel calorimeter uniformity using ionization signals from quasi-projective cosmic muons, and the second aims to reconstruct electromagnetic showers from radiative cosmic muons and to compare the measured shower shapes with simulation.

4.1 Monte Carlo simulation

The ATLAS Monte Carlo [35,36] simulates the interaction of particles produced during LHC collisions or from cosmic muons within the ATLAS sub-detectors. It is based on the Geant4 toolkit [37] that provides the physics lists, geometry description and tracking tools. For cosmic muons, the material between the ground level and the ATLAS cavern is also simulated, i.e. the overburden and the two access shafts. The simulated cosmic ray spectrum corresponds to what was measured at sea level [38]. Air showers are not simulated but have a negligible effect on the analyses presented here. In order to save CPU time, the generated events are filtered before entering the full Geant4 simulation by requiring that the particles cross a specific detector volume (in the following analyses, typically inner detector volumes).

An important use of the simulation, amongst many others, is to validate the selection criteria on shower-shape for high-level trigger and offline algorithms, as well as to derive the electron and photon energy calibrations.

It is important to note that, thanks to the digitization step of the calorimeter simulation which emulates the behavior of the electronics, the standard energy reconstruction procedure can be applied to the simulated events. The special procedure used for asynchronous cosmic muon data, which uses an iterative determination of the event time, is however not applied to the Monte Carlo data.

4.2 Uniformity of the electromagnetic barrel calorimeter

4.2.1 Goals and means of the analysis

Any non-uniformity in the response of the calorimeter has a direct impact on the constant term in the energy resolution (see Section 3.4.4); great care was taken during the construction to limit all sources of non-uniformity to the minimum achievable, aiming for a global constant term below 0.7%. The default ATLAS Monte Carlo simulation emulates the effect of the constant term, but for the present analysis, this emulation was turned off.

The uniformity of the calorimeter was measured for three barrel production modules using electrons during beam test campaigns [4]. Cosmic muons provide a unique opportunity to measure the calorimeter uniformity in situ over a larger number of modules, unfortunately limited to the barrel calorimeter due to both the topology of the cosmic muon events and the choice of triggers. The scope of this analysis is nevertheless quite different than in the beam test. First, muons behave very differently from electrons: in most events, they deposit only a minimum ionization energy in the liquid argon and they are much less sensitive to upstream material. The result can therefore not be easily extrapolated to the electron and photon response. Second, the cosmic run statistics are limited, so uniformity cannot be studied with cell-level granularity. The goal of this cosmic muon analysis is rather to quantify the agreement between data and Monte Carlo, and to exclude the presence of any significant non-uniformity in the calorimeter response.

A previous uniformity analysis using cosmic muons [39] from 2006 and 2007 relied on the hadronic Tile calorimeter to trigger events and to measure the muon sample purity. For the 2008 data discussed here, both the muon spectrometer and inner detector were operating and were used for triggering and event selection. The data sample consists of filtered events requiring a reconstructed track in the inner detector with at least one hit in the silicon tracker. The tracks are also selected to be reasonably projective by requiring that their transverse ($|d_0|$) and longitudinal ($|z_0|$) impact parameters, with respect to the center of the coordinate system be smaller than 300 mm.

4.2.2 Signal reconstruction

In the first step, a muon track is reconstructed in the inner detector. For that purpose, a dedicated algorithm looks for a single track crossing both the top and bottom hemispheres. This single track is then extrapolated both downward and upward into the calorimeter.

Around the two track impact positions in the calorimeter, a rectangle of cells (the cell road) is selected in the first and second layers (the signal to noise ratio for muons is too low in the third layer). The cells of the first layer have a size of $\Delta\eta \times \Delta\phi = 0.003 \times 0.1$ and 12×3 such cells are kept. Similarly, the cells of the second layer have a size of $\Delta\eta \times \Delta\phi = 0.025 \times 0.025$, and 5×5 such cells are kept.

To reconstruct the energy of the selected cells, the muon timing is obtained via an iterative procedure that is usually only applied to cells with an ADC signal at least four times the noise level. Since most muons are minimum ionizing particles, the muon signal is small, typically 150 MeV is deposited in the most energetic cell in the second layer, only five times the noise, and many cells do not pass this threshold. Therefore, an alternative reconstruction is used in this analysis: in the first pass, the iteration threshold is lowered to zero so that the timing is computed for most of the cells. In the second pass, the timing of the most energetic cell determined in the first pass is applied to all the other cells of the road. The cell energy is reconstructed at the electron energy scale and thus does not represent the true energy loss of the muon. Finally, clusters are formed in each layer to reconstruct the muon energy loss. The criteria used to decide on the cluster size are described below.

4.2.3 Optimization of the uniformity measurement

In order to perform the most accurate evaluation of the calorimeter uniformity, the measurement granularity, the cluster size and the selection cuts have been optimized. The granularity chosen is a compromise between the need for high statistics (large binning) and the need for high precision. The cluster size optimizes the signal to noise ratio while the selection cuts reduce the biases while keeping high statistics.

The binning is determined by requiring a minimum of 500 events per unit. In the η direction, this corresponds to bins of 0.025 (equal to the second layer cell width) up to $|\eta| = 0.7$ and wider bins above.

In the first layer, the muon energy loss is measured using a $\Delta\eta \times \Delta\phi = 2 \times 1$ (in first layer cell unit) cluster, which contains most of the deposited energy. Adding an additional cell brings more noise than signal. In the second layer, a 1×3 (in second layer cell unit) cluster is used: it suffers less from noise than a 3×3 cluster, but requires the removal of non-projective events which leak outside the cluster along the η direction.

This projectivity cut is based on the centrality of the muon in the second layer cell: when the muon passes close to the edge of the cell, a very small non-projectivity induces a large energy leakage into the neighboring cell. Therefore, for each second layer cell, eight bins corresponding to the eight first layer cells located in front of it were defined, and in each bin a cut is applied on the beam impact parameter z_0 of the track, such that the muon is geometrically contained in the second layer cell. The remaining statistics after this projectivity cut is 76 k events in the data sample and 113 k events in the Monte Carlo sample. The events are mainly located under the cavern shafts leading to a coverage of around 20% of the full electromagnetic barrel calorimeter.

A comparison of the energy reconstructed in the first and second layers between data and Monte Carlo events is shown in Figure 18. Because the muon energy loss is mostly η -dependent, both distributions are shown for all

events (top), showing a large width due to the variation of the energy response over η , and for a single η -bin (bottom).

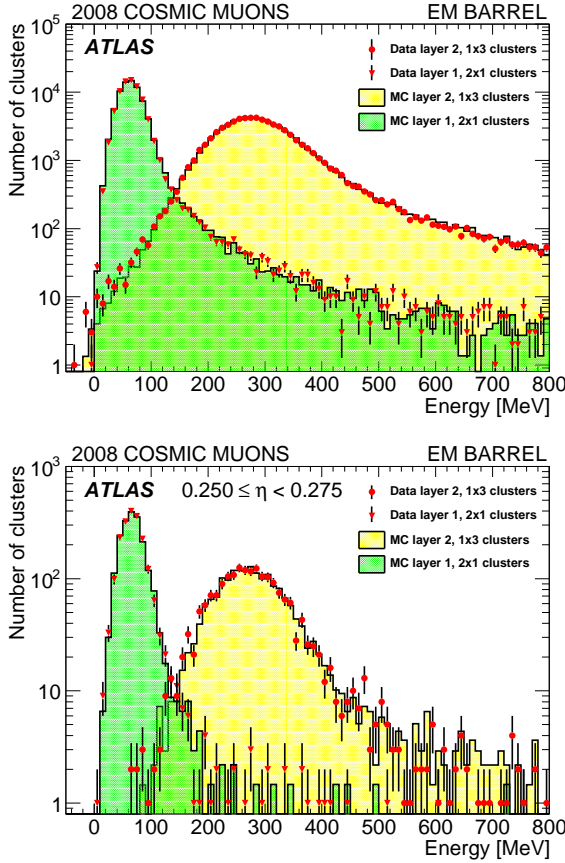


Fig. 18. Energy in a 2×1 cluster in the first layer (histogram for Monte Carlo and triangles for data) and in a 1×3 cluster in the second layer (histogram for Monte Carlo and full circles for data) for all events (top) and a single η -bin (bottom).

The agreement between the data and Monte Carlo distributions is very good, both for the shape and for the absolute energy scale which differs by only 2% in the front layer and 1% in the second layer. Part of the difference comes from the slight difference in acceptance for data and Monte Carlo, as well as from the difference in energy reconstruction. This overall energy scale difference is corrected for in the MC in the rest of the study.

4.2.4 Calorimeter uniformity along η

Given the limited statistics of the projective cosmic muon data, the uniformity of the response in η cannot be estimated at the cell level. A natural choice of cell combination is to integrate clusters in ϕ since the response should not vary along this direction due to the ϕ symmetry of the calorimeter. The response along the η direction for cosmic muons depends on the variation of the amount of liquid

argon seen by the muon. In particular, a transition occurs at $|\eta| = 0.8$ where the lead thickness goes from 1.53 mm to 1.13 mm.

The estimation of the muon energy in each η -bin is done with a fit of the cluster energy distribution using a Landau function convoluted with a Gaussian. The Landau function accounts for fluctuations of the energy deposition in the ionization process and the Gaussian accounts for the electronic noise and possible remaining fluctuations. In particular, a 10% difference is observed between the width of the Gaussian expected from the electronic noise and the width of the fitted Gaussian. Mostly this bias comes from remaining cluster non-containment effects which are found to be η -independent and thus do not produce any artificial non-uniformity. The most probable value (MPV) of the Landau distribution estimates the energy deposition.

Distributions of data and Monte Carlo MPVs along the η direction for the first and second layers are shown in Figure 19.

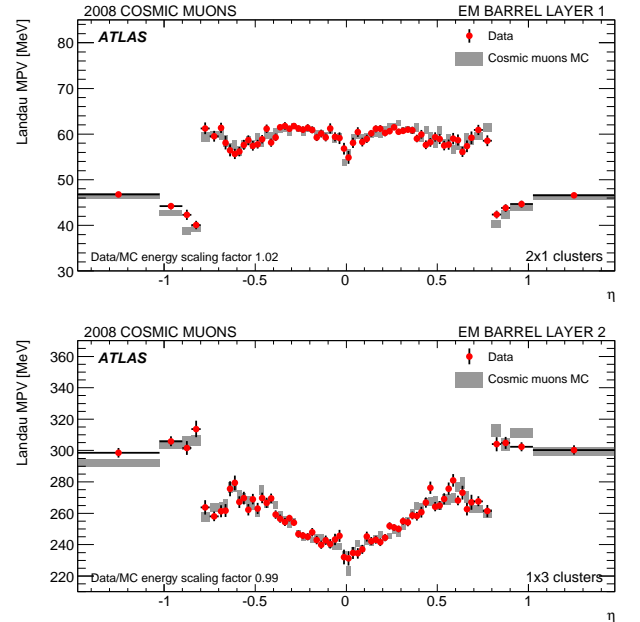


Fig. 19. Landau MPV as a function of η in the first (top) and second (bottom) layers for the data (red points) and Monte Carlo (grey bands).

In the first layer, the MPVs are roughly constant along η , except around $\eta = 0$ where some cells are physically missing in the detector, and around $|\eta| = 0.6$ where the cell depth is varying. In the second layer, the response follows a typical “V-shape” corresponding to the variation of the cell depth along η that rises up to $|\eta| = 0.6$. Again, the agreement between the data and Monte Carlo is very good, showing that the contribution of systematic effects due to the energy reconstruction method or the non-projectivity of the tracks is small.

The response uniformity U_{meas} is given by the RMS of the normalized differences between the data and Monte

Carlo MPVs in each η -bin :

$$U_{\text{meas}} = \sqrt{\frac{\sum_{i=1}^{N_b} (U_{i,\text{meas}} - \langle U_{i,\text{meas}} \rangle)^2}{N_b}}, \quad (11)$$

with:

$$U_{i,\text{meas}} = \frac{MPV_{i,\text{Data}} - MPV_{i,\text{MC}}}{MPV_{i,\text{Data}}}, \quad (12)$$

where $U_{i,\text{meas}}$ is averaged over ϕ , N_b is the number of bins in η , and $\langle U_{i,\text{meas}} \rangle = 0$ since the global energy scale difference was corrected by rescaling the MC.

The measured uniformity should be compared to the expected uniformity U_{exp} given by:

$$U_{i,\text{exp}} = \sqrt{U_{i,\text{Data}}^2 + U_{i,\text{MC}}^2} \quad (13)$$

with:

$$U_{i,\text{Data(MC)}} = \sqrt{\frac{1}{N_b} \sum_{i=1}^{N_b} \left(\frac{\sigma(MPV_{i,\text{Data(MC)}})}{MPV_{i,\text{Data(MC)}}} \right)^2}, \quad (14)$$

where $\sigma(MPV_{i,\text{Data(MC)}})$ is the statistical uncertainty on the measured Landau MPV. This uncertainty is due to the finite statistics of the data and Monte Carlo samples in each bin, the Landau dispersion of the ionization, and the electronic noise.

The measured uniformity U_{meas} should agree with the expected uniformity U_{exp} if the Monte Carlo simulation reproduces the data well: the key ingredients are the acceptance, the muon spectrum, and the energy reconstruction method. A significant departure of the measured uniformity from the expected one would be a measurement of additional non-uniformities U_{Δ} ($U_{\Delta}^2 = U_{\text{meas}}^2 - U_{\text{exp}}^2$).

The measured and expected uniformities for the two EM layers are shown in Figure 20.

The fluctuations of the measured energies are large: the RMS of the corresponding distribution is $2.4 \pm 0.2\%$ in the first layer and $1.7 \pm 0.1\%$ in the second layer, showing that the statistical power of the analysis is limited given the available data and Monte Carlo statistics. The fluctuations mostly remain within the limits of the band representing the expected values. The RMS of the latter distribution is 2.2 % in the first layer and 1.6 % in the second layer. This demonstrates that no significant additional non-uniformity (U_{Δ}) is present in the data. An upper limit is derived and yields $U_{\Delta} < 1.7\% @ 95\% \text{ CL}$ in the first layer, and $U_{\Delta} < 1.1\% @ 95\% \text{ CL}$ in the second layer.

The calorimeter response uniformity along η (averaged over ϕ) is thus consistent at the percent level with the Monte Carlo simulation and shows no significant non-uniformity.

4.3 Electromagnetic shower studies

The second analysis aims at validating the Monte Carlo simulation of the distribution of some key calorimeter variables used in the ATLAS electron/photon identification.

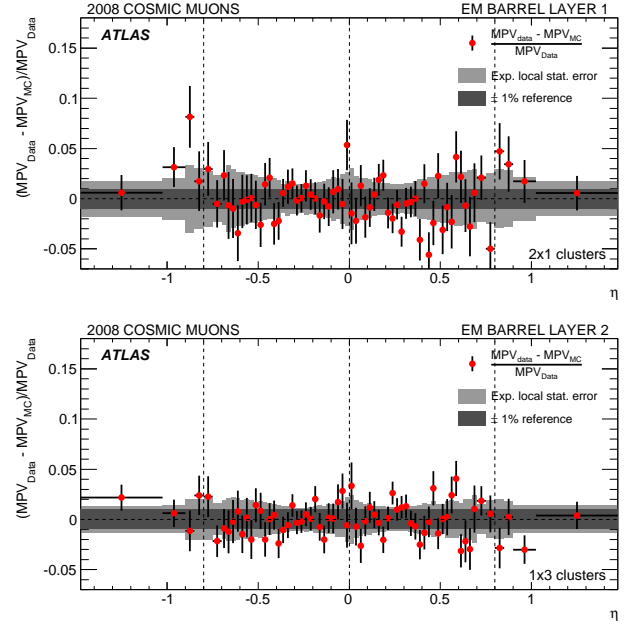


Fig. 20. Measured $U_{i,\text{meas}}$ (red points) and expected $U_{i,\text{exp}}$ (light grey band) cosmic muon energy dispersions as function of η for the first (top) and second (bottom) layers of the EM barrel. The dark grey band indicates a $\pm 1\%$ strip for reference.

This is done using radiative cosmic muons that can give rise to electromagnetic showers in the calorimeter through bremsstrahlung or pair conversions.

4.3.1 Selection of radiative muons

To increase the probability of the presence of a muon in the event, it is requested that at least one track has been reconstructed in the inner detector barrel with $|d_0| < 220$ mm and $p_T > 5$ GeV: these cuts ensure a similar acceptance for data and Monte Carlo.

A radiative energy loss is searched for in the electromagnetic barrel calorimeter by requiring a cluster with an energy greater than 5 GeV. Since the radiation can occur anywhere along the muon path, the corresponding shower is not always fully contained in the electromagnetic calorimeter: this is visible in Figure 21 which shows the fraction of the cluster energy deposited in the first layer for simulated single photons from interaction vertex and for electromagnetic showers from radiating cosmic muons. This shows that the longitudinal shower development of the radiative photons is well reproduced by the Monte Carlo simulation, and that most of the radiating muons deposit very little energy in the first layer. To select “collision-like” showers, this fraction is requested to be greater than 0.1. A total of 1200 candidates remain in the data sample and 2161 in the Monte Carlo after this selection.

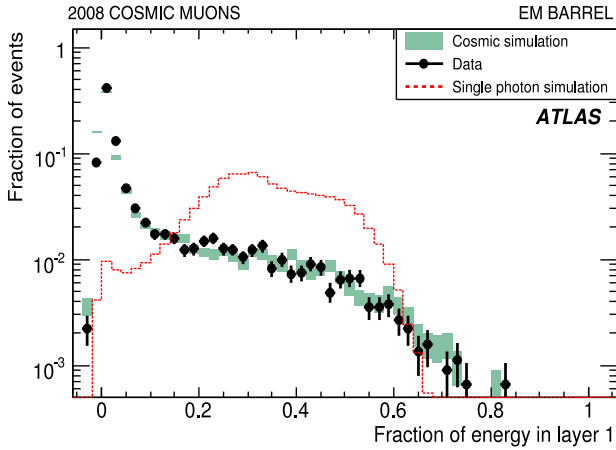


Fig. 21. Fraction of cluster energy deposited in the first layer of the electromagnetic barrel calorimeter for cosmic data (dots) and Monte Carlo (rectangles), as well as for simulated single photons of 5 GeV momentum from interaction vertex (red histogram).

4.3.2 Shower shape validation

Various shower shape distributions used for photon identification have been compared with the Monte Carlo simulation: Figures 22 and 23 show two distributions of variables related to lateral shower containment in the first and second layers of the electromagnetic calorimeter.

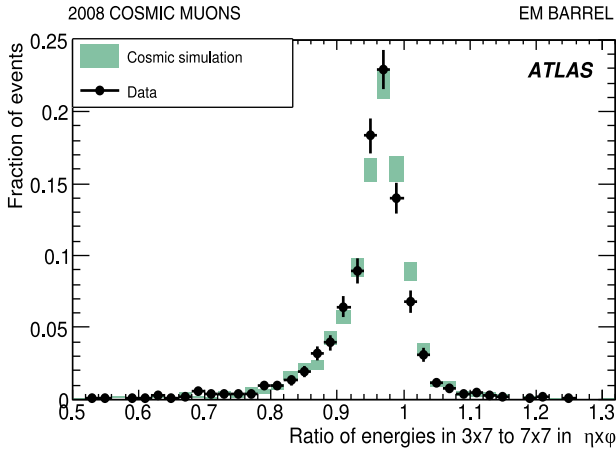


Fig. 22. Lateral shower containment in the second layer of the calorimeter given by the ratio of the energy deposited in a 3×7 cluster to a 7×7 cluster for radiative cosmic muon data (dots) and Monte Carlo simulation (rectangles).

Figure 22 shows the ratio of the energy deposited in a $\Delta\eta \times \Delta\phi = 3 \times 7$ (in second layer cell unit) cluster to that in a 7×7 cluster, in the second layer of the barrel calorimeter. In LHC collisions, this variable distinguishes electromagnetic showers, contained in 3 cells in η , from hadronic showers, leaking outside these 3 cells.

Figure 23 shows the variable $F_{\text{side}} = (E_{\pm 3} - E_{\pm 1})/E_{\pm 1}$ computed as the ratio of energy within seven central cells in the first layer ($E_{\pm 3}$), outside a core of three central cells ($E_{\pm 1}$), over energy in the three central cells: in LHC collisions, this variable typically separates photons, where little energy is deposited outside the core region, from π^0 s, where the two photons produced by the π^0 deposit some energy outside the core region. The agreement between the Monte Carlo simulation and the cosmic ray data is very good in both the cases where the electromagnetic shower develops in the “collision-like” direction (in the bottom hemisphere) and the case where it develops in the backward direction (in the top hemisphere).

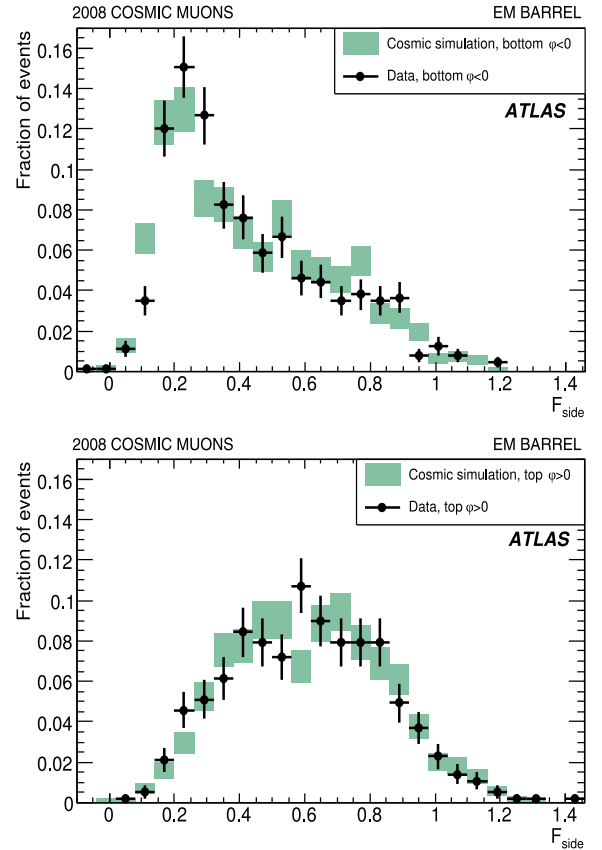


Fig. 23. Lateral shower containment in the first layer for “collision-like” (top panel) or “reverse” (bottom panel) electromagnetic showers for radiative cosmic muon data (dots) and Monte Carlo simulation (rectangles). The definition of the F_{side} is given in the text.

Within the statistics available from data, important calorimeter variables used in the electron/photon identification in ATLAS illustrate the good agreement between the Monte Carlo simulation and electromagnetic showers from radiative cosmic events in the calorimeter. These results, as well as the numerous comparisons done with beam test data [2,3,4,5,6], give confidence that robust photon and electron identification will be available for early data at the LHC.

5 Conclusions and Perspectives

The liquid argon calorimeter has been installed, connected and fully readout since the beginning of 2008. Since then, much experience has been gained in operating the system. Thanks to the very stable cryogenics and electronics operation over this period, first performance studies with the complete LAr calorimeter coverage have been done using several months of cosmic muon data and with LHC beam splash events from September 2008. These data provided a check of the first level trigger energy computation and the timing of the electronics. In the EM calorimeter, detailed studies of the signal shape predictions allow to check that, within the accuracy of the analysis, there is no extra contribution to the dominant contributions to the intrinsic constant term of the energy resolution. This indicates that the reach of a global constant term of 0.7% is achievable. The non-uniformity of the EM barrel calorimeter response to cosmic muons is consistent at the percent level with the simulated response. Finally, the electromagnetic shower profiles are in good agreement with the simulated ones, thus validating the Monte Carlo description. All these results allow for strong confidence in the readiness of the LAr calorimeter for the first LHC collisions.

The ultimate LAr calorimeter performance will be assessed with collision data: this is particularly true for the electromagnetic and hadronic energy scale computation in the ATLAS environment, which is needed for many ATLAS physics analyses.

6 Acknowledgements

We are greatly indebted to all CERN's departments and to the LHC project for their immense efforts not only in building the LHC, but also for their direct contributions to the construction and installation of the ATLAS detector and its infrastructure. We acknowledge equally warmly all our technical colleagues in the collaborating institutions without whom the ATLAS detector could not have been built. Furthermore we are grateful to all the funding agencies which supported generously the construction and the commissioning of the ATLAS detector and also provided the computing infrastructure.

The ATLAS detector design and construction has taken about fifteen years, and our thoughts are with all our colleagues who sadly could not see its final realisation.

We acknowledge the support of ANPCyT, Argentina; Yerevan Physics Institute, Armenia; ARC and DEST, Australia; Bundesministerium für Wissenschaft und Forschung, Austria; National Academy of Sciences of Azerbaijan; State Committee on Science & Technologies of the Republic of Belarus; CNPq and FINEP, Brazil; NSERC, NRC, and CFI, Canada; CERN; NSFC, China; Ministry of Education, Youth and Sports of the Czech Republic, Ministry of Industry and Trade of the Czech Republic, and Committee for Collaboration of the Czech Republic with CERN; Danish Natural Science Research Council; European Commission, through the ARTEMIS Research Training Network; IN2P3-CNRS and Dapnia-CEA, France; Georgian

Academy of Sciences; BMBF, DESY, DFG and MPG, Germany; Ministry of Education and Religion, through the EPEAEK program PYTHAGORAS II and GSRT, Greece; ISF, MINERVA, GIF, DIP, and Benoziyo Center, Israel; INFN, Italy; MEXT, Japan; CNRST, Morocco; FOM and NWO, Netherlands; The Research Council of Norway; Ministry of Science and Higher Education, Poland; GRICES and FCT, Portugal; Ministry of Education and Research, Romania; Ministry of Education and Science of the Russian Federation, Russian Federal Agency of Science and Innovations, and Russian Federal Agency of Atomic Energy; JINR; Ministry of Science, Serbia; Department of International Science and Technology Cooperation, Ministry of Education of the Slovak Republic; Slovenian Research Agency, Ministry of Higher Education, Science and Technology, Slovenia; Ministerio de Educación y Ciencia, Spain; The Swedish Research Council, The Knut and Alice Wallenberg Foundation, Sweden; State Secretariat for Education and Science, Swiss National Science Foundation, and Cantons of Bern and Geneva, Switzerland; National Science Council, Taiwan; TAEK, Turkey; The Science and Technology Facilities Council and The Leverhulme Trust, United Kingdom; DOE and NSF, United States of America.

References

1. G. Aad *et al.*, *The ATLAS Experiment at the CERN Large Hadron Collider*, JINST **3** (2008) S08003.
2. J. Colas *et al.*, *Position resolution and particle identification with the ATLAS EM calorimeter*, Nucl. Inst. Meth. **A 550** (2005) 96.
3. M. Aharrouche *et al.*, *Energy linearity and resolution of the ATLAS electromagnetic barrel calorimeter in an electron test-beam*, Nucl. Inst. Meth. **A 568** (2006) 601.
4. M. Aharrouche *et al.*, *Response uniformity of the ATLAS liquid argon electromagnetic calorimeter*, Nucl. Inst. Meth. **A 582** (2007) 429.
5. M. Aharrouche *et al.*, *Time resolution of the ATLAS barrel liquid argon electromagnetic calorimeter*, Nucl. Inst. Meth. **A 597** (2008) 178.
6. M. Aharrouche *et al.*, *Study of the response of ATLAS electromagnetic liquid argon calorimeters to muons*, Nucl. Inst. Meth. **A 606** (2009) 419.
7. B. Dowler *et al.*, *Performance of the ATLAS hadronic end-cap calorimeter in beam tests*, Nucl. Inst. Meth. **A 482** (2002) 96.
8. A.E. Kiryunin *et al.*, *GEANT4 physics evaluation with testbeam data of the ATLAS hadronic end-cap calorimeter*, Nucl. Inst. Meth. **A 560** (2006) 278.
9. J.C. Armitage *et al.*, *Electron signals in the forward calorimeter prototype for ATLAS*, JINST **2** (2007) P11001.
10. J.P. Archambault *et al.*, *Energy calibration of the ATLAS liquid argon Forward Calorimeter*, JINST **3** (2008) P02002.
11. M. Aharrouche *et al.*, *Measurement of the Response of the ATLAS Liquid Argon Barrel Calorimeter to Electrons at the 2004 Combined Test-Beam*, Nucl. Inst. Meth. **A 614** (2010) 400.
12. C. Cojocaru *et al.*, *Hadronic calibration of the ATLAS liquid argon end-cap calorimeter in the pseudorapidity region*

- 1.6 < η < 1.8 in beam tests, Nucl. Inst. Meth. **A 531** (2004) 481.
13. J. Pinfold *et al.*, *Performance of the ATLAS liquid argon endcap calorimeter in the pseudorapidity region $2.5 < \eta < 4.0$ in beam tests*, Nucl. Inst. Meth. **A 593** (2008) 324.
14. B. Aubert *et al.*, *Construction, assembly and tests of the ATLAS electromagnetic barrel calorimeter*, Nucl. Inst. Meth. **A 558** (2006) 388.
15. M. Aleksa *et al.*, *Construction, assembly and tests of the ATLAS electromagnetic end-cap calorimeter*, JINST **3** (2008) P06002.
16. M.L. Andrieux *et al.*, *Construction and test of the first two sectors of the ATLAS liquid argon presampler*, Nucl. Inst. Meth. **A 479** (2002) 316.
17. D.M. Gingrich *et al.*, *Construction, assembly and testing of the ATLAS hadronic end-cap calorimeter*, JINST **2** (2007) P05005.
18. A. Artamonov *et al.*, *The ATLAS forward calorimeters*, JINST **3** (2008) P02010.
19. C. de La Taille and L. Serin *Temperature dependence of the ATLAS electromagnetic calorimeter signal. Preliminary drift time measurement*, ATL-LARG-95-029.
20. N.J. Buchanan *et al.*, *Design and implementation of the front-end board for the readout of the ATLAS liquid argon calorimeters*, JINST **3** (2008) P03004.
21. N.J. Buchanan *et al.*, *ATLAS liquid argon calorimeter front end electronics system*, JINST **3** (2008) P09003.
22. A. Bazan *et al.*, *ATLAS liquid argon calorimeter back end electronics*, JINST **2** (2007) P06002.
23. J. Colas *et al.*, *Electronics calibration board for the ATLAS liquid argon calorimeters*, Nucl. Inst. Meth. **A 593** (2008) 269.
24. W.E. Cleland and E.G. Stern, *Signal processing considerations for liquid ionization calorimeter in a high rate environment*, Nucl. Inst. Meth. **A 338** (1994) 467.
25. ATLAS collaboration, *Liquid argon calorimeter technical design report*, CERN-LHCC-96-041, <http://cdsweb.cern.ch/record/331061>.
26. W. Lampl *et al.*, *Calorimeter clustering algorithms: Description and performance*, ATL-LARG-PUB-2008-002.
27. R. Achenbach *et al.*, *The ATLAS Level-1 calorimeter trigger*, JINST **3** (2008) P03001.
28. D. Banfi, M. Delmastro and M. Fanti, *Cell response equalization of the ATLAS electromagnetic calorimeter without the direct knowledge of the ionization signals*, JINST **1** (2006) P08001.
29. S. Baffioni *et al.*, *Electrical Measurements on the Atlas Electromagnetic Barrel Calorimeter*, ATL-LARG-PUB-2007-005.
30. C. Collard *et al.*, *Prediction of signal amplitude and shape for the ATLAS electromagnetic calorimeter*, ATL-LARG-PUB-2007-010.
31. C. Gabaldon Ruiz *et al.*, *Signal reconstruction in the EM end-cap calorimeter and check with cosmic data in the region $0 < \eta < 3.2$* , ATL-LARG-PUB-2008-001.
32. H. Brettel *et al.*, *Calibration of the ATLAS hadronic end-cap calorimeter*, Proceedings of the 6th Workshop on Electronics for LHC Experiments, Krakow (Poland, September 2000), p.218.
33. J. Ban *et al.*, *Cold electronics for the liquid argon hadronic end-cap calorimeter of ATLAS*, Nucl. Inst. Meth. **A 556** (2006) 158.
34. ATLAS Collaboration, *Drift Time Measurement in the ATLAS Liquid Argon Electromagnetic Calorimeter using Cosmic Muons Data*, to be published.
35. ATLAS Collaboration, *The ATLAS Monte Carlo project*, to be published.
36. J.P. Archambault *et al.*, *The Simulation of the ATLAS Liquid Argon Calorimetry*, ATL-LARG-PUB-2009-001.
37. S. Agostinelli *et al.*, *GEANT4: A Simulation toolkit*, Nucl. Inst. Meth. **A 506** (2003) 250.
38. A. Dar, *Atmospheric neutrinos, astrophysical neutrons, and proton-decay experiments*, Phys.Rev.Lett. **51** (1983) 227-230.
39. M. Cooke *et al.*, *In situ commissioning of the ATLAS electromagnetic calorimeter with cosmic muons*, ATL-LARG-PUB-2007-013.